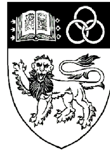

Founded 1905

A MICRO CAPACITIVE PRESSURE SENSOR WITH TWO DEFORMABLE ELECTRODES: DESIGN, OPTIMIZATION AND FABRICATION

GE PEI
(MASTER OF SCIENCE)

A THESIS SUBMITTED
FOR THE DEGREE OF PHILOSOPHY DOCTOR

DEPARTMENT OF ELECTRICAL AND
COMPUTER ENGINEERING

NATIONAL UNIVERSITY OF SINGAPORE

2006

Acknowledgments

I would like to express my sincere appreciation to my advisor, Dr. Tan Woei Wan, for her excellent guidance and gracious encouragement through my study. Her uncompromising research attitude and stimulating advice helped me in overcoming obstacles in my research. Her wealth of knowledge and accurate foresight benefited me in finding the new ideas. Without her, I would not able to finish the work here. I am indebted to her for her care and advice not only in my academic research but also in my daily life. I wish to extend special thanks to Associate Professor Tay Eng Hock for his constructive suggestions which benefit my research a lot. It is also my great pleasure to thank Associate professor Loh Ai Poh and Associate professor Miao Jianmin who have in one way or another give me their kind help.

Also I would like to express my thanks to Dr. Samudra Ganesh, Dr. Wong Wai Kin and Dr. Wang Qingguo, for their comments, advice, and inspiration. Special gratitude goes to my friends and colleagues. I would like to express my thanks to Mr. Phang Jyh Siong, Mr. Chen Bantao, Mr. Sun Jianbo, Mr. Lu Xiang, Mr. Shao Lichun and many others working in the Advanced Control Technology Lab. I enjoyed very much the time spent with them. I also appreciate the National University of Singapore for the research facilities and scholarship.

Finally, I also want to thank my family for their love, support and encouragement.

Contents

Acknowledgements **i**

Contents **ii**

List of Figures **vi**

List of Tables **xi**

Summary **xiii**

1 Introduction **1**

1.1 Review of MEMS technology 1

1.2 Fabrication Techniques 2

1.2.1 Bulk micromachining 3

1.2.2 Surface micromachining 5

1.3 Review of micro pressure sensors 6

1.3.1 Micro piezoresistive pressure sensor 7

1.3.2 Micro capacitive pressure sensor 8

1.3.3 Micro resonant pressure sensor 9

1.4 Motivations 12

1.4.1 Hydrostatic Tank Gauging 12

1.4.2 Pipeline monitoring 14

1.4.3 Biomedical applications 14

1.5 Contributions 15

1.6 Organization of the Thesis 17

2 Simulation of Micro Sensors with Two Deformable Diaphragms 19

2.1 Sensor Structure . . . 20

2.2 Analysis of diaphragm deformations . . . 22

2.2.1 Typical materials used in micro thin films . . . 23

2.2.2 Deflection of the sensing diaphragm . . . 25

2.2.3 Deflection of the middle diaphragm . . . 29

2.3 Capacitance calculation using integration method . . . 33

2.4 Mechanical and electrical characteristics of the Sensor . . . 35

2.4.1 Capacitance-Pressure characteristics . . . 35

2.4.2 Impact of fringe capacitance on C-P characteristics . . . 36

2.4.3 Temperature dependance . . . 39

2.4.4 Sensitivity comparison . . . 41

2.5 Cantilever Middle Plate Sensors: Model 2 . . . 41

2.6 Conclusions . . . 45

3 Geometric Analysis and Design 46

3.1 Design constraints imposed by fabrication technology . . . 47

3.1.1 Materials . . . 47

3.1.2 Diaphragm Dimensions . . . 48

3.1.3 Gap Heights . . . 49

3.2 Effect of Geometrical Parameters on Sensitivity . . . 51

3.2.1 Diaphragm Size . . . 52

3.2.2 Size of Boss Ring . . . 53

3.2.3 Change of Post Size . . . 55

3.2.4 Alignment Error of Boss Ring . . . 57

3.3 Sensor design using a graphical approach . . . 57

3.3.1 Design diaphragm size and gap . . . 59

3.3.2 Determine sizes of boss ring and post . . . 62

3.4 Concluding Remarks . . . 64

4 Analytical Model of the Pressure Sensor **65**
4.1 Introduction 65
4.2 Parameters in the analytical model 66
4.3 Deformation of the Sensing Diaphragm 68
4.3.1 Elastic Model of the Diaphragm 68
4.3.2 Energy Method 70
4.3.3 Analysis of internal stress 73
4.4 Deformation of the Cantilever Middle Plate 74
4.4.1 Circular Model 75
4.4.2 Square Model 82
4.5 Evaluation of Analytical Model 82
4.6 Conclusions 87

5 Sensor Optimal Design using Genetic Algorithm **89**
5.1 Introduction 89
5.2 Basic theory of genetic algorithm 90
5.3 Multi-objective genetic algorithm 91
5.3.1 Data structure of candidate individuals 92
5.3.2 Search space 93
5.3.3 Fitness functions 94
5.3.4 Evolution conditions 94
5.4 Optimization results 95
5.5 Effect of GA varaibles 99
5.5.1 Population size 99
5.5.2 Crossover probability 102
5.6 Conclusions 103

6 Sensor Fabrication and Testing **105**
6.1 Introduction 105
6.2 Fabrication Flow 106
6.2.1 Glass wafer fabrication steps 107

6.2.2 SOI wafer fabrication steps . . . 109
6.2.3 Wafer bonding and backside etching . . . 111
6.3 Fabrication results . . . 113
6.3.1 Glass etching . . . 115
6.3.2 Metallization . . . 117
6.3.3 Thin film deposition . . . 119
6.3.4 Release etching and drying . . . 123
6.3.5 Anodic bonding and backside etching . . . 126
6.4 Test of sensor performance . . . 129
6.4.1 Testing rig . . . 129
6.4.2 Capacitance Measurement using LCR meter . . . 130
6.4.3 Capacitance Voltage conversion . . . 134
6.5 Conclusions . . . 139

7 Conclusions and Suggestions 141
7.1 Conclusions . . . 141
7.2 Suggestions for future work . . . 143

Bibliography 145

Appendix A GUI Method for Capacitance Calculation 157

Appendix B Basic Photo Lithography Process 161

Appendix C MS3110 Measurement Board Calibration 163

List of Figures

1.1 Bulk micromachined structures realized by silicon etching 4

1.2 Typical steps for surface micromachining. (a)sacrificial layer deposition (b)definition of the anchor and bushing regions, (c)structural layer patterning (d)free-standing microstructure after release 5

1.3 Operation of the micro piezoresistive pressure sensor 8

1.4 (a) cross section and (b) top view of micro capacitive pressure sensor 10

1.5 Cross section view of micro resonant pressure sensor 11

1.6 Hydrostatic tank gauging system 13

1.7 Flip-chip configuration, read-out ASIC and top view of pressure sensor for biomedical measurement 15

1.8 Schematic diagram of a capacitive pressure sensor with two deformable electrodes 16

2.1 Schematic view of a capacitive sensor with a cantilever middle plate 21

2.2 The undeformed sensing diaphragm, meshed by ABAQUS 26

2.3 The deformation contour of the sensing diaphragm under a uniform pressure load $10MPa$. $a = 500\mu m, h_{sen} = 20\mu m, d = 75\mu m$ 27

2.4 Stress distribution in the deformed sensing diaphragm 28

2.5 Deflection-Pressure curve of boss ring on the sensing diaphragm . . 28

2.6 The deformation contour of the middle diaphragm at the pressure point $10.8MPa$. $a = 500\mu m, h_{mid} = 1.50\mu m, b = 20.0\mu m, g = 6.0\mu m$ 31

2.7 Stress distribution in the cantilever middle diaphragm 31

2.8 Largest deflection in top sensing and middle plates at the pressure point $10.8MPa$. 32

2.9 Structure of a typical capacitive pressure sensor with an insulating layer . . . 34
2.10 Capacitance-Pressure characteristics of the proposed sensor. $a = 500\mu m$, $h_{sen} = 20\mu m$, $h_{mid} = 1.50\mu m$, $g = 6.0\mu m$, $d = 75\mu m$, $p = 50\mu m$ . . . 37
2.11 A model of parallel plate capacitor constructed in MEDICI. 37
2.12 Fringe capacitance variations with electrode size from 460 to 540μm 38
2.13 Temperature distribution in the sensor structure, $T_{sen} = 40°C$, $T_{mid} = 20°C$ . . . 40
2.14 Capacitance-Pressure characteristics . . . 40
2.15 The three plates capacitive pressure sensor . . . 43
2.16 Capacitance-Pressure Characteristics of Model 2, $\eta = 1.0\mu m$, $d = 75\mu m$, $b = 20\mu m$ . . . 44

3.1 Capacitance-Pressure characteristics for different diaphragm sizes, $\eta = 2.0\mu m$, $d = 75\mu m$, $b = 20\mu m$ . . . 52
3.2 Change of sensitivity upon different diaphragm sizes . . . 53
3.3 Capacitance-Pressure characteristics for different ring sizes, $\eta = 2.0\mu m$, $a = 500\mu m$, $b = 20\mu m$ . . . 54
3.4 The effect of ring size on sensitivity . . . 55
3.5 Capacitance-Pressure characteristics for different post size, $a = 500\mu m$, $d = 50\mu m$, $\eta = 2.0\mu m$ . . . 56
3.6 Effect of changing post size on device sensitivity . . . 56
3.7 Capacitance-Pressure change due to misalignment of boss ring, $a = 500\mu m$, $d = 50\mu m$, $\eta = 2.0\mu m$, $b = 20\mu m$ . . . 58
3.8 Relationship between touch point pressure and the gap for different diaphragm sizes . . . 59
3.9 Relationship between Sensitivity and the gap for different diaphragm sizes . . . 60
3.10 Graphics design tool for the pressure sensor . . . 61

3.11 Sensitivity vs. boss ring size d, for post size b varying from $12\mu m$ to $20\mu m$, diaphragm size $a = 500\mu m$ . . . 63

3.12 Touch point pressure vs. boss ring size d, for post size b varying from $12\mu m$ to $20\mu m$, diaphragm thickness $h_{sen} = 20\mu m$ . . . 63

4.1 The plate with dimensions L and W, exposed to pressure normal to the surface . . . 68

4.2 An element in the plate under applied forces . . . 70

4.3 Deflection profile of a square sensing diaphragm. $h_{sen} = 20\mu m$, $a = 500\mu m$, $P = 10MPa$ . . . 74

4.4 Largest deflection vs. applied pressure. $h_{sen} = 20\mu m$, $a = 500\mu m$ . . . 75

4.5 Cross section view of half circular plate . . . 76

4.6 Forces and Moments acting on an element unit of a circular plate . . . 77

4.7 3-D deformation shape of the top plate calculated by the energy method. side length $a = 500\mu m$, thickness $h_{sen} = 20.0\mu m$, mesh size = $6.25\mu m$, internal stress = $0.5MPa$ . . . 84

4.8 Comparison of diaphragm center deflections using different methods. 84

4.9 3-D deformation of the square middle plate from the interpolation method. side length $a = 500\mu m$, thickness $h_{mid} = 1.75\mu m$, mesh size $s = 6.25\mu m$. . . . 85

4.10 Comparison of sensor characteristics from the analytical model and ABAQUS . . . 87

5.1 The evolution of Pareto front for the multi objective optimization . 96

5.2 Cost value curves in the MOEA evolution, population size 10 . . . 97

5.3 The capacitance-pressure characteristics of the designed sensors . . 98

5.4 Cost value curves in the MOEA evolution, population size 20 . . . 99

5.5 Cost value curves in the MOEA evolution, population size 30 . . . 100

5.6 Deviation of 10 runs in different population size, crossover = 0.7 . . 101

5.7 GA evolution at crossover probability 0.8, population 10 . . . 102

5.8 GA evolution at crossover probability 0.6, population 10 . . . 103

5.9 Deviation of 10 runs in different crossover probabilities, population 20104

6.1 Step height coverage. (a) perfect conformal coverage (b) step coverage as drawn in this work . . . 106
6.2 Glass 1st etching step. (a)Spin coat and pattern PR (b)Glass etching (c)PR striping . . . 108
6.3 Glass 2nd etching step. (a)Spin coat and pattern PR (b)Glass etching (c)PR striping . . . 109
6.4 Metal sputtering on the glass wafer. (a)Pattern PR (b)Sputter Cr/Au (c)PR lift off (d)glass milling . . . 110
6.5 Dielectric layer and Lead formation on a SOI wafer. (a) LPCVD silicon nitride (b) Spin coat and pattern PR (c) Metallization . . . 111
6.6 Silicon oxide deposition and patterning. (a) PECVD oxide (b) PR patterning (c) oxide RIE etching . . . 112
6.7 Polysilicon deposition and patterning, followed by sacrificial etching. (a) PECVD polysilicon (b) PR patterning (c) polysilicon plasma etching (c) sacrificial etching . . . 113
6.8 Wafer bonding. (a)anodic bonding (b)glass grinding . . . 114
6.9 Backside etching (a)PR patterning (b)Deep RIE . . . 114
6.10 PR peel off due to long time wet etching . . . 115
6.11 Glass wafer after 1st etching with PR remained . . . 116
6.12 Glass wafer after e-beam evaporation of Au/Cr . . . 118
6.13 E-beam evaporation Au/Cr film on the SOI wafer . . . 118
6.14 Profile of PECVD oxide layer measured in Dektak profile scanner . 122
6.15 Silicon oxide layer after patterning observed in microscope . . . 123
6.16 Improve release etch property by adding etch holes in polysilicon diaphragm . . . 124
6.17 Damage in nitride layer due to poor selectivity of release etching . . 125
6.18 Sensor device after anodic bonding . . . 128
6.19 Backside of SOI wafer after deep RIE etching . . . 128
6.20 Schematic of pressure sensor test setup . . . 130

6.21 Capacitance-pressure characteristics for sensors with different diaphragm sizes 133
6.22 Characteristics of the sensor with $670\mu m$ diaphragms, comparison between measurement and simulation results 135
6.23 Working theory of MS3110 measurement board 136
6.24 V_{out} vs Differential Capacitance $CS_2 - CS_1$ ($C_{ref} = 0.513pF$) 137
6.25 Voltage output vs applied pressure 138
6.26 Capacitance vs applied pressure, from different methods 139

List of Tables

2.1 Young's modulus, Poisson's ratio in different orientations 24

2.2 Sensitivity comparison between different sensors, electrode length $a = 500\mu m$, electrode gap $\eta = 2.0\mu m$ 41

2.3 Capacitance sensitivity between the middle diaphragm and the substrate, electrode length $a = 500\mu m$, electrode gap $\eta = 1.0\mu m$ 44

3.1 Specifications of standard SOI wafers used in IC industry 49

3.2 Limits on gap heights by processing technologies 50

3.3 Fixed parameters in geometric analysis 51

3.4 comparison of simulated results, FEA and Graphical design 62

4.1 Conditions for Small or Large Deflection Theory 68

4.2 Linear interpolation method using circular models 85

4.3 Comparison of percentage modelling error for different mesh sizes, at touch point pressure $10.0MPa$ 86

4.4 Comparison of pressure sensitivity deviation for different mesh sizes 87

5.1 Evolution of fitness values, population=10, crossover probability=0.7, mutation probability=0.01 97

5.2 Comparison of sensor performances between graphical design and GA optimal design 98

5.3 Effect of population size on GA evolution 100

6.1 Run sheet of major fabrication processes 107

6.2 Specifications of SOI wafer 107

6.3 Etch depths on glass wafer with PR layer 117
6.4 Nitride layer thickness measured by the SENTECH ellipsometer . . 120
6.5 Thickness of PECVD silicon oxide layer measured by profile scanner 121
6.6 Thickness of PECVD polysilicon layer measured by profile scanner . 123
6.7 Percent perimeter occupied by etch holes for different diaphragm sizes 125
6.8 Etch characteristics for different etchant 126
6.9 Bonding parameters for SiN_4 deposited silicon to glass. applied voltage 800 V, bonding temperature: 400^oC 127
6.10 Parasitic capacitance for the testing system 131
6.11 Sensitivity of capacitive pressure sensors obtained from measurement 134
6.12 Calibration data of MS3110 measurement board 137

Summary

The research work reported in this thesis proposes a novel micro capacitive pressure sensor for detecting a small pressure variations ΔP over a large constant load P. As one of the most established areas of MEMS (Micro-Electro-Mechanical Systems) technology, micro capacitive pressure sensors are popular because they provide superior properties such as lower power consumption, larger output range, and less temperature dependence. To meet various measurement requirements in practice, this dissertation assesses the evolving structure and performance of the proposed sensor, from the perspectives of computer simulation, parameters optimization, fabrication and testing, etc.

The potential fields where the proposed device could be applicable include hydrostatic tank gauging, petroleum pipe monitoring and biomedical applications, etc. The proposed sensor fundamentally consists of a sealed chamber with a rigid substrate, and two movable diaphragms which will deform under applied pressure. Simulation experiments have been conducted to identify the theoretically sensor performance. Specifically, mechanical deformation of sensing diaphragm is modelled on the basis of a Finite Element Method, and the geometric data of the deformed diaphragm is then imported into an integration method to estimate changes in the capacitance. Modelling results indicate that the deformation of a thick sensing diaphragm could be magnified after it comes into contact with a thin cantilever middle diaphragm, and thus the sensitivity could be improved by 1364% after the onset touch point.

Compared to conventional parallel plate capacitive pressure sensors, the proposed sensor has more structural parameters so the task of selecting the various

structural parameters is more complex. Based on the FEM simulation results, relationship between the structural parameters and sensor performance have been discussed and a graphical method has been proposed for sensor design. The feasibility of using evolutionary algorithms to optimize the structural parameters is also investigated. First, an analytical model of the proposed sensor that can be conveniently used to evaluate the fitness of the candidate solutions is first constructed using plate theory. The deflection model of the sensing diaphragm is based on energy method in order to consider the effects of internal stress. Theory of plate deflection is then used to model the deflection model of the cantilever middle plate. Results demonstrate that the accuracy of the analytical model is within 3% of the finite element approach. The analytical model is then combined with a Multi-Objective Evolutionary Algorithm package to optimize the sensor structure. After constraining the search space to satisfy fabrication limitations, an optimal structure that provide 65.8% improvement in sensitivity over a graphical design method is evolved.

Finally, the concept of using mechanical amplification to improve device sensitivity is investigated experimentally. The proposed device is fabricated by forming the cantilever middle plate on a SOI wafer using surface micromachining technology, bulk micromachining a pyrex wafer to active mechanical amplification, before forming a sealed chamber using anodic bonding. Using a hydrostatic pressure system, a probe station and capacitance measuring instruments, the device is characterized. Experimental results demonstrate that the sensitivity of a device with $670\mu m \times 670\mu m$ square diaphragm improves from $0.405fF/kPa$ to $3.280fF/kPa$ when mechanical amplification is activated. The data proves that the proposed device is able to provide enhanced sensitivity to small pressure fluctuations in the presence of a relatively large ambient load. The experiment done on a MS3110 measurement board is also presented to find the possibility of converting capacitance change to voltage output.

Chapter 1

Introduction

1.1 Review of MEMS technology

In recent decades, there are dramatic developments in the areas of Micro-Electro-Mechanical Systems(MEMS). MEMS is a new technology that deal with the design and production of movable miniature mechanical devices. MEMS technology integrates micromechanics and microelectronics in their functionality, and often leads to the integration of devices of both kinds into one chip [1].

MEMS components are being used in diverse applications such as mechanical sensors, optical sensors, chemical sensors, projection displays, fiber switches, DNA amplification, medical diagnostics, material testing, lab-on-a-chip, micro robots, and many others[2]. The small size and weight of this products enable sensing and actuation to be incorporated into applications that were not cost-effective or even though of before. Compared with systems in the macro domain, such micro electro-mechanical devices have the advantages listed:

1. Higher performance. As the size of system decreases, the influence of outside disturbance such as temperature, humidity become less troublesome [3][4].

2. More efficient. The transient time is obviously shorter in micro linear dimension. Thus, the system is able to respond more quickly [5].

3. Improved performance. Due to the small volume of micro systems, expensive

materials can be used to obtain desirable properties [6][7].

The micro scale structures and devices have dimensions of micrometers. MEMS technology utilizes the same operational principles and basic foundations as conventional electromechanical systems. In fact, the designer applies the classical Lagrangian and Newtonian mechanics as well as electromagnetics (Maxwell's equations) to study MEMS.

Production costs of MEMS devices are normally much cheaper than that of the macro devices for the same purposes. However, the fabrication equipments cost is very high. A state-of-the-art silicon foundry cost the better part of one billion US dollars. High initial investment is definitively one of the main challenges for anyone who is contemplating industrialization of MEMS. Another challenge is the complexity of the MEMS prototypes design and performance verification. Typical MEMS devices, even simple ones, manipulate energy (information) in several domains: mechanics, electronics and magnetics. The designer must therefore understand, and find ways to control complex interactions between those domains.

Development of MEMS devices often require the fabrication of micromechanical parts, e.g., a diaphragm in the case of the pressure sensor and a suspension beam for many accelerometers. These micromechanical parts were fabricated by selectively etching away areas of the silicon substrate to leave behind the desired geometries. Hence, the term micromachining is used to designate the mechanical purpose of the fabrication processes that were used to form these micromechanical parts.

1.2 Fabrication Techniques

Traditionally, MEMS devices has been built largely upon microelectronics technologies. The main reasons are excellent mechanical properties of silicon [8], and of other materials used in microelectronics field such as polysilicon, oxide and nitride. Besides, many microelectronics processes such as deposition, etching, lithography can be easily adapted for micromachining technology. Micromachining technology has been developed for creating structures of high quality single crystal silicon and

thin film growth and patterning. Micromachining technology is often divided into two categories: bulk micromachining and surface micromachining. It is noted the dividing lines separating these categories are not always clear, since many MEMS devices have elements of both methods.

1.2.1 Bulk micromachining

Bulk micromachining is often described as a subtractive process, where the bulk of the substrate (usually glass or single crystal silicon) is etched, cut, or otherwise modified to make the desired structure. The substrates can be machined by numerous techniques including isotropic etching, anisotropic etching, electrochemical etching, spark machining, mechanical milling, ultrasonic milling, laser and laser-assisted etching, and electro-discharge machining.

Silicon etching method is generally divided into two categories, dry etching and wet etching. There are various types of dry-etch processes, ranging from physical sputtering and ion-beam milling to chemical-plasma etching. Reactive ion etching, the most common dry etching technique, uses a plasma of reactant gases to etch the wafer, and thus is performed at low pressure in a vacuum chamber. Wet etching can also be used on single crystal silicon or gallium arsenide wafers, where the etchant attacks all crystalline plates faster than the $< 111 >$ planes. In silicon, this can be used to create diaphragms, v-grooves and other structures, as shown in Figure. 1.1. Diaphragm thickness can be controlled by using elctrochemical etch stop, or a heavily boron doped etch stop. A wide variety of anisotropic etching solutions can be used, including ethylene diamene pyrocatechol (EDP) and hydrazine. Aqueous hydroxide solutions are also commonly used, including $CsOH$, KOH, $NaOH$ and tetra-methyl ammonium hydroxide ($TMAH$). EDP and KOH are the most widely used and characterized etchants. EDP has the advantage over KOH of better selectivity to the etch mask of SiO_2. However, KOH has superior of $< 100 >:< 111 >$ etch rate selectivity. KOH contaminates silicon with potassium, a known fast ionic impurity in gate oxides of MOS transistors, and causes unwanted threshold voltage shifts. Bulk micromachining can also be defined as the

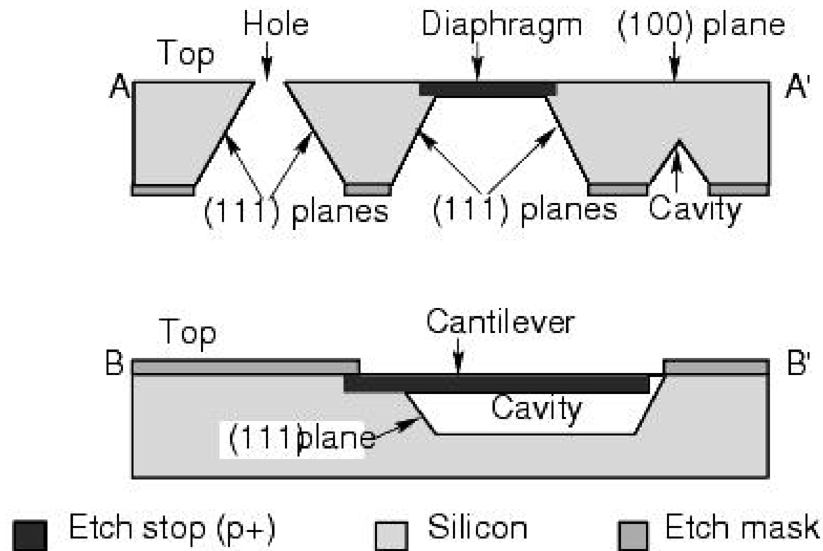

Figure 1.1. Bulk micromachined structures realized by silicon etching

formation of a desired microstructure by utilizing the bulk of a substrate, which is inclusive of wafer bonding technology. The most widespread techniques for bulk micromachining are wet anisotropic etching and wafer bonding. Wafer bonding is the technique of bonding two substrates together. Several techniques for bonding substrates are available to the aspiring micromachining processes. The most obvious technique is to use an adhesive material. Photoresist, polyvinyl acetate (PVA), poly-methyl-methacrylate (PMMA) and die attach epoxies and polymides can be used as gluing materials. Melting dissimilar metals to form a eutectic has also been done [9] [10]. Anodic bonding, sometimes referred to as field assisted bonding, involves bonding an insulating substrate to a conducting substrate by bringing two flat surfaces together and applying voltage and heat. This technique can be applied to glass and metal substrates, glass and silicon substrates, and oxidized silicon substrates. Typical values of voltages and temperature ranges are 500-1500 V and 400 -600 ^{o}C. Anodic bonding and gluing techniques are generally limited to the end of a fabrication sequence because of high temperature degradation or foundry contamination issues.

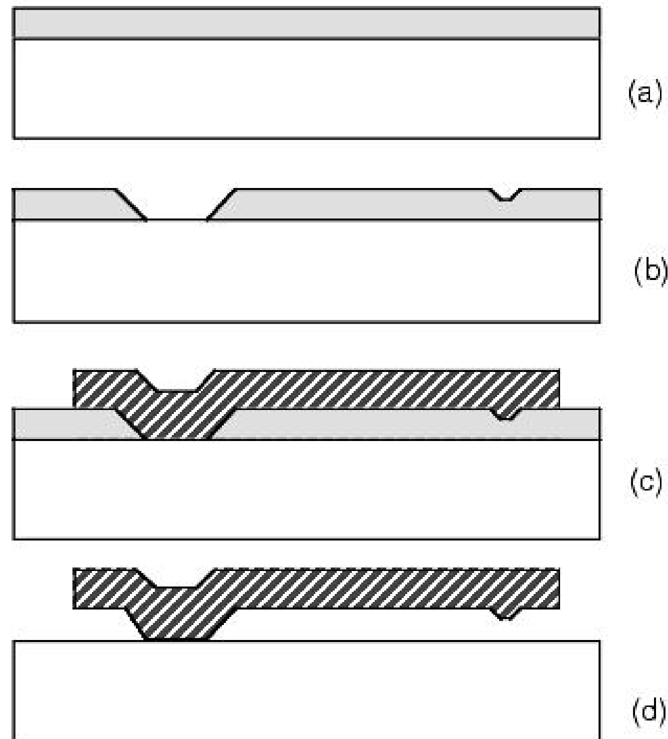

Figure 1.2. Typical steps for surface micromachining. (a)sacrificial layer deposition (b)definition of the anchor and bushing regions, (c)structural layer patterning (d)free-standing microstructure after release

1.2.2 Surface micromachining

In contrast to bulk micromachining, surface micromachining is often described as an additive technology. Typically, the desired microstructure is built by depositing and patterning thin films (less than 10 μm) of structural and sacrificial materials on surface of the substrate. Figure. 1.2 shows the process flow of surface micromachining. First, the sacrificial layer is deposited and patterned. Then, the structural layer is deposited and patterned. Finally, the sacrificial layer is etched to leave a free standing cantilever. The principle advantages of surface micromachining over bulk micromachining are size and dimension control. Due to the nature of anisotropic etching, a bulk micromachined diaphragm assembly must be at least the diaphragm size plus approximately two times the thickness of the wafer. Therefore, the dimensions of a bulk micromachined diaphragm depend on wafer thickness, which

is not always well controlled. Furthermore for a bulk micromachined part, there can be more complexity of aligning front side structures to the diaphragm that created by backside etching. The surface micromachined diaphragm assembly can be much smaller, approximately the diameter of the diaphragm itself. However, the mechanical properties of a deposited surface micromachined diaphragm will, in general, not be as uniform and repeatable as a high quality, single crystal, bulk micromachined diaphragm.

1.3 Review of micro pressure sensors

Since micromachining technology was first developed, various micromachined mechanical transducers have been developed and demonstrated. Examples include gyroscopes, pressure sensors and flow sensors. MEMS sensors are cheaper, faster and simpler, more efficient and reliable than conventional macro sensor [11]. Nowadays, MEMS-based sensors are a crucial component in automotive electronics, medical equipment, smart portable electronics, robotics and hard disk drives. Pressure sensor is one of the most established areas of MEMS technology. Micro pressure sensors began in the automotive industry especially for crash detection in airbag systems. Throughout the 1990s to today, the airbag sensor market has proved to be a huge success using MEMS technology. MEMS-based pressure sensors are now becoming pervasive in everything from inkjet cartridges to blood pressure testers.

Pressure transduction is the means by which the mechanical energy from the pressure is transformed to a form of electrical signal, such as current, voltage and capacitance. Various sensing techniques and designs have been used to develop new and improved micro pressure sensors. An example is a strain gauge, which transforms strain into a change of electrical resistance. There are some other methods of transduction that are based on fundamental physical laws, such as piezoresistive, capacitive or resonant phenomena. The various types of micro pressure sensors is discussed in this section.

Micro pressure sensors are one of the earliest and largest research areas in MEMS and it has been in existence almost since the inception of microelectron-

ics and integrated circuit (IC) technologies. The discovery of the piezoresisitive effect in silicon and germanium in 1954 [12] is commonly cited as the stimulus for silicon-based sensors and micromachining. Silicon piezoresistors were bonded to metal diaphragms to create pressure sensors in the late 1950s. Even as early as the 1960s, different techniques for bulk and surface micromachining were emerging. The Resonate Gate Transistor of Nathanson and Wickstrom in 1965 [13] is widely recognized as one of the first applications of a micromechanical device on a silicon substrate. The first monolithic integrated pressure sensor with digital (i.e., frequency) output was designed and tested in 197l at CWRU [14]. To achieve better sensitivity and stability, capacitive pressure sensors were first developed and demonstrated at Stanford University in 1977 [15]. The first integrated monolithic capacitive pressure sensor was reported in 1980 [16]. Petersen provides an excellent overview of the wide variety of silicon applications in mechanical devices including pressure sensors [17].

1.3.1 Micro piezoresistive pressure sensor

Piezoresistance is the property where the resistivity of a material changes due to an applied strain. The resistivity change is generally linear with strain. While piezoresistivity is present in most metals, the piezoresistive effect in semiconductors is stronger by up to two orders of magnitude[18]. The large effect in silicon (Si) and germanium (Ge) is due to electronic band deformation and redistribution of carriers within the various conduction and valence bands.

Piezoresistance is useful whenever a direct strain is to be measured, or when a physical variable can be related to strain. A typical piezoresistive pressure sensor structure is shown in Figure. 1.3. A thin conductive wire is cemented into the diaphragm. When external force flexes the diaphragm, the conductive wire deforms to produce a resistance change. Simultaneously, the values of resistors in the Wheatstone bridge changes. Thus a bridge voltage can be measured as a function of the pressure.

The linearity of the piezoresistive sensor output can be quite good, when the

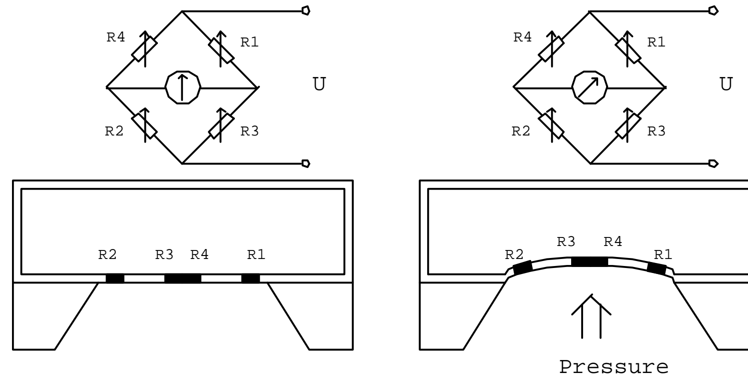

Figure 1.3. Operation of the micro piezoresistive pressure sensor

elastic limits of the diaphragm are not exceeded. It is also necessary to ensure that the diaphragm deformation is only in a small range compared to the diaphragm dimension, because the effect of nonlinearity may occurs for large deformation. Furthermore, it must be noted that hysteresis, nonlinearity, non-repeatability and creep have a significant effect on the output readings in the piezoresistive sensors. It was also found that piezoresistive sensors were very sensitive to interference, such as sideways forces, making them inaccurate for many biomedical applications [19].

1.3.2 Micro capacitive pressure sensor

Piezoresistive sensors are low cost, but they require extensive calibration and compensation procedures due to small output swing ($10 - 100mV$) and large thermal drifts. To address these limitation, many micromachined pressure sensor using the capacitive sensing method have been proposed, since capacitive sensors have more controllable characteristic and larger output range[20][21][22]. In general, capacitive pressure sensor are more sensitive to pressure than the piezoresistive ones [23]. Moreover, capacitive pressure sensors generally have less temperature dependance[24].

The typical working theory of a micro capacitive sensor is to detect the gap changes between two electrodes [25]. They are based on parallel plate capacitors, usually with one plate fixed and the other moving. The capacitance, C, of a parallel

plate pressure sensor is given by:

$$C = \frac{\varepsilon A}{d} \tag{1.1}$$

where ε, A and d are the permittivity of the gap, the area of the plates, and the separation gap of the plates, respectively. Changes in pressure cause one of the plate to deflect and change the capacitance. From Equation (1.1), the capacitance change is proportional to pressure and is typically a few percent of the total capacitance. The capacitance can be monitored by using it to control the frequency of an oscillator or to vary the coupling of an AC signal. It is good practice to keep the signal-conditioning electronics close to the sensor in order to mitigate the adverse effects of stray capacitance.

The micromachined capacitive pressure sensors typically have capacitances of only a few picofarads, making them susceptible to signal loss through parasitic capacitances [26]. This problem can be mitigated by increasing the area of the sensor, but leads to increases in the die size and sensor cost. For these reasons, capacitive sensors have historically been passed over in favor of piezoresistive sensors. However, improvements in analog circuits and the monolithic integration with capacitive sensors have overcome many of the problems and have made capacitive sensors an attractive technology [24]. One approach is to construct an identical reference device with no diaphragm is next to the sensing capacitor for a parasitic insensitive capacitance measurement scheme [8], as shown in Figure. 1.4. When the pressure is applied on the sensing device, the difference between reference and sensing devices are measured and used as the output. By these means, the effect of parasitic capacitance and thermal stress has been removed greatly.

1.3.3 Micro resonant pressure sensor

Another type of pressure sensor relies on vibrating elements for measurement of pressure. The sensors operate by monitoring the resonant frequency of an embedded doubly clamped bridge [27][28][29], or a comb drive [30]. A typical micro resonant pressure sensor is shown in Figure. 1.5, which consists of a thick outer

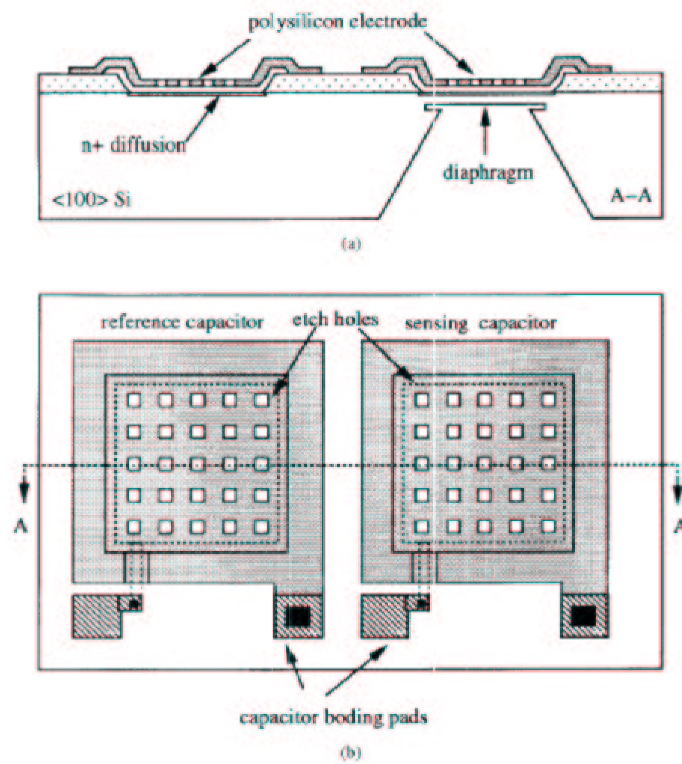

Figure 1.4. (a) cross section and (b) top view of micro capacitive pressure sensor

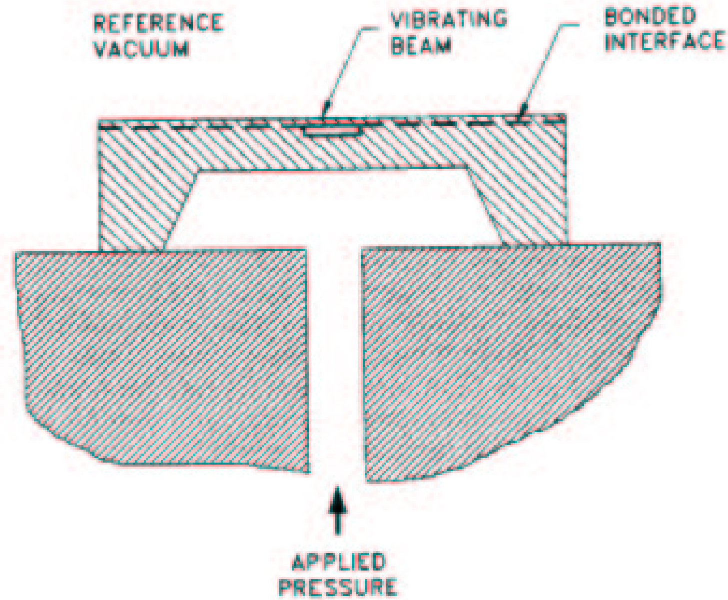

Figure 1.5. Cross section view of micro resonant pressure sensor

frame, a thin inner diaphragm, and a thin doubly supported silicon beam positioned in the center [27]. The resonant beam is on top of the diaphragm and it acts as a sensitive strain gauge. As the stress state of the diaphragm changes, the tension in the embedded structures changes and so does the resonant frequency.

The beam is excited into resonance by applying an AC voltage through the electrodes beneath the silicon beam. The beam vibrates at its natural frequency according to its tension, which varies with pressure. Thus, pressure may be calculated by measuring the frequency of vibration of the beam. Such frequency measurement is commonly carried out by electronic circuits (oscillator amplifier and frequency converter) integrated into the sensor cell. The resonant beam can also be optically excited by laser and sensed by a photo detector [31], or electrostatically excited and capacitively sensed [30].

Resonant pressure sensors have been shown to exhibit better pressure sensitivity and lower temperature sensitivity than pure pressosensitive sensors. Furthermore, a frequency output is more robust to disturbance than classical analog piezoresistive and capacitive signals[27][29].

The resonant beam needs an excited signal, as well as an electrical circuit

to measure the vibration frequency. These parts usually make the pressure sensor more complex in design and fabrication. Furthermore, the vibration of the resonant beam will be greatly affected for large diaphragm deformation. Thus, the working range of the resonant pressure sensors is limited, compared to that of piezoresistive or capacitive sensors.

1.4 Motivations

As discussed in previous section, most sensors for greater-than-atmospheric pressure utilize the characteristic of deformable diaphragms. However, for large pressure applications, the sensing diaphragm must be thick enough to handle the high pressure load. On the other hand, the sensitivity of these pressure sensors must also be high enough to detect small pressure variations caused by leakage or other disturbances. In order to address this problem, an approach is needed to enhance the sensitivity while keeping the ability to sustain high ambient pressure. The sensitivity enhancement approach will be useful to many pressure applications such as tank gauging, pipeline pressure measurement and biomedical applications, etc.

1.4.1 Hydrostatic Tank Gauging

Despite various types of micro pressure sensors, few are sensitive to small pressure variations in a high pressure ambient. Sensors capable of measuring $P+\Delta P$, where $P >> \Delta P$, accurately are useful for the specialized application of hydrostatic tank gauging (HTG) [32]. Tank gauging is the generic term for the quantity assessment of liquid products in bulk storage tanks. Hydrostatic tank gauging (HTG) is a pressure-based tank gauging system, and the typical structure is shown in Figure 1.6. Hydrostatic tank gauging systems operate on the principle that the pressure at the bottom of the tank varies with the liquid in the tank. In Figure. 1.6, pressure sensors on the dip tube are submerged into the bottom of the tank, and the readings at the digital gauge are used to indicate tank contents and liquid height level.

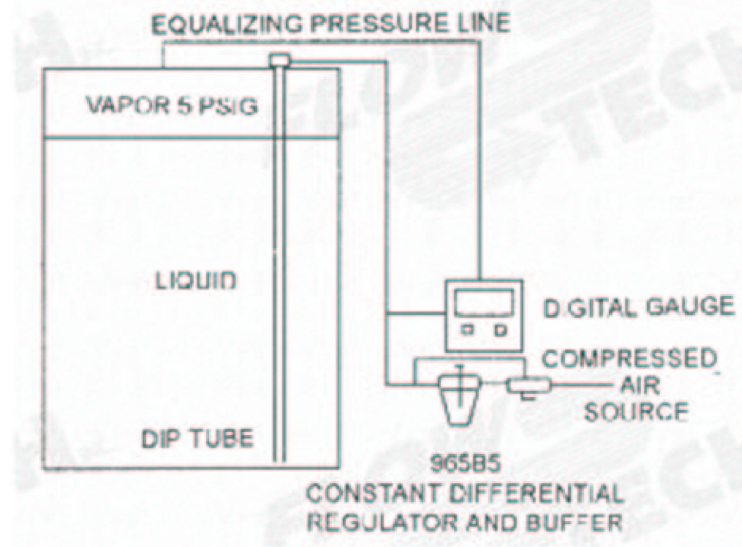

Figure 1.6. Hydrostatic tank gauging system

Micro pressure sensors and mechanical gauges are used in this application because of their simplicity of installation and calibration, and because of their high accuracy at a low price. These pressure gauges are normally designed to measure liquids having high constant specific pressure in the tanks. Thus, they cannot response promptly to some changes in the tanks, such as the liquid level variation due to leakage, or the liquid density change because of incoming moisture. By applying the idea of sensitivity improvement, it may be possible to detect small pressure variations in a certain high pressure environment, thus helping to detect leakage or density monitoring in HTG area.

It is a method to accurately gauge liquid inventory and to monitor transfers in tank farms and similar multi-tank storage facilities. Increasingly, HTG systems are also employed for storage tank leak detection [33]. Traditional HTG installations involve disrupting the integrity of the tank wall in three or more places to mount multiple pressure and temperature sensors. Each sensor is a complex combination of electrical and mechanical components. Microelectromechanical Systems technology offers a means of eliminating the need for multiple sensors as it allows on-chip integration of pressure and temperature transducers.

1.4.2 Pipeline monitoring

Piping transporting are normally used for crude oil, natural gasoline, natural gas liquids, liquefied petroleum and alcohol, etc. Pipeline consists of pipe, flanges, bolting, gaskets, valves, fittings and the pressure containing parts of other piping equipment. Liquid may be injected or stripped at various locations along the pipeline. Pressure sensors are commonly used for quickly calculating the inlet or outlet pressure of a pipe segment for a given flow rate. The pipeline pressure profile are monitored and used as a reference guide for each pump station.

The idea of monitoring small variations in the large pressure environment can be applied to monitor leaks in the pipelines due to corrosion or defect. A leak in a segment of the pipeline may result in the a small change in pressure readout. To locate the leakage points within 5 minutes as required, pressure sensors with the capability of detecting a transfer pipeline pressure variation caused by 2 % change of the design flow rate.

1.4.3 Biomedical applications

MEMS capacitive pressure sensors are widely used in biomedical applications due to its advantages of miniaturization, low power consumption, ease of measurement and telemetry [34]. The pressure sensor is designed to operate in a pressure range of $0 \sim 300mmHg$ and is targeted for biomedical application of blood pressure or heart beat rate sensing [35]. Present pressure sensors typically utilizes parallel plate capacitors, which are large in size and are required to be operated in touch mode for good linearity.

Figure. 1.7 shows one of the pressure sensors in biomedical applications. The capacitive pressure sensor comprises a pressure dependent capacitance $C_x = C_0 + \Delta C$ and a pressure reference capacitance C_0 for cancelling out the offset capacitance. To build a sensor for measurement of absolute pressure the reference pressure inside the sealed micro-cavity is kept well below $100Pa = 1mbar$ [36]. The readout circuit is a micro-power with $100\mu A$ and $3.5V$. A capacitive measurement range of $600fF$ are achieved and processed by the signal preprocessing circuit. The output

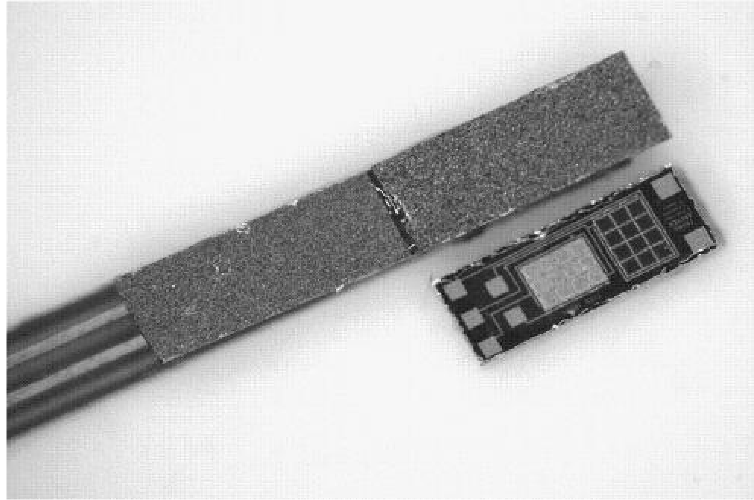

Figure 1.7. Flip-chip configuration, read-out ASIC and top view of pressure sensor for biomedical measurement

of the signal preprocessing is transmitted via a flexible foil carrier based cable to the telemetry unit placed under human skin. In biomedical practice, it will be very useful to have a very sensitive measurement for ΔC, so that to detect in time the slight changes in human body. Differential pressure sensing method may help to address this concern, but the applications of body test are normally absolute pressure measurement. By utilizing the proposed idea of mechanical magnification in this work, it is possible to performance such measurement even in the absolute pressure environment.

1.5 Contributions

Despite the wide applications of micro pressure sensors, few are sensitive to small pressure variations in a high pressure environment. As described in previous section, there is a need for pressure sensors which can accurately measure $P + \Delta P$, where $P >> \Delta P$, in specialized applications, such as HTG, pipeline monitoring and Biomedical. For example, typical constant pressure load in Hydrostatic tanks is $P = 10MPa$, and the pressure variations is $\Delta P = 70kPa$.

The objective of the thesis mainly focus on designing, optimizing and fabricating a new type of MEMS capacitive pressure sensor that can address the require-

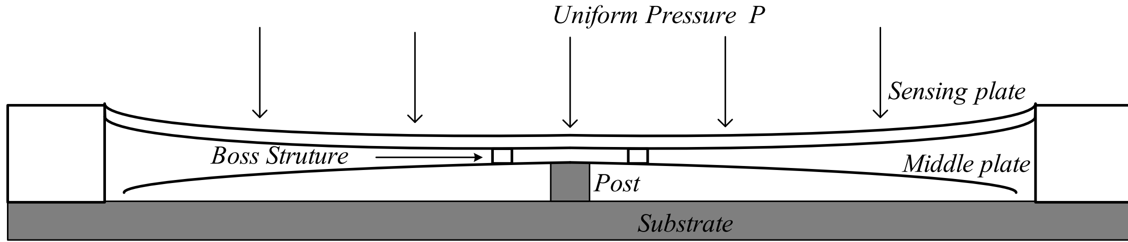

Figure 1.8. Schematic diagram of a capacitive pressure sensor with two deformable electrodes

ment. Since the sensitivity is normally low for a pressure sensor that can sustain high pressure load, the core idea is to magnify the sensitivity as much as possible. By the means of mechanical magnification structures, the deformation of a certain diaphragm can be enlarged, thereby leading to bigger changes in the capacitance of a device that uses this diaphragm as one of the electrodes. Based on the idea of sensitivity enhancement, a novel capacitive pressure sensor with two deformable electrodes and a rigid substrate is proposed, as the schematic diagram shown in Figure. 1.8. In contrast to normal parallel capacitive pressure sensor, the new sensor have a relatively large capacitance-pressure change after a certain threshold pressure value.

The contributions of the research presented in this thesis includes:

- Proposing a novel structure for capacitive pressure sensors. With two movable diaphragms and the magnification mechanism in between, the pressure sensor has an advantage of measuring small variations under a large pressure ambient.
- Providing a simple graphic design tool for the proposed sensor. By using the experiment graph, it is possible to find a sensor geometry that satisfy the requirement.
- Presenting an analytical model based on energy method and nonlinear theory. The deformation of different diaphragms and their interactions in between are researched and modelled respectively. The result of the analytical model shows a quite good agreement with the finite element analysis.

- Using genetic algorithm to optimize sensor parameters based on the analytical model. There are two objectives are to fulfilled, including sensitivity and touch point pressure, so the optimization is a multi-objective process. The optimization procedure will help to found the global minimum points of the design space and its results are used for further fabrication steps.

- Using a combination of bulk and surface micromachining processes to fabricate the sensor, and testing the sensor performance in a hydro pressure system. All fabrication steps as well as the process conditions, recipes and experiments are discussed. Proof of concept data is presented to demonstrate the feasibility of using sensitivity enhancement concept to detect small pressure changes. Further works are discussed to improve the sensor performances.

Although discussions have focused on high pressure applications, it should be noted that the magnification effect in the diaphragm deformation may also applied to other applications where high sensitivity are required. Examples include biomedical areas or automotive engine control.

1.6 Organization of the Thesis

The thesis is organized as follows. Chapter 2 focuses on simulating a novel micro capacitive pressure sensor with two movable diaphragms, including a thick clamped edge sensing diaphragm and a thin cantilever middle diaphragm. The deflection of the sensing diaphragm is passed to the cantilever diaphragm, and the deflection is enlarged in the cantilever structure. The simulation study begins by analyzing diaphragm deformation behavior, by means of the Finite Element Method, ABAQUS. With the exported geometry of deformed diaphragms, changes in the sensor capacitance due to the applied pressure are calculated by the integration method.

Chapter 3 is devoted to sensor parameter analysis and graphic design. Based on the simulation results in Chapter 2, the relationship between the structural

parameters and the performance of the proposed sensor are studied. A graphical design method is presented to select the proper sensor parameters that will meet the design requirements.

Chapter 4 concerns with the construction of the sensor analytical model. The deformation models of clamped sensing diaphragm and cantilever middle diaphragm are both presented. The analysis results are compared with that of finite element model, so as to verify the accuracy of the analytical model.

Chapter 5 investigates the feasibility of using genetic algorithm to optimize sensor structure. Multi Objective Evolution Algorithm (MOEA) is used to solve the optimal design problem in order to meet two major objectives, including touch point pressure P_t and sensitivity S in the working range. The effect of genetic algorithm variables, and the deviations of the genetic evolution are also discussed.

Chapter 6 describes the fabrication steps of the pressure sensor. The process flow is described by using schematic views of main processing steps. The conditions and results in each fabrication steps are discussed in details. The sensor performance is characterized by using a hydrostatic pressure system, and compared with simulation results.

Finally in Chapter 7, conclusions are drawn for the research of sensor simulation, design, fabrication and testing. Suggestions and Further studies for improving the sensor performance and widening the application areas are also presented.

Chapter 2

Simulation of Micro Sensors with Two Deformable Diaphragms

MEMS products are generally superior to the macro devices for the same purpose. Since the fabrication cost for MEMS device is high, and usually MEMS prototypes design and performance verification are complex, fast but accurate simulations are normally used to provide valuable information for verifying the characteristics of the micro devices at concept level. Thus, simulating MEMS devices performance using computer software or other related analytical methods is desirable because of the ease of use and the insight they provide to the designer.

Typically, micro pressure sensors are formed by micromachined technology including film deposition, etching and bonding etc. Micro capacitive pressure sensors, which is the focus of the work, measure the diaphragm deflection directly, so correct analysis of the diaphragm deflection and deflection shape is of importance. Several papers have studied the deflection characteristics of micromachined diaphragms [8] [37]. Capacitive based devices measure diaphragm deflection directly, so deflection and deflection shape is of importance to characterize the device performance. In general, analytical and exact solutions for diaphragm behavior are desirable because of their ease of use and the insights they provide. Specific geometric effects can be ascertained from these solutions. However, these solutions are generally only applicable for small deflection cases. Numerical techniques, such as Finite

Element Method, Boundary Element Modelling, and Finite Difference Modelling, can be more accurate in predicting deflection behavior [38].

In this chapter, the schematic structure of a micro capacitive pressure sensor with two deformable plates is first introduced, regarding the desired ability of measuring a small variation over a constant pressure ambient. Then with the help of Finite Element Methods, the deflection behavior of micromachined diaphragms are investigated. The extension of the deformed model to a capacitance computation is also presented which accounts for electrical performance of the sensor. Another pressure sensor model of the same amplification concept is also simulated. This model provide an alternative way to construct the pressure sensor.

2.1 Sensor Structure

Typically, a capacitive pressure sensors consists of two electrodes, a deformable sensing diaphragm and a rigid substrate. The sensing diaphragm electrode deforms due to the applied pressure, resulting in a capacitance change. In order to withstand the high constant ambient pressure, the sensing diaphragm of pressure sensor should be sufficient thick. The results in small diaphragm deflection, thereby reduce the sensitivity of the device to small pressure fluctuations.

This leads to small deflections in the diaphragm and the deterioration of the sensitivity. To improve the response of the sensor to small pressure changes while withstanding relatively high ambient pressure, a novel design that comprises of two deformable plates is proposed [39]. The two movable electrodes are a thick sensing plate and a thin middle plate. In order to amplify the the small deflection changes in sensing plate, the middle plate is structured as a cantilever. The schematic structure is shown in Figure. 2.1. When the sensing plate deforms according to the applied pressure, the boss ring attached to the sensing plate will touch the middle plate and make it deform as well. The touch point pressure, P_t, is defined as the pressure point when the boss ring come into contact with the middle plate. Since the middle plate is a thin cantilever plate with free standing edges, its deflection due to the contact with the boss ring is magnified and reaches the maximum value

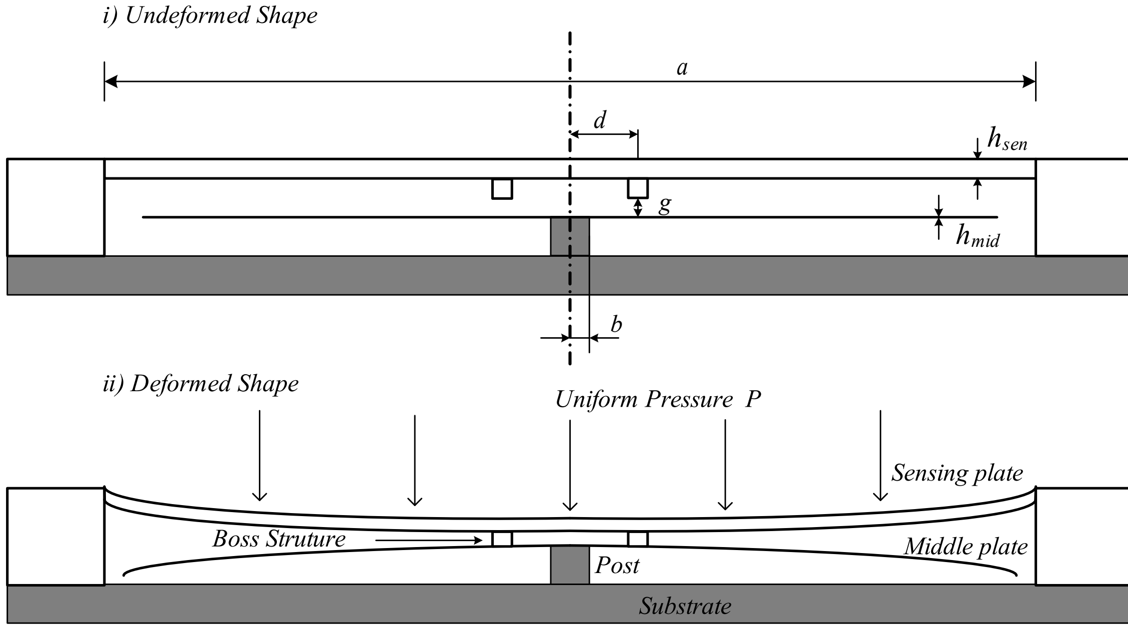

Figure 2.1. Schematic view of a capacitive sensor with a cantilever middle plate

at the edges. In this way, the small deflections in the sensing plate are enlarged in the middle plates, and therefore the change in capacitance between the middle plate and substrate may be enhanced. From Figure. 2.1, some important geometrical parameters of the proposed sensor are as follows:

- Initial gap height $g = 6.0\mu m$;
- Sensing plate thickness $h_{sen} = 20\mu m$;
- Middle plate thickness $h_{mid} = 1.50\mu m$;
- Side length of both diaphragms $a = 500\mu m$;
- Half length of the post $b = 50\mu m$;
- Half length of the boss ring $d = 75\mu m$.

The proposed capacitive pressure sensor manipulates energy in the mechanical and electrical domains. Thus, there is a need to perform both mechanical and electrical analysis properly. In general, the steps that need to be considered in order to model the sensors performance are as followed:

1. Simulating deflection behavior of the sensing and cantilever diaphragm under certain pressure loads and boundary conditions.

2. Interactions and contact analysis between boss ring and the cantilever diaphragm

3. Converting diaphragm's geometrical deformations into capacitance changes

Both the sensing and cantilever middle plate are micro machined thin films fabricated by bulk or surface micromachining technology. Therefore, understanding of the typical materials of micro thin films and the diaphragm behavior is necessary for designing and evaluating the cantilever pressure sensor's performance. There are several works studying the deflection properties of micromachined diaphragms [40] [41]. The finite element analysis software, ABAQUS, is employed to simulate plate deflections in section 2.2. The simulation of electrical property focus on the capacitance change due to plate deformation. Several capacitance computation methods are discussed in section 2.3.

2.2 Analysis of diaphragm deformations

In general, analytical and exact variational solutions for diaphragm behavior are desirable, and specific geometric effects can be ascertained from these solutions. Unfortunately, these techniques are only applicable for cases with simple load and boundary conditions. In the proposed sensors, where complex contact interaction between two diaphragms occurs, Finite Element Method is a more straight forward approach in predicting complex deflections behaviors of diaphragms. The diaphragms can be regard as an assemblage of finite, sufficiently small elements, which are properly connected with each other. The trial functions for those small elements are defined locally, and they must fulfill the connection or boundary requirement in which they are defined. The trial functions are solved in an iteration way and the unknown field function can be approximated by a series of trial functions on each element. This computational procedure can be achieved by the use of a computer software, ABAQUS.

ABAQUS is a suite of powerful engineering simulation programs, based on the finite element method, that can solve problems ranging from relatively simple linear analysis to the most challenging nonlinear simulations [42]. It has an equally extensive list of material models that can simulate the behavior of most typical engineering materials including metals, silicon, polysilicon, silicon dioxide and nitride. Designed as a general purpose simulation tool, ABAQUS can be used to study more than just structural (stress/displacement) problems. It can also simulate problems in such diverse areas as heater transfer, thermal analysis of mechanical components, piezoelectric analysis and acoustics.

2.2.1 Typical materials used in micro thin films

Typically, micro pressure sensors are produced by utilizing silicon based fabrication technologies, such as etching, deposition, etc. There are two ways to form the diaphragms of a sensor. One way is bulk micromachining, where the bulk of the substrate, usually single crystal silicon is etched, cut, or otherwise modified to make the diaphragm. Another approach is surface micromachining, where the desired diaphragm is built by depositing and patterning polysilicon films as well as removing sacrificial materials. Therefore in the diaphragm simulation, it is helpful to understand the properties of the typical materials: silicon and polysilicon.

Single Crystal Silicon

Single crystal silicon has a conventional unit cube structure with 8 atoms per cell [43]. The mechanical property of silicon is stiffer than stainless steel, and does not yield before fracturing. This means single crystal silicon is brittle, but exhibits low hysteresis. Moreover, its linear limit extends nearly to the fracture point, an asset for many micro mechanical devices. Basically, four properties are need to be considered in designing micro structures from thin films. These are Young's modulus, Poission's ratio, Temperature Effect and Fracture point.

From Hooke's law for linearly elastic material, the strains in one direction are functions of stress in that direction as well as stresses in other directions. Young's

modulus E is defined as the proportionality constant between a uniaxial stress in a particular direction and the strain which results in the same direction, with all other stress zero. Materials compressed by stress in one direction undergo expansion in orthogonal directions. Poisson's ratio is defined as the negative ratio of the strain in one orthogonal direction to the strain in the stress direction.

Direction	Young's modulus E (GPa)	Poisson's ratio υ
[100]	130.1	0.2783
[110]	169.1	0.2783
[111]	187.9	0.2618

Table 2.1. Young's modulus, Poisson's ratio in different orientations

Both Young's modulus and Poisson's ratio vary with directions for single crystal silicon, as well as for other crystalline materials. The values are given in Table 2.1. The temperature effect of the stiffness coefficients for single crystal silicon has been measured by McSkimin, et.al.[44]. The effect of increasing temperature on Young's modulus is to reduce it, or soften the material.

Polysilicon

Polysilicon is also an excellent choice for fabrication of MEMS devices. High quality films of polysilicon can be deposited using Low Pressure Chemical Vapor Deposition (LPCVD) techniques. Polysilicon consists of grains of single crystal material with grain boundaries. Grains size as well as surface texture is determined by temperature, pressure and deposition rates. The grains have particular orientations, and there may be a major orientation for a particular Polysilicon film.

Polysilicon films have mechanical characteristics highly dependent on deposition conditions and annealing [45][46]. Different researchers have reported a Young's modulus ranging between 140 to 210 GPa, with these values having a dependence on crystal structure and orientation. Polysilicon films exhibit preferential grain orientations that vary with temperature. Since an ideal film does not exhibit orientation dependence for its mechanical properties, depositing polysilicon films at

590^oC, which is the transition point between polysilicon and amorphous silicon, is an effective method of producing an isotropic film of polysilicon. At this temperature, the amorphous silicon will recrystalize during annealing, which produces films with a nearly uniform Young's modulus of 165 GPa and a poisson's raito of 0.22.

For polysilicon material, the fracture strength is decided by two factors, the grain size, d_g, and the fracture surface energy, γ_s. Griffiths equation shows that the fracture strength of polysilicon is [47]:

$$\sigma_f = \sqrt{\frac{4E\gamma_s}{\pi d_g}} \tag{2.1}$$

Since the size of a dislocation is usually governed by the grain size, larger grains will be stronger due to the increased energy needed to propagate a crack across the material. In several studies, the average fracture strength of polysilicon has been found to be between 1.08 to 1.25 GPa [48], which is clearly less than that of single crystal silicon.

Diaphragm simulation requires the ability to predict the strength of load-carrying components with stress concentrations. Polysilicon is brittle materials but it exhibit higher fracture strengths when smaller volumes or areas are involved. The fracture strengths of polysilicon varied from $2600MPa$ [49] to $3445MPa$ [50], due to different fabrication conditions.

2.2.2 Deflection of the sensing diaphragm

As shown in Figure. 2.1, the edges of the sensing diaphragm are clamped and the pressure is uniformly exerted upon the sensing diaphragm. In ABAQUS, the model of sensing diaphragm is constructed and it consists of two parts: a square plate and a square boss ring. The ABAQUS result was obtained by meshing the diaphragm uniformly using quadrilateral shell elements S8R5, with 8 nodes for each element. Constructing and simulating the diaphragm model deformation in ABAQUS take the following steps:

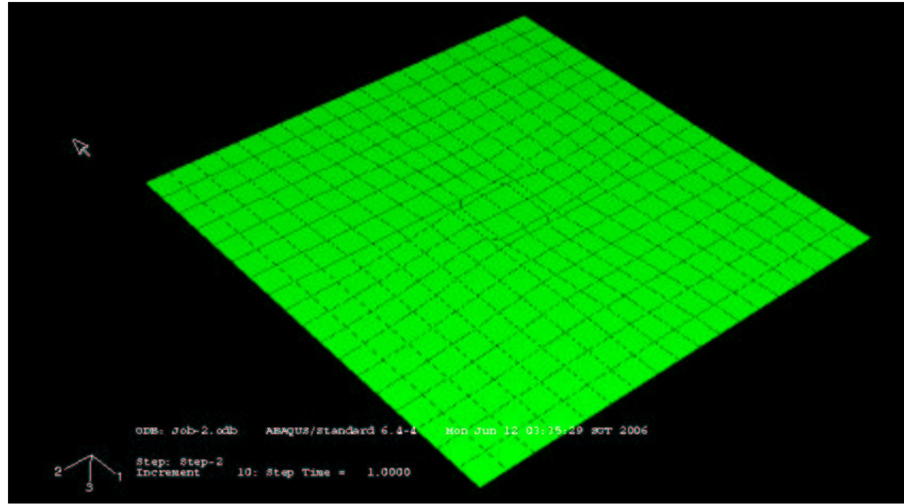

Figure 2.2. The undeformed sensing diaphragm, meshed by ABAQUS

1. Constructing model geometry. An square solid part is constructed to represent the sensing diaphragm. It has a side length of $a = 500\mu m$ and a thickness of $h_{sen} = 20\mu m$. From the solid part, an extruded structure that represent the boss ring is sketched, and its half length is $d = 75\mu m$. The symbols of these parameters have already been defined in section 2.1. Figure. 2.2 shows the undeformed shape of the plate model after mesh creation. The protruding section near the center plate indicates the boss ring underneath.

2. Creating a material property section. An isotropic material section named silicon is defined. As shown in Table. 2.1, Young's modulus is 130GPa, and Poisson's ratio is 0.28. The residual stress in the diaphragm is assumed to be zero. The material section is assigned into the whole diaphragm.

3. Defining analysis steps. The deformation of diaphragm is a non dynamic process at a equilibrium point, so a general static analysis is used. General static analysis can contain different analysis procedures, including plate deformation in the elastic region, the nonlinear region when pressure further increases, and the case of applying temperature field.

4. Applying a boundary condition and pressure load. All four edges are selected as boundary regions and "Encastre" is toggled on because it is assumed that

the edges of the diaphragm are clamped. The encastre boundary condition constrains all active structural degrees of freedom in the specified region. After the region is meshed and the analysis is performed, the constraint will be applied to all the nodes that occupy the region. The magnitude of the pressure load is $10MPa$ and the distribution of the pressure is uniform upon one of the diaphragm surfaces.

5. Meshing the model and submit analysis job. Element size is an important factor to the correct analysis results. In Figure. 2.2, the mesh size is $30\mu m$.

The deformed shape of the diaphragm under a uniformly applied pressure load of $10MPa$ is shown in Figure. 2.3. It can be seen that the displacement contour curves tends to be circles while the diaphragm displacements increase gradually from the edges to the center. Figure. 2.3 also shows that the displacement at the diaphragm edges are much smaller, and the largest displacement ($6.608\mu m$) is located at the center.

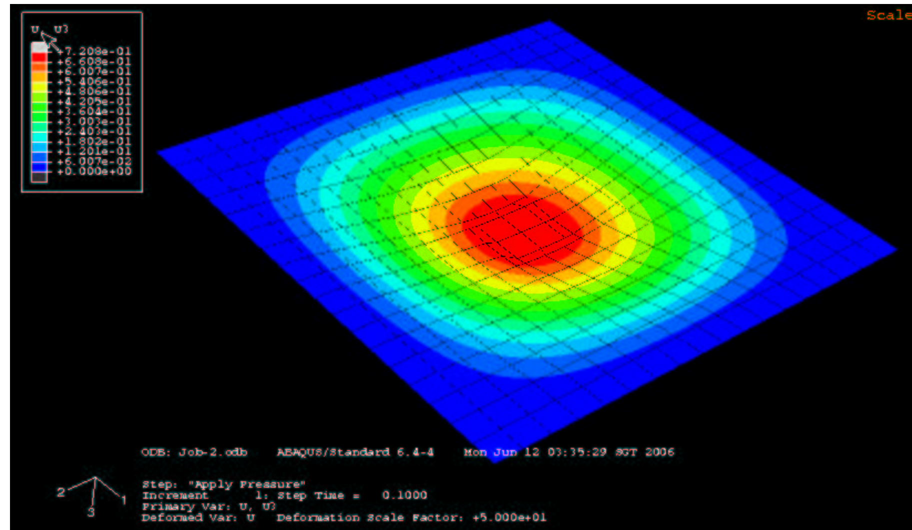

Figure 2.3. The deformation contour of the sensing diaphragm under a uniform pressure load $10MPa$. $a = 500\mu m, h_{sen} = 20\mu m, d = 75\mu m$

The proposed pressure sensors need to be designated to withstand high pressure loads, which exert large stresses in the diaphragms. When the stress at any point on the diaphragm exceeds the material rupture stress, it can damage the diaphragm

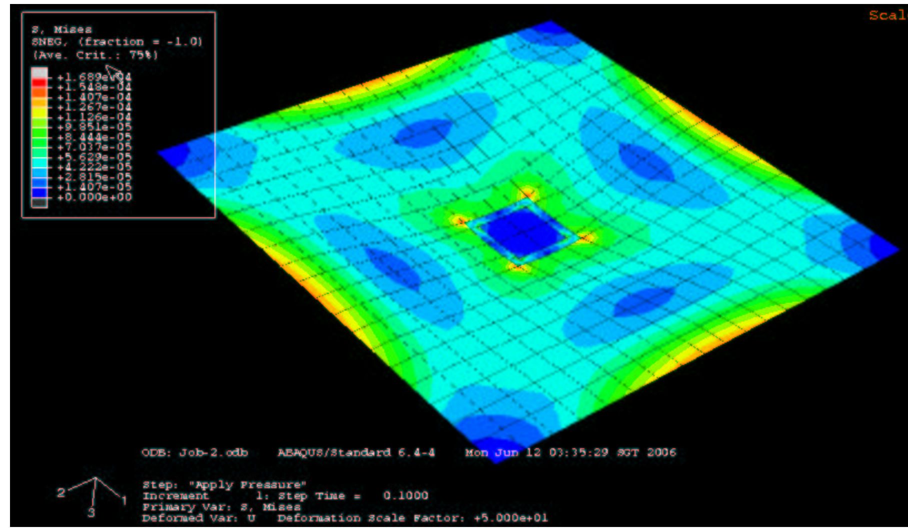

Figure 2.4. Stress distribution in the deformed sensing diaphragm

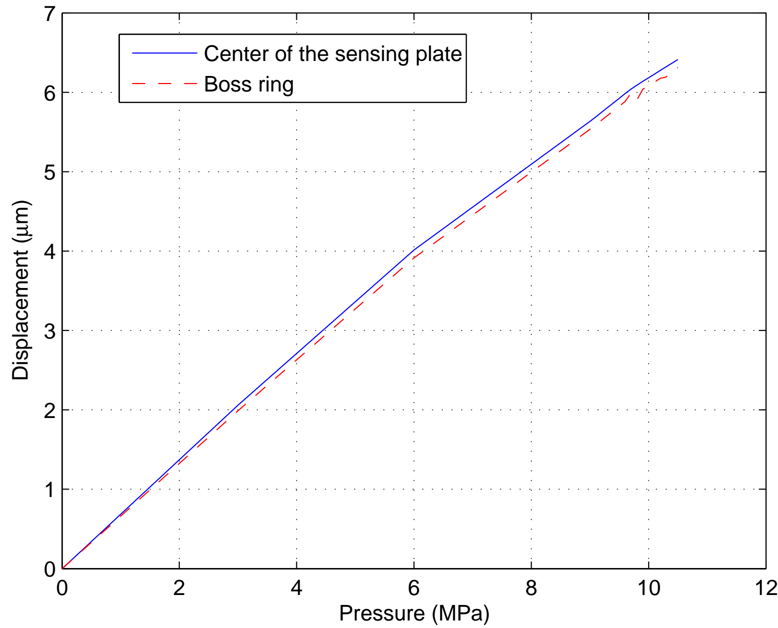

Figure 2.5. Deflection-Pressure curve of boss ring on the sensing diaphragm

and the device will fail. Therefore, accurate stress analysis of the plate deformation is very important to ensure safe design. Figure. 2.4 shows the distribution of Von-Mises stress in the deformed sensing diaphragm. Von-Mises stress is a generalized quantity that is proportional to the strain energy density caused by the change of diaphragm shape at a integrating point. As shown in Figure. 2.4, the maximum

stress is at the center of four edges and the surrounding area surrounding the boss ring, which indicates that these area are most liable to rupture when the applied pressure increase over elastic region of the diaphragm material. The sensors are designed to be in the range where the maximum sensing stress is less than rupture pressure by a safety factor 60% so that the typical fracture strain is 1×10^{-2} [51] [52]. From Figure. 2.4, the largest Von-Mises stress in the deformed diaphragm is $1402MPa$, about 53.9% of the tensile strength of polysilicon ($2600MPa$) indicated in section 2.2.1.

In Figure. 2.5, the dashed line represents the displacement of the boss ring that is attached to the sensing diaphragm. This displacement is determined by the deflection of the sensing diaphragm at the boss ring region. Since the boss ring is located near the center diaphragm, its displacement is close to the center deflection, represented by the solid line in Figure. 2.5. It can be seen that the deflection of the sensing diaphragm changes proportionally with pressure when the pressure is less than about $6.0MPa$. Beyond that point, the change of diaphragm deflection tends to be slower and the phenomena of nonlinearity can be observed in the deflection-pressure curve, where the change of maximum displacement is not so fast as the pressure load. The nonlinearity effect in the high pressure range degrades the sensor performance since it always desirable to maintain a simple linear relationship for engineering applications.

2.2.3 Deflection of the middle diaphragm

The concept of mechanical amplification is to achieve greater displacement in the cantilever middle plate despite of the small deflection in the sensing diaphragm. The middle diaphragm starts to deflect when the boss ring move down and touch it. In the case when two parts come into contact, there are complex load and boundary conditions, resulting from transferring of forces and moments from the boss ring to the middle diaphragm. In this section, to model the deformation of the middle diaphragm correctly, the contact problem is analyzed by using ABAQUS. ABAQUS provides an effective way with good modelling accuracy for contact prob-

lems when there are gradual spatial variations in elastic and inertial properties in the diaphragm.

In the proposed sensor, the most complicated stage of the entire simulation process is when the various surfaces are brought together. The surfaces cannot start in a touching configuration as there are too many redundancies in the contact stresses along the surfaces, and if they are brought together too imprecisely the gaps can chatter between open and closed in successive iterations. Modelling the model characteristics around touch point pressure involves the analysis of multiple rigid surfaces. The rigid surfaces must be smooth, which is easily achieved by using the SMOOTH parameter on the *RIGID SURFACES option in ABAQUS, and the rigid surfaces must also extend beyond the mesh to ensure that nodes do not slide off the end of the surface. The contact analysis in ABAQUS is performed using following steps:

- Before pressure is increased, it is assumed that no contact has yet been established. Without additional constraints on surfaces there is zero stiffness in the vertical direction and a numerical singularity will result. To overcome the problem, at the clamped edges of sensing diaphragm, a set of reference points are chosen, and the positions of these reference points are always fixed when the two parts come into contact.

- The contact surface on the middle diaphragm is defined as “Slave” surface, and the contact surface on the sensing diaphragm is defined as ”Master” surface. Contact condition is defined so that all the points in “Slave” surface will not extrude the “Master” surface. Regarding to reference points, ABAQUS attempts to create the contact equation between two surfaces, and constraints to nodes on the contact elements are applied accordingly.

- The contact equation is is solved iteratively in order to ensure a firm contact condition with no possibility of singularities or chattering.

The deformed shape of the middle diaphragm after contact occurs is shown in Figure. 2.6. It shows that at the diaphragm corners, the displacement reach

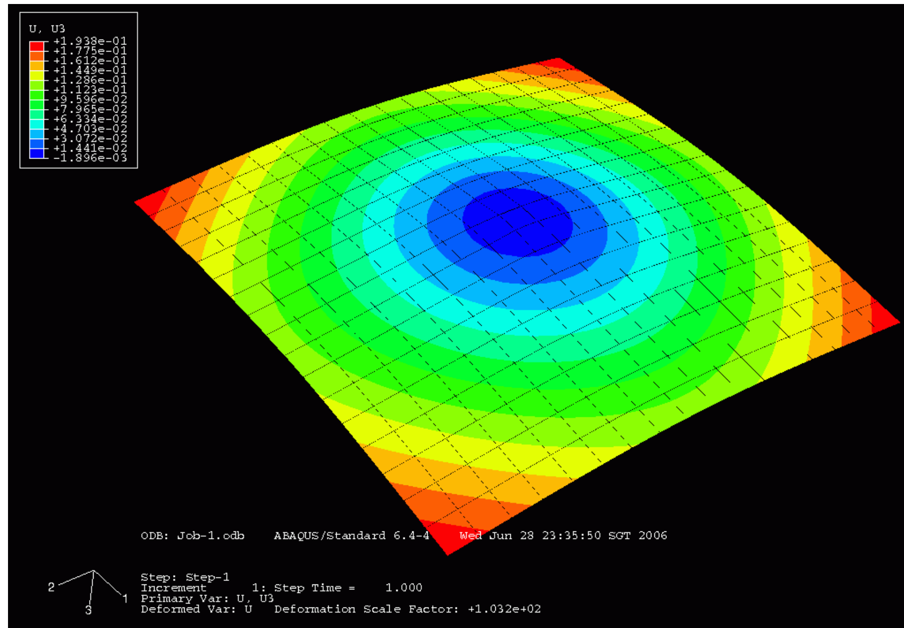

Figure 2.6. The deformation contour of the middle diaphragm at the pressure point $10.8MPa$. $a = 500\mu m, h_{mid} = 1.50\mu m, b = 20.0\mu m, g = 6.0\mu m$

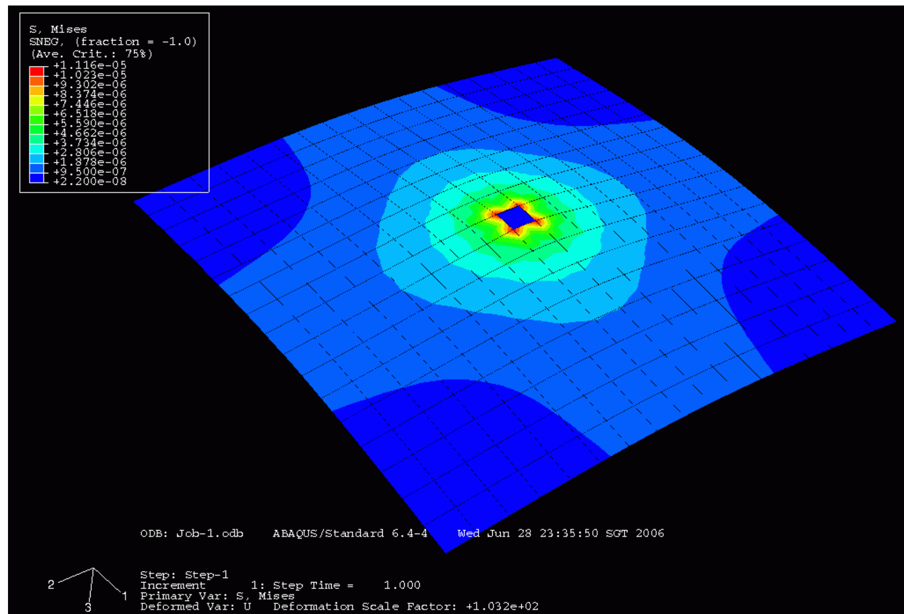

Figure 2.7. Stress distribution in the cantilever middle diaphragm

maximum values of $1.775\mu m$. Figure. 2.7 shows the Von-Mises stress distribution in the deformed diaphragm. Regions where stress are as high as $10.23MPa$ are located near the post, and in the contact region between the boss ring and the

middle diaphragm. However, these stresses are small compared to that of the sensing diaphragm ($1402MPa$). Therefore, it is sufficient to only consider the stress in the sensing diaphragm for fracture analysis.

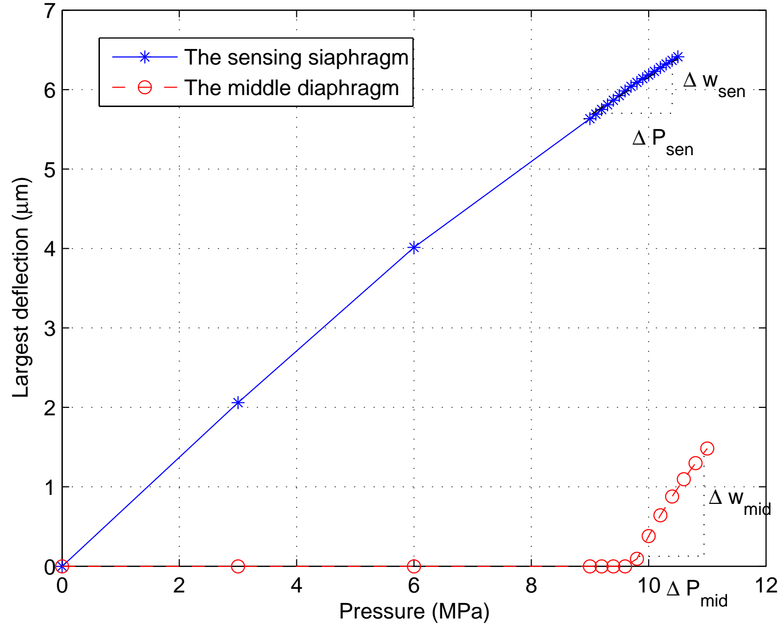

Figure 2.8. Largest deflection in top sensing and middle plates at the pressure point $10.8MPa$.

The largest deflection of the sensing and middle diaphragms are shown in Figure. 2.8. The deflection-pressure curve of the cantilever middle diaphragm remains at zero for the pressure less than $9.8MPa$. The middle diaphragm's deflection increase abruptly after that pressure point. In the small region after $9.8MPa$, the deflection-pressure curves of both diaphragms is regarded as a straight line in order to estimate the device sensitivity. From Figure. 2.8, the slope of the middle diaphragm curve is $\Delta w_{mid}/\Delta P_{mid} = 1.0991\mu m/MPa$, and the slope of the sensing diaphragm curve is $\Delta w_{sen}/\Delta P_{sen} = 0.5172\mu m/MPa$. Therefore, it can be concluded that deflection of the middle plate is a magnified form of the movement in the sensing diaphragm.

2.3 Capacitance calculation using integration method

The proposed sensor utilizes capacitive sensing mechanism to realize pressure measurement. Thus, it is of much importance to calculate the device capacitance in as accurate a manner as possible. In the proposed sensor, the capacitor consists of two electrodes, one on the deformable middle diaphragm, and another on the rigid substrate. The geometric data of the deformed middle diaphragm under various pressure loads is simulated and exported from ABAQUS. Given other descriptions of the capacitor, like relative permittivity of dielectric material, thickness of the insulated layer and initial gap distance between electrodes, it is possible to compute the capacitance for each pressure points. In this way, capacitance pressure relationship can be obtained, enabling the electrical performance of the sensor to be analyzed.

From Figure. 2.1, the undeformed shape of the device is two parallel plates so the nominal capacitances (zero pressure capacitance) can be computed simply by the parallel-plate capacitance equation:

$$C_0 = \frac{\varepsilon_0 \varepsilon_a a^2}{\eta} \tag{2.2}$$

where a is the side length of two electrodes, ε_0 is the permittivity in vacuum, ε_a is dielectric constant of air and η is the initial gap distance between two electrodes.

In the operation of the sensor, the area of electrodes is always unchanged. The change of capacitance is mainly due to the relative movement between two electrodes. This mechanism is inherently nonlinear since the capacitance is inversely proportional to gap distance. Moreover, due to the non-uniform displacement of the middle diaphragm, it is necessary to consider the gap change over the entire plate area. One approach that may be used to estimate the capacitance of the device, is the integration method.

Integration method employs the diaphragm geometry to calculate the capacitance of the micro pressure sensors. The diaphragm geometry is first divided into base elements that can be regarded as very small parallel plate capacitors. Therefore, parallel plate models can be applied to compute the capacitance contribution

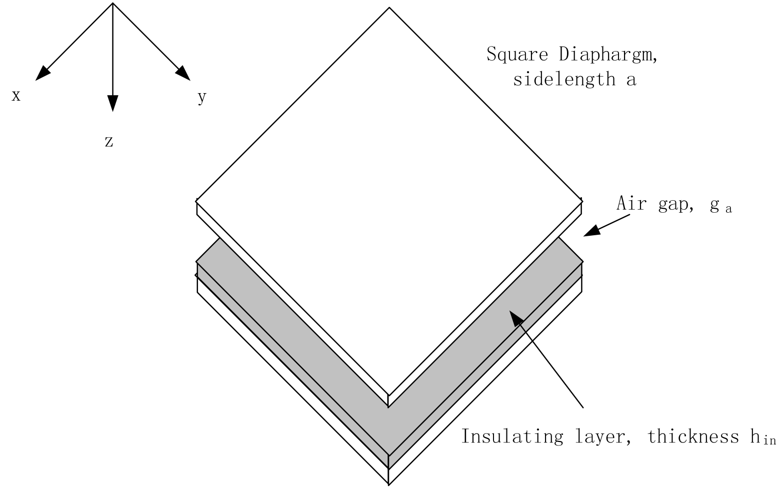

Figure 2.9. Structure of a typical capacitive pressure sensor with an insulating layer

of each base elements.

Figure. 2.9 shows the three dimensional structure of a typical parallel-plate capacitive sensor. It consists of a movable plate, an insulating layer and the substrate. The movable plate is a square silicon diaphragm with side length a. It deforms when a pressure load is applied to the structure. The insulating layer is included to avoid short circuit problems and ensure long term stability of the device. The thickness of insulating layer is h_{in}.

After the geometry file of deformed plate is exported from ABAQUS, capacitance of the sensor shown in Figure. 2.9 can be calculated analytically. The whole capacitor can be regarded as many small square capacitors connected in parallel. If a small capacitor is considered, its vertical z displacement ($dz = w(dx, dy)$) can be regarded as uniform. Hence, the capacitance of this small region is:

$$dC_{air} = \frac{\varepsilon_0 \varepsilon_a dxdy}{g_a - dz} \tag{2.3}$$

where ε_0 is the permittivity in vacuum, and ε_a is dielectric constant of air. The capacitance change of insulating layer remains unchanged:

$$dC_{in} = \frac{\varepsilon_0 \varepsilon_d dxdy}{h_{in}} \tag{2.4}$$

where ε_d is dielectric constant of insulating layer. Since the multi-layer capacitor

can be regarded as two capacitors connected in series, the capacitance between top and bottom plates is:

$$dC = \frac{dC_{air} dC_{in}}{dC_{air} + dC_{in}} = \frac{\frac{\varepsilon_0 \varepsilon_a dxdy}{g_a - dz} \frac{\varepsilon_0 \varepsilon_d dxdy}{h_{in}}}{\frac{\varepsilon_0 \varepsilon_a dxdy}{g_a - dz} + \frac{\varepsilon_0 \varepsilon_d dxdy}{h_{in}}} = \frac{\varepsilon_0 \varepsilon_a \varepsilon_d}{\varepsilon_a h_{in} + \varepsilon_d (g_a - dz)} dxdy \tag{2.5}$$

The capacitance of the whole structure can be obtained by integration:

$$C = \int\int \frac{\varepsilon_0 \varepsilon_a \varepsilon_d}{\varepsilon_a h_{in} + \varepsilon_d (g_a - dz)} dxdy = \int\int \frac{\varepsilon_0 \varepsilon_a \varepsilon_d}{\varepsilon_a h_{in} + \varepsilon_d (g_a - w(dx, dy))} dxdy \tag{2.6}$$

$w(dx, dy)$— the deflection of diaphragm at node(dx,dy).

The integration method is an approximate approach that predict the capacitance based on a 3-D geometric data. This may be the reason that the GUI method gives a larger capacitance result than the integration method does when deformed structure is considered.

Besides the integration method, there are some other capacitance calculation methods, such as GUI simulation methods, etc..

2.4 Mechanical and electrical characteristics of the Sensor

With the help of Finite Element Software ABAQUS and the capacitance computation method, both mechanical and electrical characteristics of cantilever pressure sensors can be obtained. In this section, several sensor models have been analyzed using above methods.

2.4.1 Capacitance-Pressure characteristics

From the deflection data shown in Figure. 2.8, the capacitance is calculated. The Capacitance-Pressure characteristic of the capacitive pressure sensor is shown in Figure. 2.10. When the applied pressure is less than touch point pressure of $9.8MPa$, the middle diaphragm does not deflect so that capacitance between the middle electrode and substrate remains unchanged. The Capacitance-Pressure

Curve beyond $9.8MPa$ can be represented by the following polynomial:

$$C = S_0 + S_1 * P + S_2 * P^2 + ... \quad (2.7)$$

Where C is the capacitance of the device, P is the applied pressure load, and S_0, S_1, and S_2 are polynomial coefficients. The Capacitance-Pressure curve from 10.0 to $11.0MPa$ can be regarded as a straight line approximately, which indicates that capacitance change proportionally to applied pressure. Thus this region can be deemed as linear region and used as the working range of the sensor. In this region, all the high order polynomial terms may be ignored, i.e. $S_N = 0, N > 2$. The sensitivity of the pressure sensor can be regarded as coefficient S_1, and the slope of the best straight line that is fitted to the C-P data in the least square sense. Figure. 2.10 shows the capacitance change curve when the sensing diaphragm and the substrate are used as the two electrodes of a parallel plate capacitor. Due to the small deflection in the sensing diaphragm, and the large gap distance between these two electrodes, the slope of C-P curve is very small. Hence the sensitivity is only 0.0243 fF/kPa for pressures ranging from 9.8 to $11.2MPa$. From Figure. 2.10, a sensitivity of 0.5725 fF/kPa at the range from 10.0 to $10.8MPa$ can achieved in the cantilever middle diaphragm curve. About 2070% improvement in the sensitivity can be observed when the cantilever middle diaphragm is used to magnify the deformation.

2.4.2 Impact of fringe capacitance on C-P characteristics

Typically, the capacitance of the pressure sensor is estimated as a sum of two components, the parallel plate capacitance due to overlap area, and the capacitance formed by the fringing electric fields outside the overlap area. In section 2.3, when calculating the capacitance between parallel plate electrodes, the integration method only consider the overlap capacitance between plate electrodes. The fringe capacitance also need to be considered so as to understand the characteristics of the sensor device in a more comprehensive way.

The capacitance due to the fringing field at the ends of the electrodes can be computed based on the model given in [53]. For a parallel plate capacitor, the

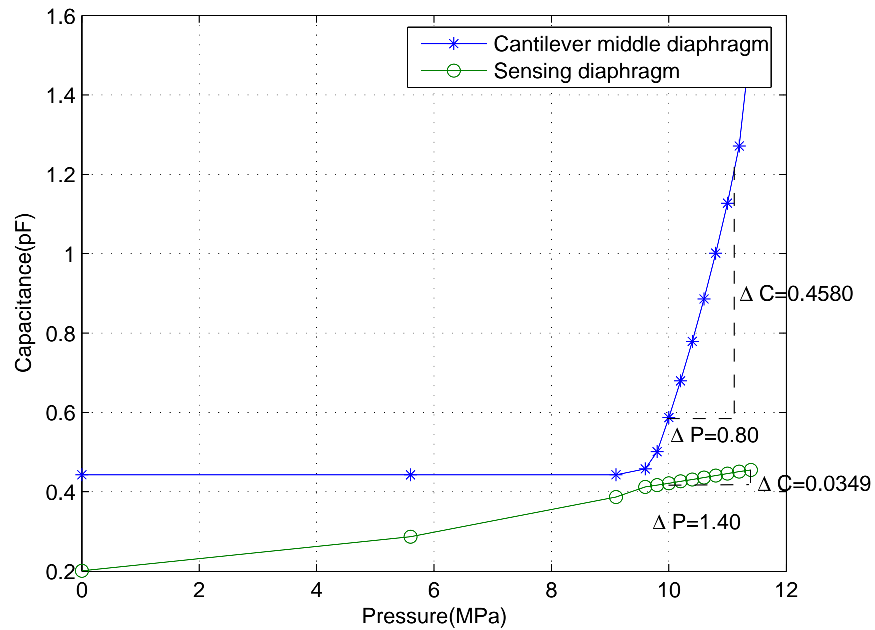

Figure 2.10. Capacitance-Pressure characteristics of the proposed sensor. $a = 500\mu m$, $h_{sen} = 20\mu m$, $h_{mid} = 1.50\mu m$, $g = 6.0\mu m$, $d = 75\mu m$, $p = 50\mu m$

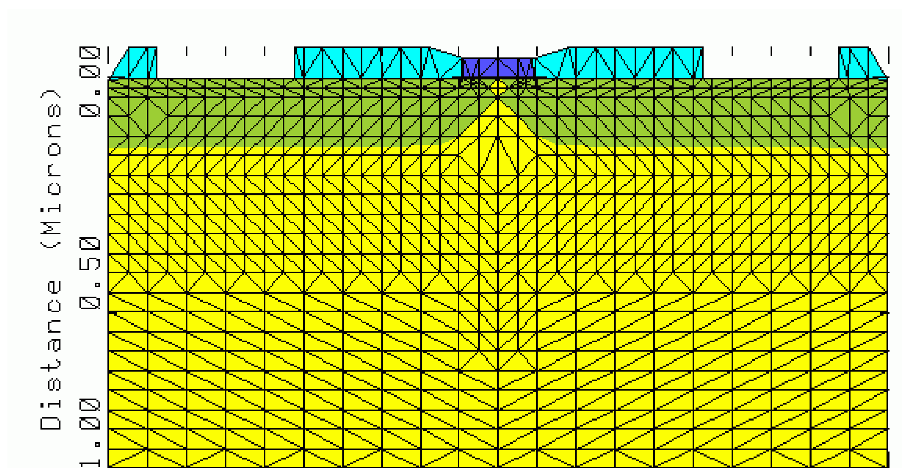

Figure 2.11. A model of parallel plate capacitor constructed in MEDICI.

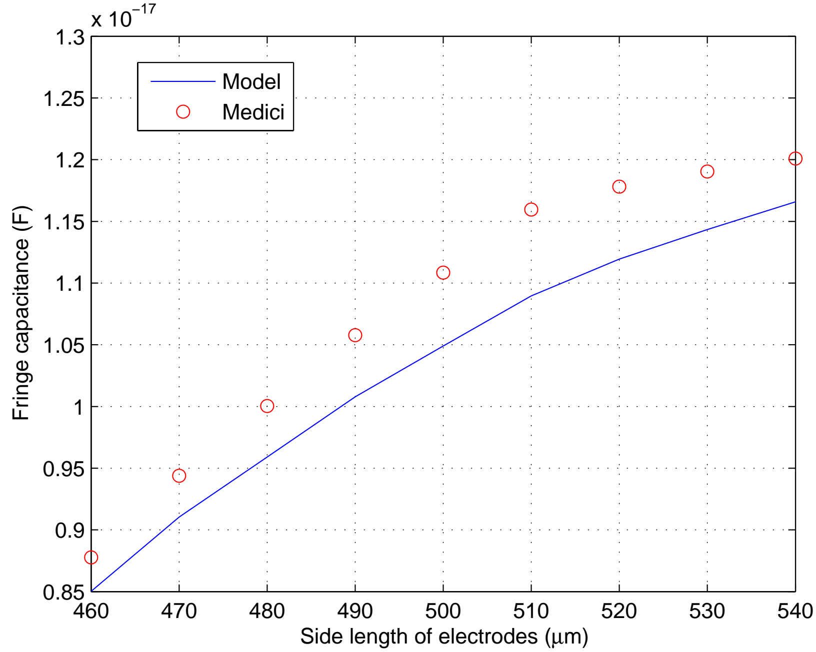

Figure 2.12. Fringe capacitance variations with electrode size from 460 to 540μm

fringe capacitance per edge is given by Equation (2.8):

$$\Delta C_f = \frac{\varepsilon_0 \varepsilon_a a}{2\pi} \ln \frac{\pi a}{\eta} \tag{2.8}$$

where η is the distance between the electrodes, ε_a is the permittivity of space material (air) and a is the length and width of the electrode. While Equation (2.8) provide a convenient means to estimate fringe capacitance, it is only valid if $\eta \ll a$. In the case where η is much larger, or environment surrounding the electrode edges is complex, this approximate equation may not be applicable. Fortunately, several simulation models have been proposed to compute fringe capacitances in MOSFETs [54] and in Nanoscale DGMOS Devices [55]. Besides these specified fringe capacitance model, a powerful device simulation program, MEDICI can be used to simulate the fringe effect of capacitors [56]. Figure. 2.11 shows a parallel capacitor model after meshing in MEDICI. The gap distance between electrodes is 2.0μm and the size of electrodes is varied from 460 to 540μm.

In Figure. 2.12, the fringe capacitances simulated by MEDICI are compared to the results calculated by Equation. (2.8). There are a difference of $0.5 \times 10^{-18} F$, or 4.76% percentage error between the results of MEDICI and Equation (2.8).

Moreover, it can also be seen that the fringe capacitance ($1.05 \times 10^{-17}F$) is much smaller than the capacitance ($0.6 \times 10^{-12}F$) formed by overlap electrodes. In the proposed sensor, the magnitude of fringe effect only accounts for 0.0018 % in the total capacitance. Thus, it may possible to ignore it and only consider the parallel plate capacitance.

2.4.3 Temperature dependance

The sensing diaphragm of the pressure sensors are always exposed to ambient conditions with various temperatures. The thermal differences between the sensing diaphragm and the middle diaphragm may affect the sensor performance. The pressure sensor output usually drift slightly due to temperature change. Since the proposed sensors need to performance high sensitive measurement in a small range, even a small deviation may not be acceptable. Thus, it will make sense to estimate the extent of the temperature effects.

The thermal analysis of the device can be performed in ABAQUS, by applying different temperature fields in both diaphragms. The temperature fields are defined as thermal loads that distribute uniformly across the diaphragms. The magnitude of temperature field in the middle diaphragm is set to $T_{mid} = 20°C$, and it kept unchanged in the analysis. The magnitude of sensing diaphragm temperature T_{sen} is ramped from 20 to $100°C$. Figure. 2.13 shows the distribution of the temperature loads when $T_{sen} = 40°C$.

The effect of temperature on the sensor performance is shown in Figure. 2.14. It can been seen that Capacitance-Pressure curve has a small shift upwards when temperature increase. High temperature has an effect than soften the diaphragm rigidness, therefore the sensing diaphragm are more liable to deform. This effect leads to a earlier touch point pressure and higher capacitance values. For the proposed sensor that utilizes capacitive sensing, the small temperature dependance is very attractive. Furthermore, Figure. 2.14 also shows that the sensitivity (slope) characteristics is independent of the temperature.

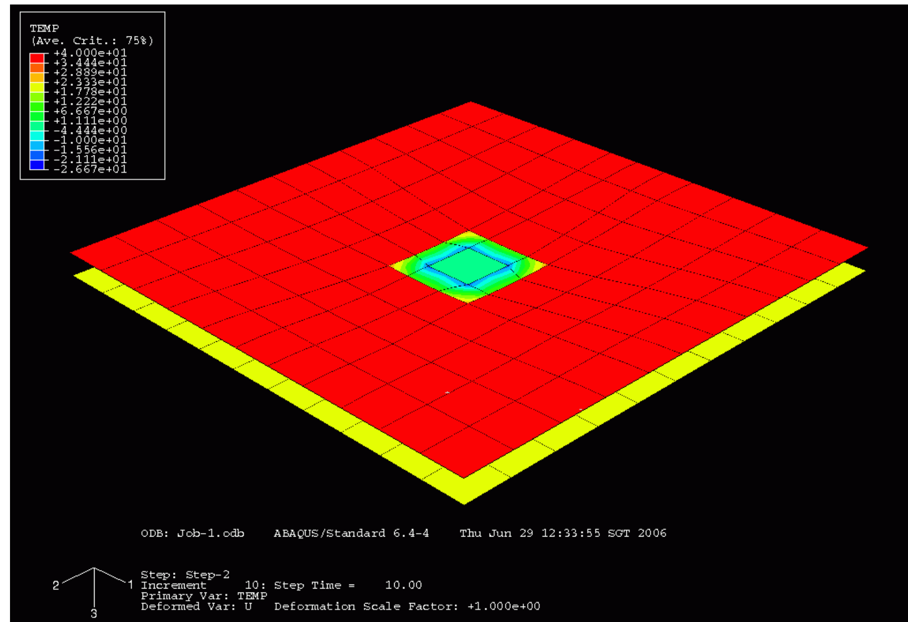

Figure 2.13. Temperature distribution in the sensor structure, $T_{sen} = 40°C$, $T_{mid} = 20°C$

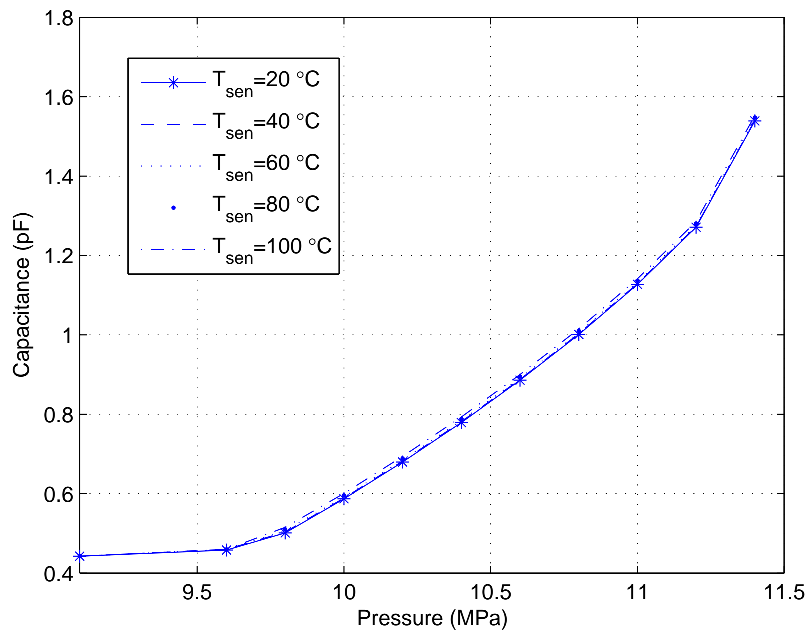

Figure 2.14. Capacitance-Pressure characteristics

2.4.4 Sensitivity comparison

The proposed pressure sensor is designed to detect small pressure fluctuation in a high pressure ambient. Hence, it would be ideal if a sensitivity is comparable to a normal parallel capacitive pressure sensors, when the touch point pressure is reached. Typically, a capacitive pressure sensors consists of two parallel electrodes, a rigid substrate and a deformable electrode with clamped edges. The parallel plate sensor always works in a manner that the two electrodes do not touch each other. To withstand the pressure load around $10MPa$, a sensing diaphragm as thick as $20\mu m$ is required. Such a sensor would have a sensitivity of 0.0391 fF/kPa which is not desirable.

For the parallel plate capacitive pressure sensor working under the normal pressure conditions, such as $0 \sim 50kPa$, the thickness of the sensing diaphragm can be less than $5\mu m$ [21]. Table. 2.3 compares the sensitivity of the proposed sensor with two parallel plate capacitors. The analysis shows that the introduction of a cantilever middle diaphragm resulted in a 1364% improvement in sensitivity, when compared with a parallel plate capacitive pressure sensor whose sensing diaphragm is $20.0\mu m$ thick. The sensitivity of the proposed sensor is also comparable with the sensor with a $5\mu m$ diaphragm thickness.

Type	Sensing diaphragm thickness (μm)	Sensitivity (fF/kPa)
Parallel plates sensor	$20.0\mu m$	0.0391
Parallel Plates sensor	$5.0\mu m$	0.242
Proposed sensor	$20.0\mu m$	0.5725

Table 2.2. Sensitivity comparison between different sensors, electrode length $a = 500\mu m$, electrode gap $\eta = 2.0\mu m$

2.5 Cantilever Middle Plate Sensors: Model 2

The deformation of a sensing diaphragm is magnified after it touches a cantilever middle diaphragm. The enlarged deformation in the middle diaphragm can provide

a great improvement in sensitivity. The sensor as shown in Figure. 2.1 can be constructed by using surface micromachining technology. However, if both the sensing and middle films are formed on the front side of a wafer, two sacrificial layers need to be removed during the micromachining process. As a result, it would be harder to control the property and dimension of the thin films. Therefore, an alternative approach that share the same magnification idea is proposed. This new structure utilizes both bulk and surface micromachining technologies, and needs only one sacrificial layer. The thickness and dimension of the sensing diaphragm can be controlled by back side etching.

The alternative model also has the similar structure as the first model, including two movable diaphragm and a solid substrate, as shown in Figure. 2.15. The cantilever middle plate and the rigid substrate form the two electrodes of the capacitor. When the sensing plate deforms due to the applied pressure, the middle plate first move close to the substrate which leads to an increase in the capacitance. However, at the touch point, where the middle plate starts to contact the rigid boss ring, the boss ring exerts a force that cause the thin middle plate to deflect in the opposite way. Within this pressure range, the capacitance decrease as the deflection in the middle diaphragm reduces the gap between the electrodes.

In the subsequent part, a sensor model with following structural dimension is studied:

- Initial gap height $g = 6.0\mu m$;
- Sensing plate thickness $h_{sen} = 20\mu m$;
- Middle plate thickness $h_{mid} = 1.50\mu m$;
- Side length of both diaphragms $a = 500\mu m$;
- Half length of the post $b = 50\mu m$;
- Half length of the boss ring $d = 75\mu m$.

The Capacitance-Pressure characteristics of the model is shown in Figure 2.16. The deformation of sensing and middle diaphragm is simulated in ABAQUS by

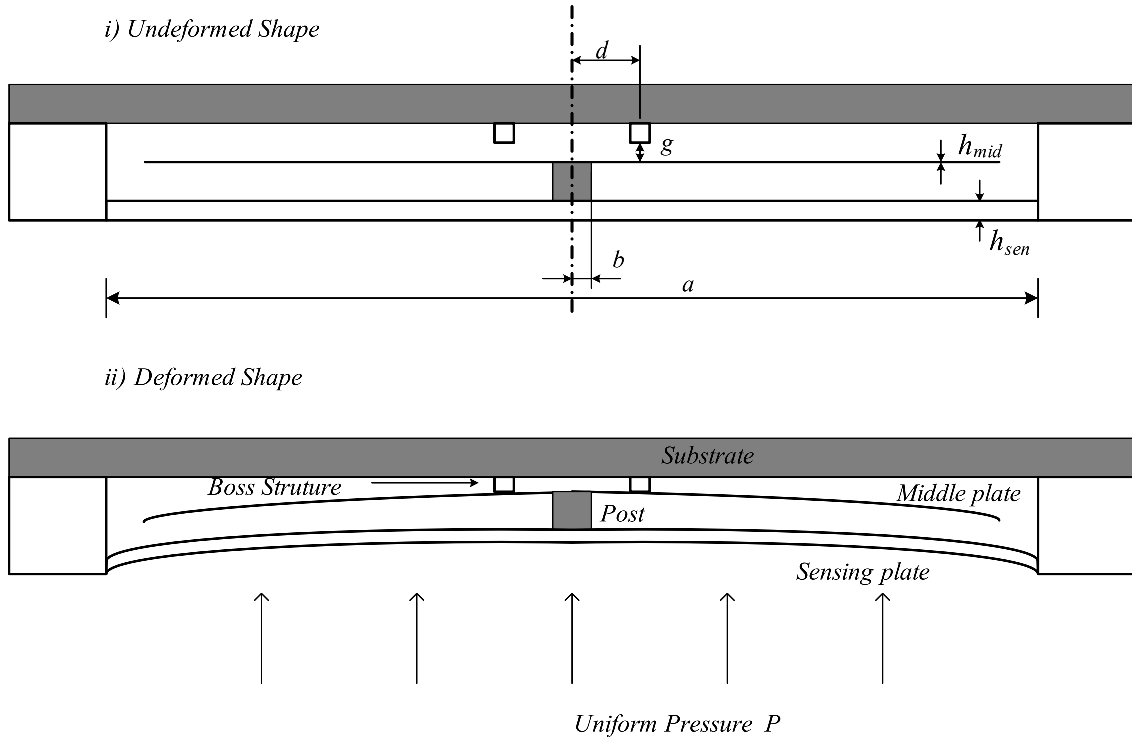

Figure 2.15. The three plates capacitive pressure sensor

constructing a new structure model. The material of sensing diaphragm is single crystal silicon, which has a Young's Modulus of $130GPa$, and a poisson's ratio of 0.2783. It is assumed that the middle diaphragm is formed by thin film technology so the material is polysilicon, which has a Young's Modulus of 165 GPa, and a poisson's ratio of 0.22.

Integration method is employed to calculate the capacitance from the geometry data of the deformed structure model. Although the Capacitance-Pressure characteristics is different to that in Figure 2.10, the mechanism of displacement magnification in the cantilever middle plate are similar. There are two regions in the C-P curve, namely the region before touch occurs and the region after touch point, as shown in Figure 2.16. The capacitance sensitivities between the middle diaphragm and substrate for two models are compared in Table. 2.3. The sensitivity of model 2 is $0.5037fF/kPa$ when applied pressure exceeds the touch point pressure, which is comparable to $0.5725fF/kPa$, the sensitivity of model 1 when the cantilever middle plate is forced to deflect.

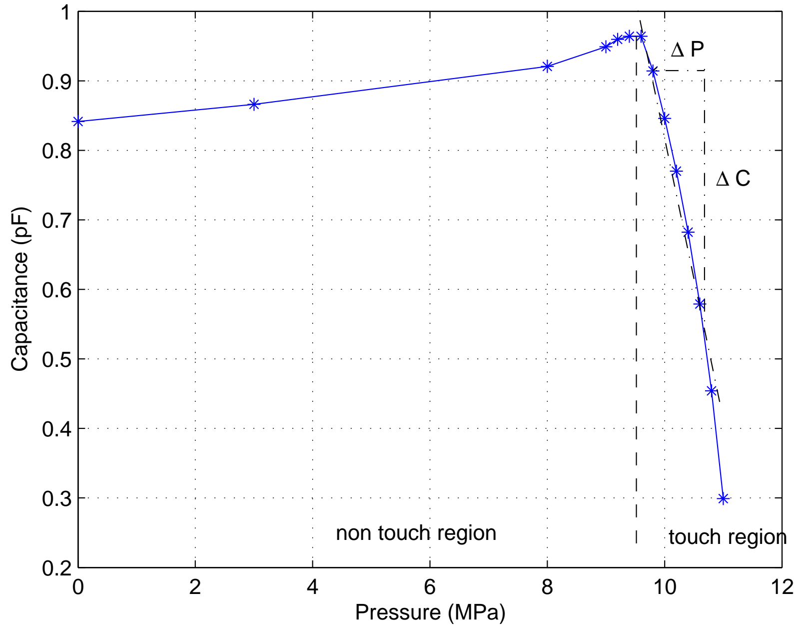

Figure 2.16. Capacitance-Pressure Characteristics of Model 2, $\eta = 1.0\mu m$, $d = 75\mu m$, $b = 20\mu m$

Model	Type	Sensitivity (fF/kPa)
1	Before touch point	0.000
	After touch point	0.5725
2	Before touch point	0.0123
	After touch point	0.5037

Table 2.3. Capacitance sensitivity between the middle diaphragm and the substrate, electrode length $a = 500\mu m$, electrode gap $\eta = 1.0\mu m$

It may be concluded that model 2 has similar characteristics as model 1, except for the different slope directions of C-P curves after the touch point pressure. Model 2 only deal with one sacrificial layer, so that the property of the middle diaphragm will be more easy to control. Moreover, it is very hard to form a thick sensing diaphragm by using deposition method, as discussed in Model 1. With the combination of bulk micromachining process, the thick diaphragm of Model 2 can be obtained by silicon etching process, in which the good film property can be

achieved. Therefore, Model 2 is selected for further analysis and fabrication.

2.6 Conclusions

In this chapter, novel capacitive pressure sensors with two movable diaphragms are proposed. The main application of the sensors is to detect small variations upon a large constant pressure ambient. FEM software ABAQUS is employed to analyze the diaphragm deflection and sensor capacitance are calculated based on the geometric data of deformed diaphragms. The simulation results shows that the proposed sensor with cantilever middle plate has a promising Capacitance-Pressure characteristics after the touch point. Besides the ability to sustain large pressure, it has a sensitivity comparable to normal parallel plate capacitive pressure sensors working in low pressure environment. Another structure model of the same amplification idea is also proposed, the capacitance changes inverse proportionally to the pressure in the touch period.

Chapter 3

Geometric Analysis and Design

The novel capacitive pressure device with two deformable diaphragms has been proposed in Chapter 2. Simulation results demonstrate that the proposed device successfully provided better sensitivity to small pressure fluctuations than conventional parallel plate pressure sensors.

For conventional silicon-based sensors, the design and simulation of such devices have been presented by several papers [42][38]. However, compared to conventional parallel plate capacitive pressure sensors, the proposed sensor has more structural parameters, including diaphragm sizes and thickness, boss ring size, post size, and gap height, etc. Varying each geometric parameter may affect the sensor performance. The task of selecting the various structural parameters is, therefore, more complex. Several criteria needs to be considered during the process of designing the sensor structure. Firstly, the materials of the diaphragms and mechanical stability are considered to allow sufficient fracture tolerance. Touch point pressure, where the capacitance-pressure curve transforms, are also used to select design sets. The pressure sensitivity, or the amount of signal output, can be optimized to achieve maximum value.

This chapter aims at using ABAQUS as a platform to understand the relationship between the structural parameters and the performance of the proposed sensor so as to provide comprehensive information to aid the design process. First, a brief introduction of device fabrication is presented and the design constraints imposed

by fabrication technology and mechanical properties of the structural material are described. Simulation results from ABAQUS are used to give the relationship between the structural parameters and the sensor characteristics. Then, a design method based on graphical analysis is described to find the proper sensor parameters.

3.1 Design constraints imposed by fabrication technology

The proposed capacitive pressure sensor with two deformable diaphragms utilize MEMS fabrication techniques such as bulk micromaching and surface micromaching. As shown in Figure. 2.15, the two deformable diaphragms in conjunction with the rigid substrate form the transducing element of the micro pressure sensor. Combination of surface and bulk micromachining may be used to allow the fabrication and bonding of the free-standing middle diaphragm with the substrate. After the bonding, a backside etching is used to pattern the sensing diaphragm.

The analysis in this chapter will be performed based on this fabrication process. The design of the pressure sensor is intimately connected with the processing and materials. Thus the constraints due to processing are to be taken into consideration.

3.1.1 Materials

The structure materials commonly used in MEMS fabrication process are polysilicion and silicon crystal. The cantilever element in Figure. 2.15 can be fabricated on a SOI (Silicon-On-Insulator) wafer from a deposited thin film of polysilicon after release etching away a silicon oxide layer underneath. The unique feature of SOI wafers is that they have a buried silicon oxide layer extending across the entire silicon wafer, just below a device layer and above a handle layer [57][58][59]. The silicon handle layer underneath can be stop etched to the buried oxide. Due to this feature, SOI wafers are selected, instead of normal silicon wafers, in order

to accurately control the diaphragm thickness. The device is then completed by bonding a patterned pyrex wafer with the SOI wafer.

Therefore, the silicon device layer of SOI wafers is used to form the sensing diaphragm on which the high pressure is applied. Mechanical properties of single crystal silicon are discussed in section 2.2.1. The proposed micro capacitive pressure sensors are designed to work in a high pressure environment, which resulting in high stresses in the deformed sensing diaphragm. In this aspect, silicon is a desirable material for sensing diaphragms since it has a large elastic range, high yield points in compression and tension, and high fracture limits.

The role of cantilever middle plate is to magnify the deformation of the sensing plate. Surface micromachining technology are utilized to construct the cantilever structure. Typically, the plates with free standing edges requires materials with stable, uniform and low stresses mechanical properties. Therefore, polysilicon is a particularly good candidate for the structure material of the cantilever middle plate. Mechanical properties of polysilicon are discussed in section 2.2.1.

When polysilicon is used as the structural layer, surface micromachining technology normally employs silicon dioxide (SiO_2) as the sacrificial material, which will be removed during release etching process to realize some space parts. Polysilicon, as well as silicon dioxide, form a nearly ideal pair for fabrication of the free-standing plate. The cavity etchant, concentrated hydrofluoric acid (HF) has nearly infinite etch selectivity, readily removing the sacrificial space material, silicon dioxide, even in very small geometries ($10\mu m$). For a processing standpoint, polysilicon is patternable and compatible with bipolar and MOS fabrication techniques and has a well-matched thermal expansion coefficient with silicon substrates.

3.1.2 Diaphragm Dimensions

Diaphragm dimensions need to be chosen to provide the maximum pressure sensitivity while staying within process and material constraints. Selecting plate dimensions properly are central to the design of the micro pressure sensor. In the case of a square sensing plate, the dimensions that need to be selected are the

side length and the thickness. In MEMS fabrication, the thickness of each layer is often dictated by wafer thickness and fabrication processes. Hence, unlike the side length, the thickness of the deformable diaphragms cannot be arbitrary selected. Since the proposed device is fabricated on an SOI wafer, the thickness of the sensing diaphragm depends on the available thickness of standard SOI wafers [60][59]. Standard specifications of SOI wafers are shown in Table 3.1.

Specifications	Data
Wafer diameter	4, 5, 6 and 8 inches
Si device Layer thickness	3, 4, 5 ...to 20 μm
Buried oxide Layer thickness	0.0500 to 10 $\mu m \pm 5\%$
Si Handle Layer thickness	300 to 725 $\mu m \pm 15\mu m$
Device layer orientation	$< 100 >, < 111 >$

Table 3.1. Specifications of standard SOI wafers used in IC industry

Since the thickness of the cantilever middle diaphragm is determined by the deposition of a thin polysilicon film, the diaphragm thickness is also generally limited. Although it would be possible to create several thicknesses of diaphragms by repeated deposition and patterning steps, this comes at the expense of more fabrication complexity and overall cost. Moreover, depositing several layers to increase diaphragm thickness may also lead to inferior diaphragm properties including larger internal stress, surface defects and diaphragm warpage. Thus, according to the rule of standard fabrication process [61], the thickness of the cantilever middle diaphragm thickness is fixed in this study as $h_{mid} = 1.5\mu m$. The size of the middle diaphragm can also be changed, and larger diaphragms normally leads to larger nominal capacitance.

3.1.3 Gap Heights

Anodic bonding process is used to bind a pyrex substrate with a SOI wafer which contains a cantilever middle diaphragm. There is an initial gap height (g), or a vertical distance, between the boss ring on the pyrex substrate and the middle

diaphragm. The fabrication of capacitive sensing device by using anodic bonding technology may limit the attainable gap height to no less than 2.0μm [62]. The internal chamber of the proposed sensor shown in Figure. 2.15 is formed by etching pyrex wafer, which normally a 15μm etching depth can be achieved [63]. Therefore, the maximum gap is around 10μm, when the heights of boss ring and cantilever structure are considered. Within these limitations, the proper selection of the gap results in a sensor device with the desired pressure touch point and working range. This gap height also places a limit on the maximum deflection of the deformable sensing diaphragm.

As the cantilever member on the SOI wafer is formed by surface micromachining process, the initial gap height between the middle plate and SOI wafer substrate is defined by the thickness of the removed sacrificial silicon oxide layer. Smaller gap height results in higher capacitance but smaller working range. Step coverage considerations may also limit the gap height, since materials can pile up around protruding structures, such as the post, making too small gap height unacceptable. Typically, use of thermally grown oxide limits the gap height to a maximum of around 1.5μm. Oxide layer formed by plasma-enhanced chemical vapor deposition (PECVD) process can achieve gap height as high as 2.5μm [61]. The limitation of both gap heights are summarized in Table 3.2.

Gap height	Min	Max
between boss ring and the middle diaphragm, g	2.0μm [62]	10μm
between the middle diaphragm and substrate, η	0.05μm [60]	1.5μm (Thermal) 2.5μm (PECVD) [61]

Table 3.2. Limits on gap heights by processing technologies

3.2 Effect of Geometrical Parameters on Sensitivity

In this section, the manner in which the diaphragm dimensions, the gap heights and other geometric parameters will affect performance of the pressure sensor is studied.

As shown in Figure. 2.15, the important geometrical parameters are:

- g - Initial gap height between the boss ring and the middle plate;
- η - Gap height between the middle plate and the substrate;
- h_{sen} - Sensing plate thickness;
- h_{mid} - Middle plate thickness;
- a - Side length of both diaphragms;
- b - Half length of the post;
- d - Half length of the boss ring.

g, η, h_{sen} and h_{mid} are constrained by the fabrication processes, as discussed in preceding section. Those parameters are set to fixed values that is used in the subsequent analysis, as shown in Table. 3.4. The parameters that can be varied, includes the diaphragm size a, the half length of boss ring d and the post half length b.

Fixed parameters	Dimensions (μm)
g	6.0
η	2.0
h_{sen}	20.0
h_{mid}	1.5

Table 3.3. Fixed parameters in geometric analysis

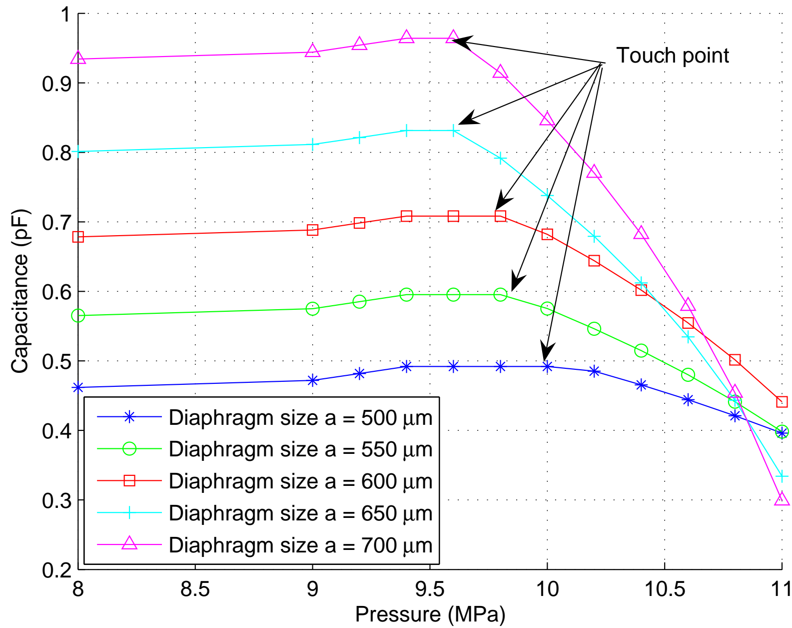

Figure 3.1. Capacitance-Pressure characteristics for different diaphragm sizes, $\eta = 2.0\mu m$, $d = 75\mu m$, $b = 20\mu m$

3.2.1 Diaphragm Size

In the sensor geometric analysis, the sensing diaphragm and the cantilever middle diaphragm are assumed to have the same size, where the side length is denoted as a. Several models with different diaphragm sizes are simulated in ABAQUS, where a is changed from $500\mu m$ to $700\mu m$, in steps of $50\mu m$. The diaphragm thicknesses and the gap height g are as shown in Table 3.4. The half length of the boss ring is set to $d = 75\mu m$ and the half length of the post is $b = 20\mu m$. The capacitance-pressure characteristics of these models are shown in Figure 3.1.

From Figure 3.1, it can be seen that increasing diaphragm size allow the boss ring to contact diaphragms earlier. The touch point in the capacitance-pressure curves, is shifted from $10.0MPa$ to $9.6MPa$, as diaphragm size a increases from $500\mu m$ to $700\mu m$. In the period after touch point pressure, the decrease in capacitance can be regarded as proportional to the pressure change. The range is taken to be the working range of the sensor. Within this range, a straight line is fitted to the capacitance-pressure data points in a least-square sense, and the slope of the

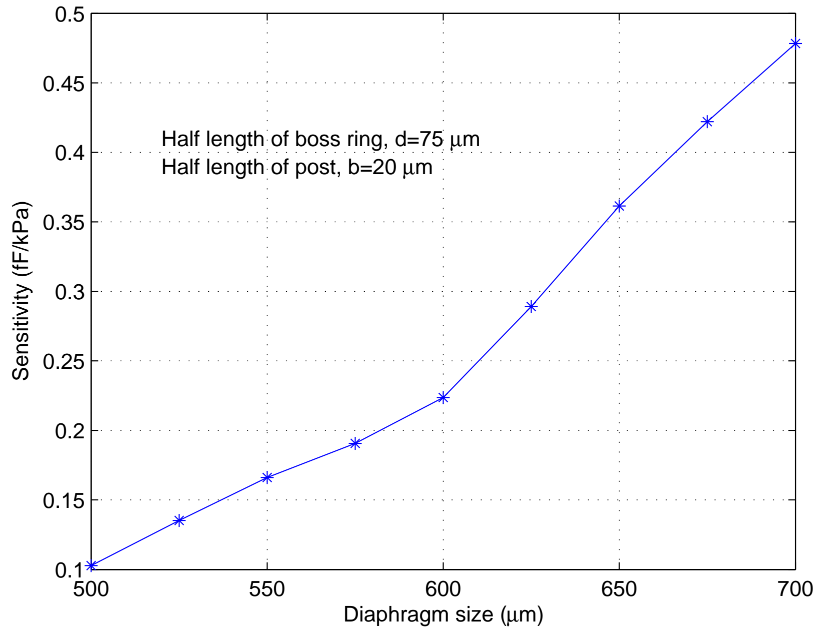

Figure 3.2. Change of sensitivity upon different diaphragm sizes

line is defined as the device sensitivity, as described in section 2.4.1.

Figure 3.1 also shows that the models with large diaphragm size not only results in larger nominal capacitance but also higher sensitivity after the touch point. The detail relationship of device sensitivity vs. diaphragm size is shown in Figure 3.2. Simulation results of some more diaphragm sizes, including $525\mu m$,$575\mu m$, $625\mu m$ and $675\mu m$, are used to provide a smooth and accurate curve. The sensitivity increases almost proportionally to diaphragm size, but there is a change in slope when $a = 600\mu m$. The proportional rate increases from 0.001172 to 0.002658 after this point.

3.2.2 Size of Boss Ring

The half length of the boss ring d is also an important geometrical factor that affects the behavior of the pressure sensor. In this study, different sensor models are simulated by varying d from 35 to 75 μm in steps of $10\mu m$, while fixing the diaphragm size at $a = 500\mu m$ and the half length of the post at $b = 20\mu m$.

Figure 3.3 shows capacitance-pressure characteristics after changing boss ring

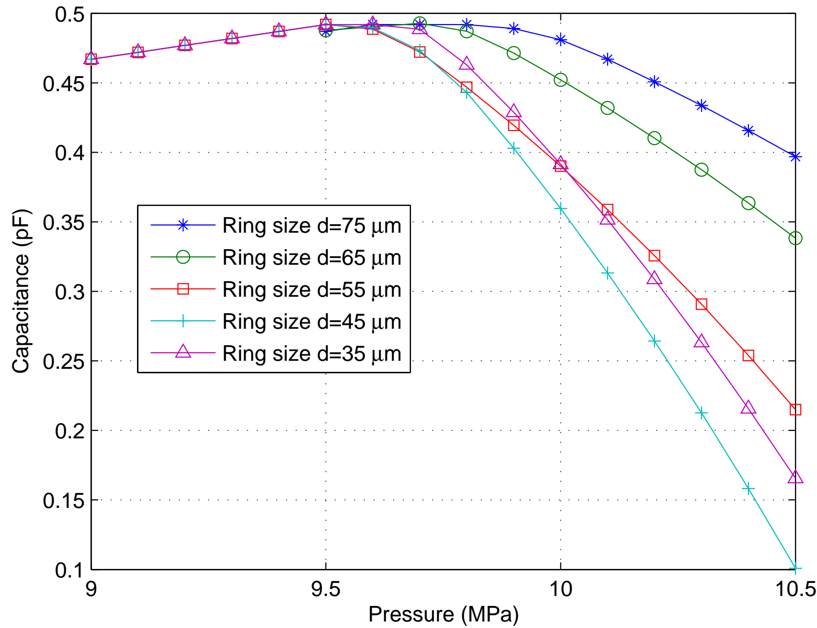

Figure 3.3. Capacitance-Pressure characteristics for different ring sizes, $\eta = 2.0\mu m$, $a = 500\mu m$, $b = 20\mu m$

size. It can be concluded that variations in boss ring size has little effect on the sensor performances before the touch point. That is due to the fact that the boss ring does not touch the cantilever middle plate before touch point pressure. However, it also shows after the touch point, a properly chosen boss ring size may give rise to the device sensitivity.

The relationship between the boss ring size and the sensitivity is more accurately represented in Figure. 3.4. If boss ring size is too small, some part of it may come into contact with the middle diaphragm at the region of post. In the worst case that all the contacts are happened within the post region, the middle diaphragm does not even deflect and consequently no capacitance change is detected. Therefore the deflection of middle plate will decrease, and leads to a small sensitivity. On the other hand, a large ring size means that it is far from the center of sensing diaphragms. Since the diaphragm deflection is largest at the center, the movement of ring size under the same pressure load is diminished, thereby reducing the deflection of the cantilever middle plate. Thus, there is an optimal value of

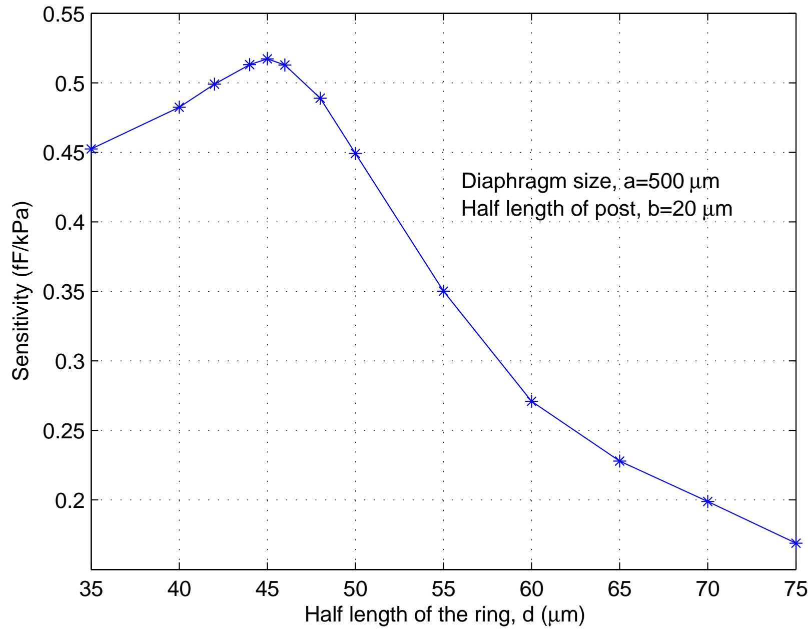

Figure 3.4. The effect of ring size on sensitivity

ring size that can produce the maximum sensitivity with applied pressure. From Figure. 3.4, the peak point value of sensitivity curve is selected, and the achievable maximum sensitivity is 0.5172 fF/kPa, when ring size d is around $45\mu m$.

3.2.3 Change of Post Size

In general, increasing post size will move the clamped center of the middle plate close to the boss ring, and thus leads to a decrease in middle plate deflection which is magnified by the boss ring. Figure. 3.5 shows capacitance-pressure characteristics curves for different post sizes and the changes in these curves only occur after the touch point pressure ($9.6MPa$).

It can also be seen from Figure. 3.6 that the sensitivity monotonously decreases for larger post size b. The relationship curve between sensitivity and post size b is non-linear. If post size b is raised, or the post is close to the boss ring, the slope of relationship curve tends to be smaller.

Although it is true that selecting a small post size can achieve a high sensitivity, it must be noted that the small post size are used only when they do not violate

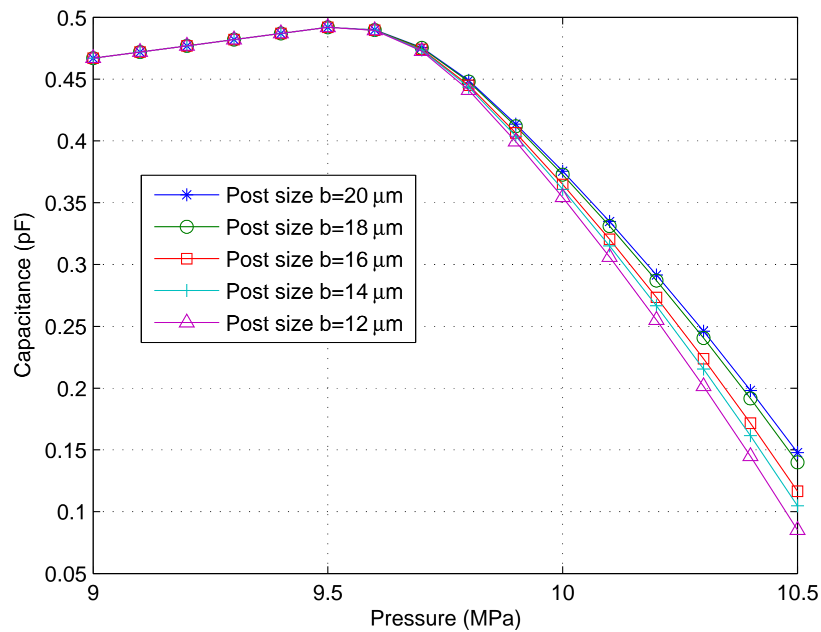

Figure 3.5. Capacitance-Pressure characteristics for different post size, $a = 500\mu m$, $d = 50\mu m$, $\eta = 2.0\mu m$

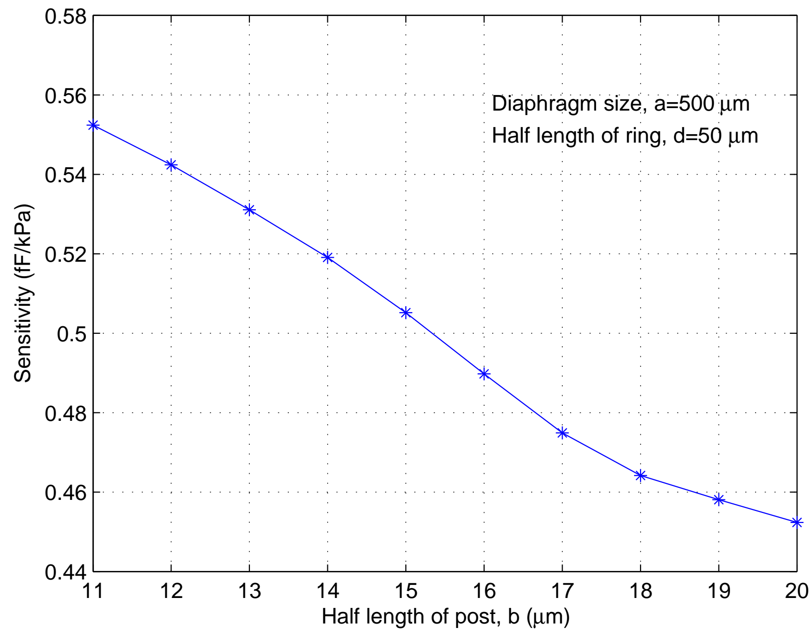

Figure 3.6. Effect of changing post size on device sensitivity

the constraints imposed by fabrication techniques and structure stability.

3.2.4 Alignment Error of Boss Ring

In practice, there are always some alignment errors between different layers. For example, the center of the boss ring may not align with the center point of the post supporting the middle plate precisely. This may leads to an unsymmetrical deformation shape of middle plate, therefore changing the capacitance behavior of the sensor.

The influence of errors in boss ring alignment is very similar to that of changing boss ring size. Some part of the boss ring has smaller deflection and touches the middle plate later, thus makes this part of middle plate less pliable to the pressure load. Other part of the boss ring translates larger deflection to the middle plate and in that region, the device become more sensitive. Fig. 3.7 shows that when the misalignment error of ring position increases, the output capacitance has a positive variation. This positive variation increases continuously until it reaches a turning point. After this point, a negative variation in capacitance output occurs.

In this section, effects of changing geometrical parameters on the behavior of the proposed sensor have been studied. The simulation and analysis shed light on sensor characteristics and form a basis for parameter selection. As a result of the complex relationship between the various parameters, matching parameter change and pressure sensitivity is complicated. Therefore, a systematic approach is required to find the desirable geometries so that the sensitivity to pressure change could be more pronounced.

3.3 Sensor design using a graphical approach

The FEA simulations in Chapter 2 and the analysis in section 3.2 can predict the sensor performance and performance changes when the sensor geometry is varied. The understanding of device parameters and the derived curves generated are used as a design tool to arrive at a desired specific performance using a graphical

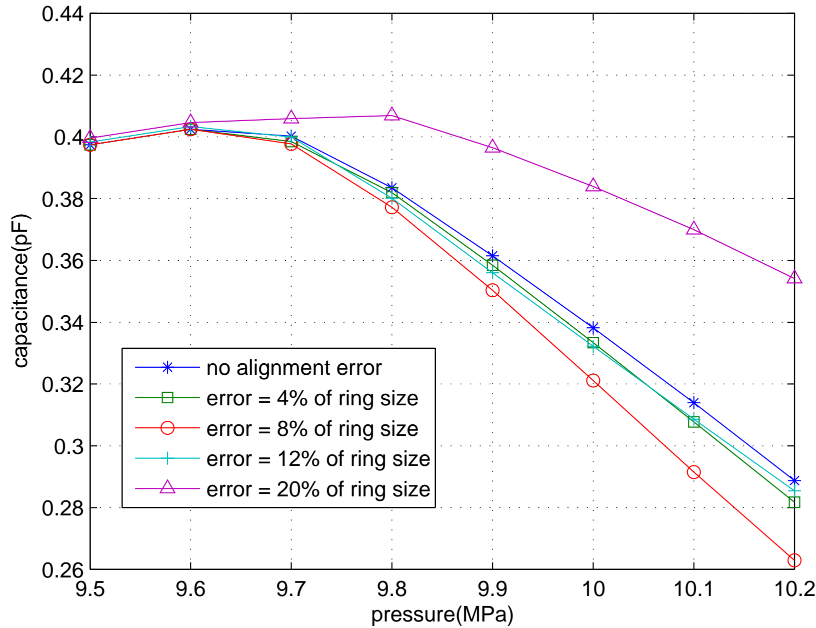

Figure 3.7. Capacitance-Pressure change due to misalignment of boss ring, $a = 500\mu m$, $d = 50\mu m$, $\eta = 2.0\mu m$, $b = 20\mu m$

approach. In a practical design, sensor parameters are to be chosen according to the application requirement.

The two important features involved in the design of the proposed pressure sensor are the touch point pressure and the sensitivity in working ranges. The touch point pressure, where the boss ring of the sensing diaphragm starts to touch the cantilever middle diaphragm, is mainly determined by specifications of the sensing diaphragm and the gap height between diaphragms. Touch point pressure define the starting point of the working range, and capacitance-pressure curve of the sensor shows great difference after touch point pressure. The sensitivity, which is in the form of capacitance change per pressure unit, is the major index of the sensor characteristics. The capacitance change can be detected directly or after electrical conversions. In either approach, the sensor must be designed to produce noticeable electrical signals that required to detect small pressure variations.

3.3.1 Design diaphragm size and gap

As discussed in section 3.1, the sensing diaphragm is formed by the silicon device layer of a SOI wafer. Therefore, the diaphragm thickness should comply to the standard SOI specifications listed in Table 3.1. In this section, two important parameters, the diaphragm size a and gap height g, are designed to meet the required sensor specifications. Other geometric parameters are unchanged during this design step, including boss ring size $d = 50\mu m$, post size $b = 12\mu m$.

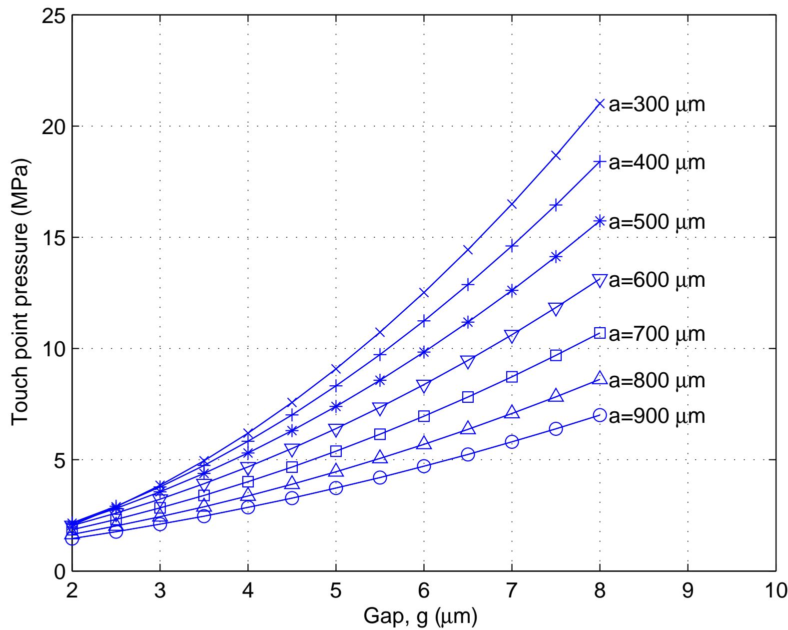

Figure 3.8. Relationship between touch point pressure and the gap for different diaphragm sizes

A series of touch point pressure Pt and gap g characteristics are plotted with different sensing diaphragm sizes a in Figure 3.8. The g vs. Pt curves are obtained from ABAQUS simulation results. With a known touch point pressure Pt, different combinations of g and a can be designed. Although the curves are obtained with diaphragm sizes $h_{sen} = 20\mu m$, similar curve group and design approach can also be applied to different thickness of sensing diaphragms.

Figure 3.9 shows the sensitivity versus gap height (g) for different diaphragm sizes. The relationship curves are plotted according to ABAQUS simulations re-

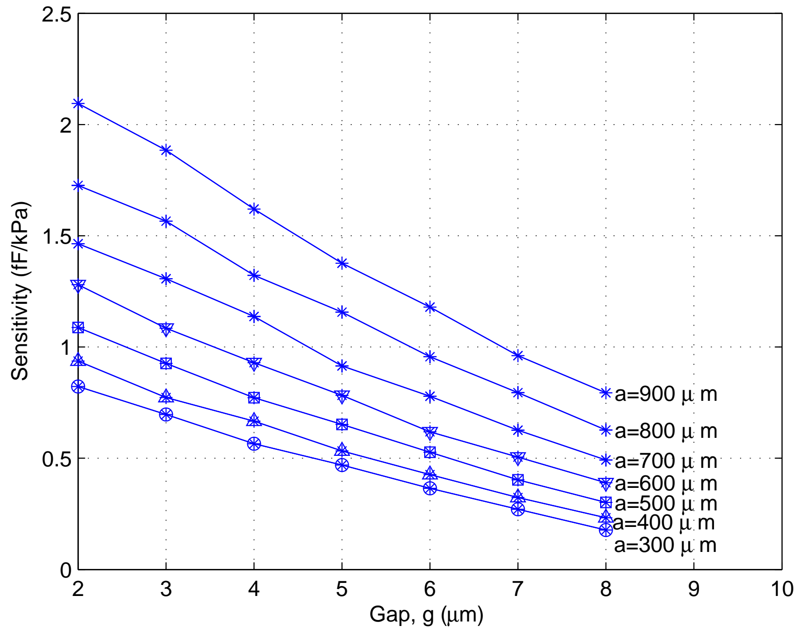

Figure 3.9. Relationship between Sensitivity and the gap for different diaphragm sizes

sults. Desired sensitivity can be designed by virtue of selecting proper diaphragm size a and gap height g from the group of curves.

Since capacitance is proportional to the area of the diaphragm, i.e., a^2, the sensitivity with a smaller diaphragm usually have a smaller sensitivity in their working range. To illustrate the design procedures, a sensor with the following specifications is designed:

- The working range of the sensor is $10.0 \sim 11.0MPa$;
- Sensitivity S larger than $0.5fF/KPa$, which is a achievable specification from Table. 2.3.

In Figure. 3.10, which combines Figure 3.8 and Figure 3.9, the solid lines are the touch point pressure P_t vs. gap g curves and the dot lines are the sensitivity S vs. gap curves. The touch point pressure can be chosen as $P_t = 9.5 - 10.0MPa$ to get a working rage of $10.0 \sim 11.0MPa$. The sensing diaphragm of thickness $h_{sen} = 20\mu m$ is selected. Hence, Figure. 3.10 can be used directly to determine g

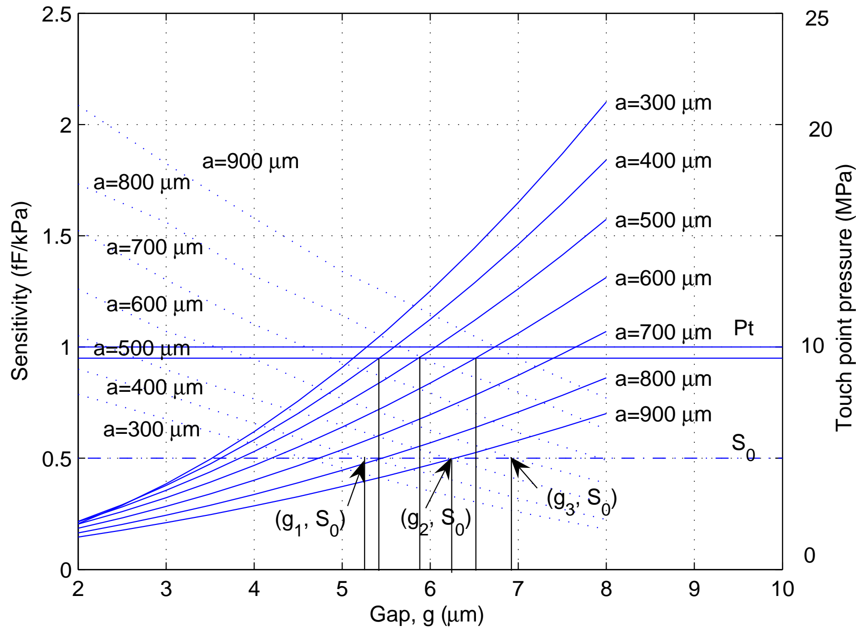

Figure 3.10. Graphics design tool for the pressure sensor

and h in order to meet the specifications listed above.

Combination of the curves P_t vs. g with different diaphragm sizes a, and two horizontal lines $P_t = 9.5MPa$ and $P_t = 10.0MPa$ can be used to define the area to get the touch point of $9.5 \sim 10.0MPa$. A horizontal line $S_0 = 0.5fF/kPa$ is also drawn in Figure. 3.10. In order to meet the requirement of Sensitivity $> 0.5fF/kPa$, the combination of g and a must be selected in the area above the line S_0. The line S_0 has interaction points with dashed curves (Sensitivity vs. g). The interactions are denoted by (g_1, S_0),(g_2, S_0),(g_3, S_0), where g_i represents the gap at certain sensing diaphragm sizes that can give pressure sensitivity of S_0.

The diaphragms with $a = 400\mu m$, $a = 500\mu m$, and $a = 600\mu m$ are taken into consideration. For the case of $a = 500\mu m$, if a sensor has gap $g < 6.20\mu m$, its sensitivity will be larger than 0.5 fF/kPa. On the other hand, its gap must be larger than $5.80\mu m$ in order to get the touch point in $9.5 - 10.0MPa$. Therefore, the gap for this diaphragm can only be with the range of $5.80\mu m < g_2 < 6.20\mu m$. It can be also concluded from Figure. 3.10 that the gap should be in the range of $6.55\mu m < g_3 < 6.90\mu m$ for $a = 600\mu m$. For $a = 400\mu m$, $g_1 < 5.25\mu m$ and

$g_1 > 5.45\mu m$ can not be satisfied together, so there is no proper gap design range in the diaphragm $a = 400\mu m$ that meet the required specifications.

Pt (MPa)	gap (μm)	a (μm)	Graphical design $S_1(kF/MPa)$	FEA $S_2(kF/MPa)$	Error
9.6	5.90	500	0.5592	0.5331	4.896%
9.8	6.00	500	0.5237	0.5037	3.971%
9.6	6.60	600	0.5692	0.5891	3.378%
9.8	6.75	600	0.5492	0.5746	4.420%

Table 3.4. comparison of simulated results, FEA and Graphical design

Table 3.4 lists the results of sensitivity estimated from Figure. 3.10 and ABAQUS data with touch point pressure $10MPa$. The error is defined as $(S_1 - S_2)/S_2 \times 100\%$. For both cases, the error of the estimated results is less than 5.0%. Therefore, the graphical method can be used to design sensor structures.

3.3.2 Determine sizes of boss ring and post

In above design procedure, the size of boss ring d and post size b is kept unchanged at $d = 50\mu m$, $b = 20\mu m$. Since section. 3.2 have clearly shown the effect of d and b on device sensitivity, choosing appropriate d and b values will help to enhance sensitivity.

In Figure. 3.11, the design group of curves is obtained from ABAQUS simulations with diaphragm size $a = 500\mu m$ and gap height $g = 6.0\mu m$. It may be deduced that the maximum sensitivity of $0.7448fF/kPa$ can be found at $d = 42\mu m$ and $b = 12\mu m$. Since post size b does not affect touch point pressure, the touch point pressure can be estimated using the Figure. 3.12 by varying the size of boss ring d. From Figure. 3.12, the touch point is $P_t = 9.53MPa$ at boss ring size $d = 42\mu m$, which is within the design specification range.

Thus, one possible parameter set is [$a = 500\mu m$; $g = 6.0\mu m$; $b = 12\mu m$; $d = 42\mu m$]. The designed sensor has a touch point pressure of $9.53MPa$ and a sensitivity of $0.7448fF/kPa$.

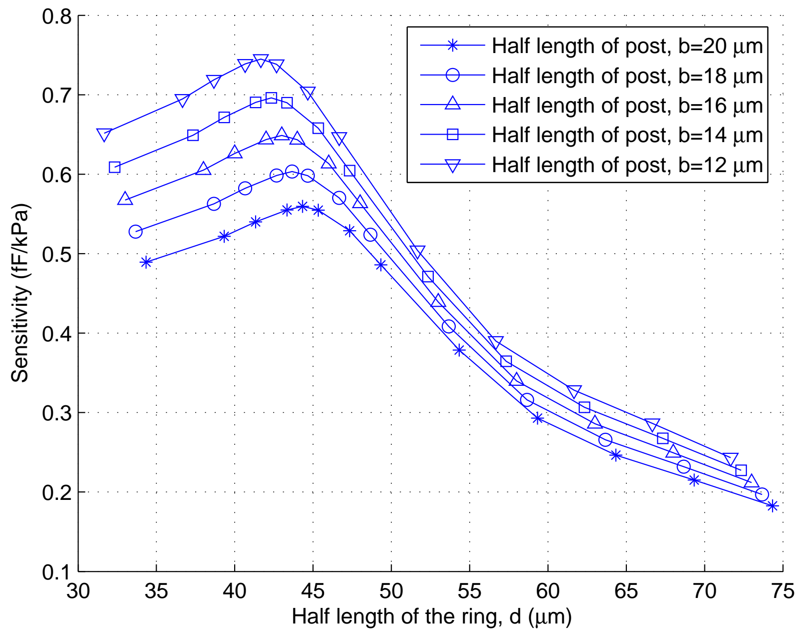

Figure 3.11. Sensitivity vs. boss ring size d, for post size b varying from $12\mu m$ to $20\mu m$, diaphragm size $a = 500\mu m$

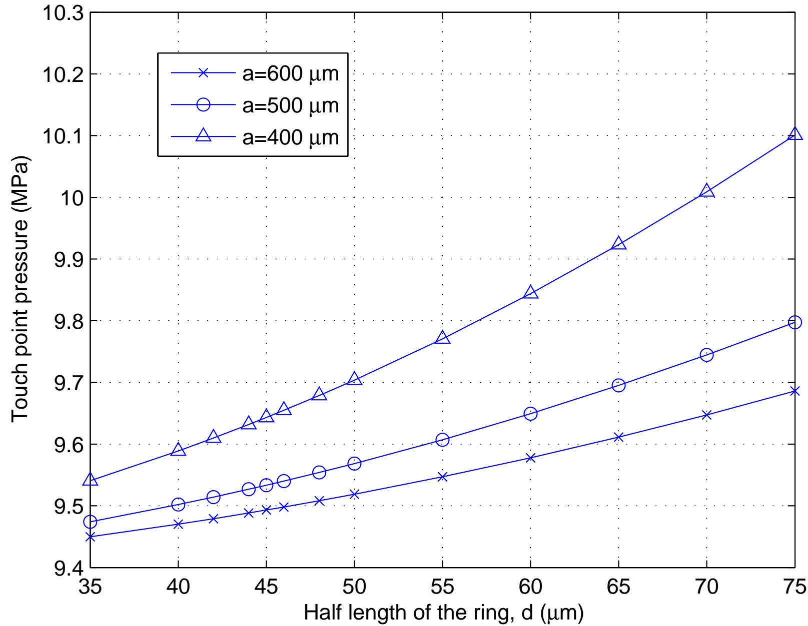

Figure 3.12. Touch point pressure vs. boss ring size d, for post size b varying from $12\mu m$ to $20\mu m$, diaphragm thickness $h_{sen} = 20\mu m$

3.4 Concluding Remarks

In this chapter, design of proposed pressure sensor with two movable diaphragms is presented. First, design issues and constraints, including the structure materials, diaphragm thickness and gap height between parts are discussed according to fabrication processes. Then, effects of geometric parameters on sensitivity are analyzed by using the results from ABAQUS simulations. It shows that increasing diaphragm size leads to sensitivity enhancement, while increasing post size results in the reduced sensitivity. Raising boss ring size may help to enlarge sensitivity, but further increase will make the sensitivity smaller. These parameter analysis provide insight to the sensor design.

Lastly, based on the simulation data of ABAQUS, a graphical design tool is developed for the design of the proposed pressure sensor from the specifications of desired touch point pressure and sensitivity. First, the dimension of the sensing diaphragm is designed. Besides diaphragm thickness that is unchanged in the design, diaphragm sizes and gap height between diaphragms are all designed to be satisfy specifications requirement. Then boss ring size and post size are considered to find a better sensitivity. It is a valuable tool for sensor design that can quickly predict the performance of the sensors.

The graphical design approach only provide valid parameter design ranges for certain specifications and only two parameters can be designed simultaneously in a 2-D plot. Therefore, it may not thoroughly represent the interactions of many parameters and the design result may not be the optimal one. To improve the sensor performance, in an attempt to achieve better possible parameters in term of sensitivity and touch point pressure, etc., optimization approaches will be presented in the subsequent chapters. An analytical model of the proposed sensor, which can provide quick and accurate estimations of sensor behavior and good compatibility to the optimization program, is derived in the next chapter.

Chapter 4

Analytical Model of the Pressure Sensor

4.1 Introduction

In Chapter 2, a pressure sensor with two moveable diaphragms is presented and characterized by using the Finite Element Method software, ABAQUS. Understanding the deflection behavior of the deformable diaphragms in the pressure sensor is necessary for performance estimation and sensor design. Based on the simulation results and analysis obtained from ABAQUS, a graphical tool has been utilized to design device parameters, as described in Chapter 3. The graphical design can provide a direct way to select appropriate parameters that satisfy sensor specifications. However, this method cannot ensure all the sensor parameters are varied and compared at a single step, thus the design set may not be the optimal choice in view of the whole design space.

Sensor design can also be viewed as a multi-objective optimization problem, where genetic algorithm (GA) have extensively been used [64] [65]. Genetic algorithm, which is a robust search technique formulated on the principles of natural selection and natural genetics, may be employed to generate and identify better solutions until convergence is reached. In using genetic algorithm to select the structural parameters of the device, a sensor model is needed to provide accurate

performance index to compare the relative strength of the generated solutions. Although FEM softwares such as ABAQUS can offer a convenient mean to simulate the sensor, it is difficult to integrate GA optimization programs with parameter variations in the FEM model. Therefore, an analytical model that can be implemented in a numerical software such as MATLAB is proposed to replace the FEM model. With the advent of computer programming, the analytical model provides a possible way to study the characteristics of micro sensor and to optimize the sensor structure. For the proposed capacitive pressure sensor, the analytical model presented herein is mainly developed to predict the deformed geometry of the two movable diaphragms. Deformation of the clamped-edge diaphragm is a well-known engineering problem with many existing analysis [66, 67]. Hence, the chanllenging part of the analytical model is to model the interactions between the two diaphragms and the deflection of the cantilever middle diaphragm.

This chapter aims at deriving a theoretical model for the capacitive pressure sensor with two movable diaphragms. The chapter is organized as follows: device variables and elasticity theory that is normally used to analyze diaphragm behavior is introduced first. The deflection model of the clamped edges sensing diaphragm based on Energy Method is presented next. This is followed by the cantilever middle diaphragm deflection after the two diaphragm come into contact. Deflection of both deformable plates are of primary importance for this work, and comparisons between the analytical method and Finite Element Model are made so as to verify the correctness of the proposed analytical model.

4.2 Parameters in the analytical model

The idea of the novel capacitive pressure sensor has been proposed in the previous chapter, Figure. 2.15 shows that the device comprises of an insulated substrate and two deformable square plates, referred to as the sensing plate and the middle plate. In the subsequent development, the following geometric parameters are used to construct the analytical model of the proposed sensor structure:

- a — Side length of square sensing and middle plates;
- h_{sen} — Thickness of the sensing plate;
- h_{mid} — Thickness of the middle plate, $h_{sen} >> h_{mid}$;
- g — Distance between boss ring and the middle plate;
- $2d$ — Width of the square boss ring;
- $2b$ — Width of the square post supporting the middle plate;
- $w(x, y)$ — Deflection of the point (x, y) on the sensing plate;
- w_d — Deflection of the point $(d, 0)$ on the sensing plate;
- P — Uniformly distributed pressure applied to sensing plate;
- Q — Total force exerted by the boss ring on the middle plate;
- N — Intrinsic stress of the sensing plate;
- $z(r)$ — Vertical displacement of the middle plate along the radial direction;
- u — Radial displacement of the middle plate.

The sensing diaphragm is a clamped edges square plate of thickness, h_{sen} and side length, a. The deformation behavior of the sensing diaphragm can be analyzed using plate theory. The use of plate theory is appropriate for the analysis of micromachined thin-film diaphragms. Thin plate or small plate deflection theory is often used, and is appropriate for small deflection cases. For larger deflections, the mechanical behavior becomes dominated by the internal stresses of the diaphragm. Problems in bending dominated structures (small deflections of thin plates) and stress dominated structures (large deflections) are both considered. The conditions for using either theory is summarized as:

For the model of the proposed sensor, an energy method is used to provide an insight to predict the effect of the internal stress on the behavior of the sensing diaphragm. Due to the cantilever structure, the thin middle plate may have a large

Theory	*Conditions*
small deflection	plate deflection $\ll$ 0.2 plate thickness [68]
large deflection	plate deflection $\ll$ 3 plate thickness [69]

Table 4.1. Conditions for Small or Large Deflection Theory

deflection where small deflection theory may not be applicable. In this case, large deflection theories, is employed for the analysis and is presented in section 4.4.

4.3 Deformation of the Sensing Diaphragm

4.3.1 Elastic Model of the Diaphragm

The structure of the sensing plate is shown in Figure. 4.1, where the pressure acting on the diaphragm surface causes deflection in the z direction. In the derivation of the Equation (4.1), it is assumed, due to the small thickness h, that the force is acting in the middle plane (plane $z = 0$) in the Figure. 4.1. This assumption means that the line perpendicular to the middle plane remains perpendicular also to the elastic surface when the deformation occurs. In other words, the changes of the length and the width of the diaphragm are negligible.

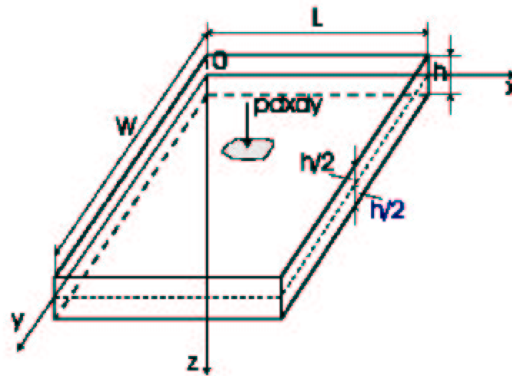

Figure 4.1. The plate with dimensions L and W, exposed to pressure normal to the surface

The deflections w of a rectangular plate with thickness h, pressure load $P(x, y)$

is given by the differential equation [67]:

$$\frac{\partial^4 w}{\partial x^4} + 2\frac{\partial^4 w}{\partial x^2 \partial y^2} + \frac{\partial^4 w}{\partial y^4} = \frac{P(x,y)}{D} \tag{4.1}$$

where D is flexural rigidity of the plate.

$$D = \frac{Eh^3}{12(1-\nu^2)} \tag{4.2}$$

Assumptions

Details of the derivation of Equation (4.1) can be found in Appendix I. There are several important issues must be stressed before using this differential equation:

1. In order to use above equation, the plate material must be elastic, homogenous, continuous and isotropic
2. The equation is valid for small deflections, where the bending deflections are small compared to the thickness of the plate.
3. Deflections in excess of this region result in stretching of the neutral surface and nonlinearities result.

Boundary Constraints

The sensing diaphragm is a rectangular plate with four fixed edges. Along these edges, the plate deflection w is zero, and the tangent plane to the deformed plate shape coincides with the initial the undeformed plate shape.

$$(w)_{x=L} = 0, \qquad \left(\frac{\partial w}{\partial x}\right)_{x=L} = 0 \tag{4.3}$$

Pressure Load

Equation (4.1) is applicable for any pressure distribution that can be expressed as a function of x and y. Since either in hydraulic or in baric pressure measurement, a uniform pressure load is normally applied, so the expression of pressure can be simplified as:

$$P(x,y) = P, (0 < x < L, 0 < y < W) \tag{4.4}$$

In Equation (4.1), the in-plane stresses are neglected, and the resolution can be obtained by using several techniques [25, 70]. However, in micro devices, diaphragms formed by micromachined processes always contain residual stress, the in-plane stress in the diaphragm always play an important role or even dominate the mechanical response. Therefore, other approaches that consider the diaphragm internal stress will be better to model the deformation of the sensing plate. Predicting the deflection of sensing diaphragm accurately is important for further analysis of the cantilever middle diaphragm, since the movement of boss ring on the sensing diaphragm is a key parameter that affect middle diaphragm deflection.

4.3.2 Energy Method

Figure. 4.2 shows an elemental unit in the sensing diaphragm. The bending moments M_x and M_y and the twisting moments M_{xy} andM_{yx} are also included when considering the bending of plate. There are vertical shearing forces Q_x and Q_y acting on the sides of the element. All other forces and moments are considered negligible, since the strain of the middle plane of the plate is also neglected. Therefore, the equilibrium of the element can be completely defined by the equilibrium of forces in z direction, and equilibriums of moments with respect to x axis and y axis.

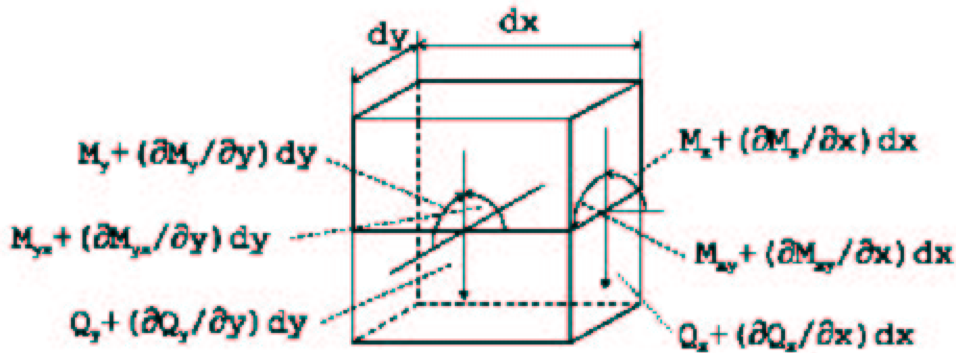

Figure 4.2. An element in the plate under applied forces

$$\frac{\partial M_{xy}}{\partial x} - \frac{\partial M_y}{\partial y} + Q_y = 0 \tag{4.5}$$

$$\frac{\partial M_{yx}}{\partial y} + \frac{\partial M_x}{\partial x} - Q_x = 0 \tag{4.6}$$

If considering the residual stress $N_x = N_y = N$ in the sensing diaphragm, the sum of forces in the z-direction is therefore:

$$0 = P + \frac{\partial Q_x}{\partial x} + \frac{\partial Q_y}{\partial y} + N_x \frac{\partial^2 w}{\partial x^2} + N_y \frac{\partial^2 w}{\partial y^2} \tag{4.7}$$

By substituting Equation (4.5) and Equation (4.6) into Equation (4.7), shearing forces Q_x and Q_y is eliminated and the following equation is obtained:

$$\frac{\partial^2 M_x}{\partial x^2} + \frac{\partial^2 M_{yx}}{\partial x \partial y} + \frac{\partial^2 M_y}{\partial y^2} - \frac{\partial^2 M_{xy}}{\partial x \partial y} = -\left[P + N\left(\frac{\partial^2 w}{\partial x^2} + \frac{\partial^2 w}{\partial y^2}\right)\right] \tag{4.8}$$

The external moments M_x, M_y and $M_x y$ can be obtained by integration of moments per unit length from $z = -h/2$ to $z = h/2$:

$$M_x = D(\frac{1}{r_x} + \nu\frac{1}{r_y}) = -D(\frac{\partial^2 w}{\partial x^2} + \nu\frac{\partial^2 w}{\partial y^2}) \tag{4.9}$$

$$M_y = D(\frac{1}{r_y} + \nu\frac{1}{r_x}) = -D(\frac{\partial^2 w}{\partial y^2} + \nu\frac{\partial^2 w}{\partial x^2}) \tag{4.10}$$

$$M_{xy} = -M_{yx} = D(1-\nu)\frac{\partial^2 w}{\partial x \partial y} \tag{4.11}$$

It is more convenient to express in the form of plate in z direction, denoted as w. Observing that $M_{yx} = -M_{xy}$, the diaphragm deformation can be modelled using the general equation for static displacement of a thin plate in the $x - y$ plane. Replacing M_x, M_y and M_{xy} by Equation (4.10), Equation (4.11) and Equation (4.11), Equation (4.8) can be expressed as:

$$\frac{\partial^4 w}{\partial x^4} + 2\frac{\partial^4 w}{\partial x^2 \partial y^2} + \frac{\partial^4 w}{\partial y^4} = \frac{1}{D}\left[P + N\left(\frac{\partial^2 w}{\partial x^2} + \frac{\partial^2 w}{\partial y^2}\right)\right] \tag{4.12}$$

D is stiffness of the plate as defined in Equation (4.2), w is the amount of vertical deflection at point (x, y), P is the applied pressure, E is Young's modulus, ν is the Poisson's ratio and N is the internal stress function. The difference between Equation (4.12) and Equation (4.1) is that the effects of internal stress N have been considered in plate deflection.

To calculate the deflections of rectangular plates with internal stress under a uniform pressure, a method that study diaphragm energy may be used. The solution to the Equation (4.12) can be found using energy methods. Energy methods used here utilizes the principal of energy conservation. The micro capacitive pressure sensor is exposed to a uniform hydraulic pressure. Since the applied pressure changes slowly, kinetic energy may be neglected. Hence, the amount by which the sensing plate deflects is the equilibrium point where the work performed by the applied pressure is balanced by the static energy stored in the plate [70]. The total static energy, U, in the diaphragm is the sum of the bending energy of the plate and the energy due to the effect of internal stress. Equation (4.13) contains the mathematical expression for the static energy, U [67].

$$U = \underbrace{\frac{D}{2}\int\int\left(\frac{\partial^2 w}{\partial x^2}+\frac{\partial^2 w}{\partial y^2}\right)^2 - 2(1-\nu)\left(\frac{\partial^2 w}{\partial x^2}\frac{\partial^2 w}{\partial y^2}-\left(\frac{\partial^2 w}{\partial x \partial y}\right)^2\right)dxdy}_{\text{bending energy}}$$
$$+\underbrace{\frac{N}{2}\int\int\left(\frac{\partial w}{\partial x}\right)^2+\left(\frac{\partial w}{\partial y}\right)^2 dxdy}_{\text{internal stress}} \tag{4.13}$$

At each point in the plate, the work done by the applied force Pa^2 along a distance dw is equal to the change in the total energy U. The principle of virtual displacement states that

$$\frac{\partial U}{\partial b_{mn}}\Delta b_{mn} = Pa^2 \cdot \Delta w(x,y) \tag{4.14}$$

where b_{mn} is the coordinates defining the shape of the deflection surface and $w(x,y)$ is the displacement perpendicular to the plate surface. The deflection surface of the loaded plate can be approximated by series functions. These functions have zero value and zero first derivatives at the plate edges, in order to satisfy the the boundary condition of clamped edges. Moreover, a uniformly distributed pressure implies that the deflections are symmetrical. The assumed displacements $w(x,y)$ are:

$$w(x,y) = \sum_{m=1,2,..}^{\infty}\sum_{n=1,2,..}^{\infty} b_{mn}\left[1-(-1)^m\cos\left(m\frac{2\pi x}{a}\right)\right]\left[1-(-1)^n\cos\left(n\frac{2\pi y}{a}\right)\right] \tag{4.15}$$

So Equation. (4.14) can be rewritten as:

$$\frac{\partial U}{\partial b_{mn}} \Delta b_{mn} = Pa^2 \cdot \Delta b_{mn} \left[1 - (-1)^m \cos\left(m\frac{2\pi x}{a}\right)\right] \left[1 - (-1)^n \cos\left(n\frac{2\pi y}{a}\right)\right] \tag{4.16}$$

The coefficients b_{mn} can be determined as

$$b_{mn} = \frac{Pa^4}{4\pi^4 D(3m^4 + 2m^2n^2 + 3n^4) + 3\pi^2 a^2 N(m^2 + n^2)} \tag{4.17}$$

4.3.3 Analysis of internal stress

The residual stresses in the diaphragms are the important parameters in establishing the reliability of the structure and the performance of the sensor. In order to fully understand and predict the reliability and performance of the sensor, it is imperative that the effect of diaphragm stress be analyzed and quantified. From semiconductor fabrication technology, it is founded that the typical residual stresses are developed in silicon wafers during the growth of boules as well as in thermal processing. The stresses can be measured by various methods, and has a typical magnitude of $1.4 - 1.5MPa$ [71][72].

The deflection profiles for a $500\mu m \times 500\mu m$ diaphragm with a $10MPa$ pressure load is plotted in Figure. 4.3. Due to the symmetry of the square plate, it is sufficient to only show half of the diaphragm profile. The profiles are calculated for $0MPa$ and $\pm 1.5MPa$ internal stresses. From Equation (4.15), it can be seen that for plates with tensile stress where N is a positive value, b_{mn} tends to be a smaller than the case of zero stress. The tensile plates has less deflections with given loads. By definition, tensile stress will cause the plate to stiffen. On the other hand, plates from films with compressive stress have reduced stiffness, and deflections are increased. When the compressive intrinsic stress is further increased for a plate with fixed geometry, the plate may deflect, even without externally applied loads. This is the case of buckling. Buckling behavior is usually undesirable in micro mechanical sensor and devices. Largest deflection on the sensing diaphragm are obtained using both the energy method in Equation (4.15) and the small deflection method, as shown in Figure. 4.4. All the curves are nearly the same for low pressure

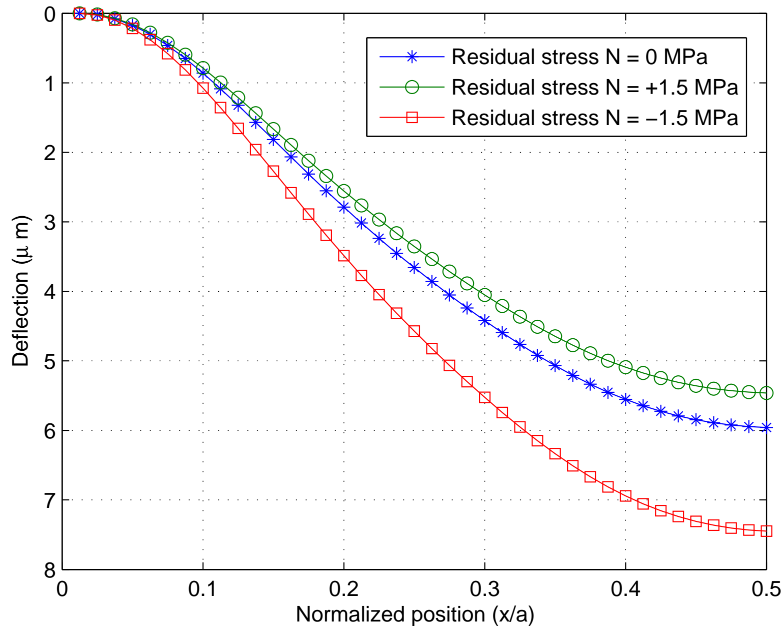

Figure 4.3. Deflection profile of a square sensing diaphragm. $h_{sen} = 20\mu m$, $a = 500\mu m$, $P = 10MPa$

loads and diverge for larger loads, with small deflection theory overestimating the actual deflection. The diaphragm of tensile internal stress of $1.5MPa$ shows smaller deflection than the diaphragm with no built-in stress.

4.4 Deformation of the Cantilever Middle Plate

In previous section, the deflection of the sensing diaphragms are calculated using an energy method. This method accounts for the deflection analysis of diaphragm with large loads and residual stresses. As stated before, small deflection theory generally only predicts diaphragm behavior accurately for deflections less than one fifth of the diaphragm thickness. Beyond this point, diaphragm stretching and membrane stress become significant and tend to decrease the amount of deflection. Large deflection theory is used to model the middle plate deformation.

The middle plate is a thin square diaphragm of uniform thickness. The four edges are free standing and it has a post at the center. When the applied pressure

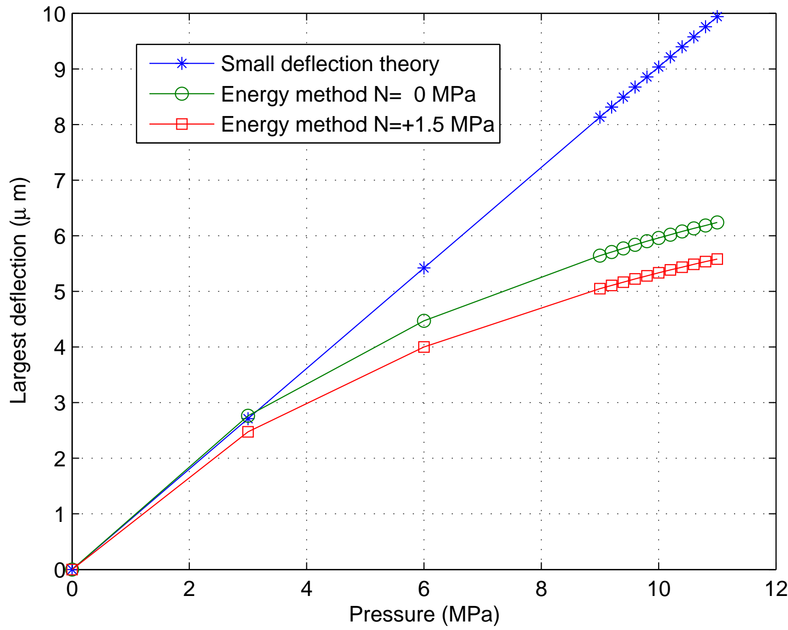

Figure 4.4. Largest deflection vs. applied pressure. $h_{sen} = 20\mu m$, $a = 500\mu m$

exceeds a threshold value, the boss ring on the glass substrate comes into contact with the middle plate and forces it to bend. As the interactions between the boss ring and square-shape cantilever diaphragm is complex, the task of building a model to predict the deflection of middle plate is not straight forward. One problem is the shape of the diaphragm. Square plates are commonly used in micro sensors because the shape can be easily fabricated. On the other hand, it is easier to analyze the deflection of a circular plate using cylindrical co-ordinates. The methodology adopted in this paper is to first construct a model for predicting how a circular plate, supported at the center, would deform under an external force before extending the results to the case of a square plate.

4.4.1 Circular Model

Consider a circular plate of radius $0.5a$ that is supported at the center by a circular post of radius b. Q is the total force applied uniformly on the middle plate by a circular boss ring of radius d. Figure. 4.5 shows the cross-sectional view of the circular cantilever structure. Due to the symmetrical property of circular plates,

it may be assumed that the deformation is independent of angle, θ. Hence, it is sufficient to only analyze an elemental unit in a sector of the circular plate. The forces and moments the elemental unit directly under the boss ring is illustrated in Figure. 4.6. dr and $d\theta$ define the size of the element unit and $z(r)$ is the vertical displacement of points lying on a circle of radius r. F_r and F_θ are the inner forces in the radial and tangential directions, while M_r and M_θ are the moments. N_z is the shear force perpendicular to the plate.

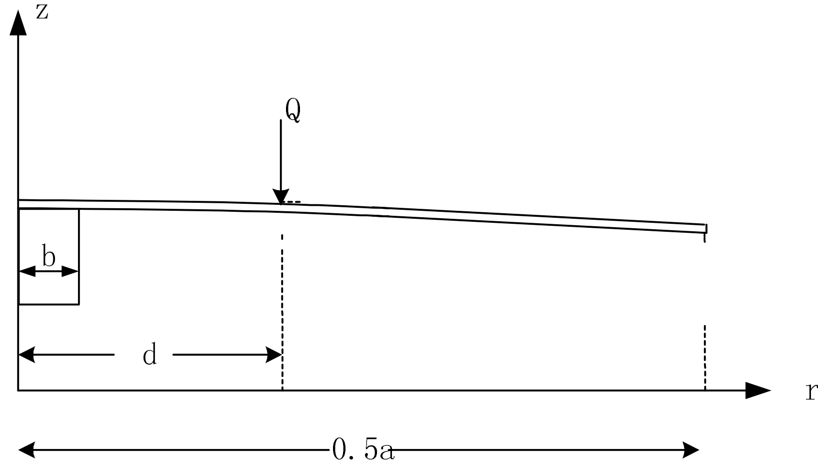

Figure 4.5. Cross section view of half circular plate

When force is applied, the plate deforms. A general point initially at the radius r will move to a new radius $r + u - (dz/dr)z$, where u represents the displacement in radial direction. Hence, expressions [73] representing strain in the radial (ε_z) and tangential direction (ε_θ) are

$$\varepsilon_r = \frac{du}{dr} + \frac{1}{2}\left(\frac{dz}{dr}\right)^2 - \frac{d^2 z}{dr^2}z, \tag{4.18}$$

$$\varepsilon_\theta = \frac{u}{r} - \frac{dz}{dr}\frac{z}{r} \tag{4.19}$$

Applying Hooke's law, the stresses can be determined from the strains as :

$$\begin{aligned} \sigma_r &= \frac{E}{1-\nu^2}(\varepsilon_r + \nu\varepsilon_\theta) \\ \sigma_\theta &= \frac{E}{1-\nu^2}(\varepsilon_\theta + \nu\varepsilon_r) \end{aligned} \tag{4.20}$$

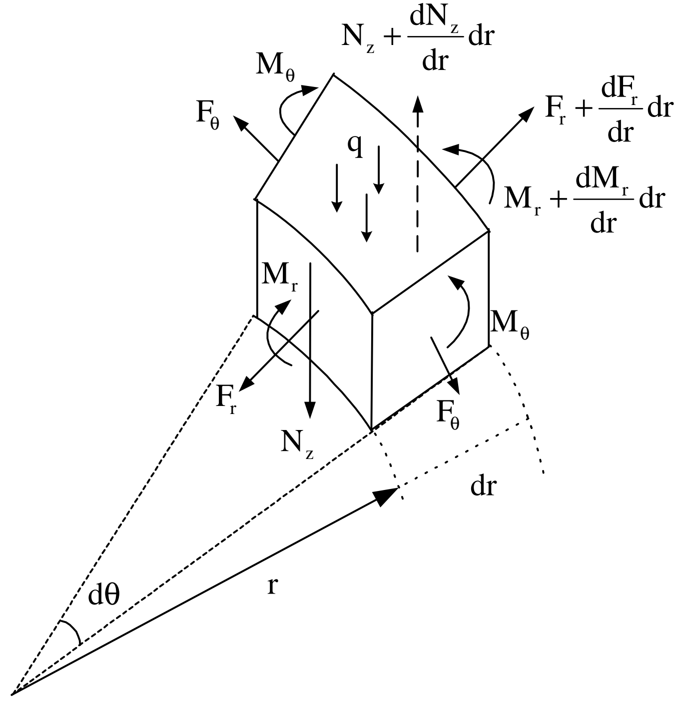

Figure 4.6. Forces and Moments acting on an element unit of a circular plate

ν is the Poisson's ratio. As the plate deflection z is very small compared to the plate radius (r), the last term in Equation (4.18) and (4.19) can be neglected. Hence, the tensile force per unit length, in radial direction, can be obtained by integrating σ_r along the plate thickness (h) :

$$F_r = \int_0^h \sigma_r dt = \frac{Eh}{1-\nu^2}\left[\frac{du}{dr} + \frac{1}{2}\left(\frac{dz}{dr}\right)^2 + v\frac{u}{r}\right] \tag{4.21}$$

In the same way, the tensile force per unit length of section in tangential direction is given by :

$$F_\theta = \int_0^h \sigma_\theta dt = \frac{Eh}{1-\nu^2}\left[\frac{u}{r} + \frac{\nu}{2}\left(\frac{dz}{dr}\right)^2 + \nu\frac{du}{dr}\right] \tag{4.22}$$

The bending moments per unit length in radial and tangential directions [73] [74]:

$$M_r = -D\left(\frac{d^2z}{dr^2} + \frac{\nu}{r}\frac{dz}{dr}\right) \tag{4.23a}$$

$$M_\theta = -D\left(\frac{1}{r}\frac{dz}{dr} + \nu\frac{d^2z}{dr^2}\right) \tag{4.23b}$$

Summation of the moments about the center tangential axis of the element

shown in Figure. 4.6 gives

$$\begin{aligned}\sum M \quad = 0 = \quad & (M_r + dM_r)(r + dr)d\theta - M_r r d\theta - 2M_\theta dr \sin\frac{d\theta}{2} \\ & +(N_z + dN_z)(r + dr)\frac{dr}{2}d\theta + N_z r\frac{dr}{2}d\theta \end{aligned} \tag{4.24}$$

By assuming that $d\theta$ is very small, $\sin\frac{d\theta}{2}$ can be reduced to $\frac{d\theta}{2}$. Neglecting the high order derivatives,

$$\begin{aligned} & 0 = M_r dr + dM_r r - M_\theta dr + N_z r dr \\ & \Longrightarrow N_z = -\frac{dM_r}{dr} - \frac{M_r - M_\theta}{r} \end{aligned} \tag{4.25}$$

Substituting Equation (4.23) into Equation (4.25) yields

$$N_z = -D\left(\frac{d^3 z}{dr^3} + \frac{1}{r}\frac{d^2 z}{dr^2} - \frac{1}{r^2}\frac{dz}{dr}\right) \tag{4.26}$$

To maintain static equilibrium, the sum of all forces and moments on a body should be zero. Thus, the transverse equilibrium equation holds :

$$D\left(\frac{d^4 z}{dr^4} + \frac{2}{r}\frac{d^3 z}{dr^3} - \frac{1}{r^2}\frac{d^2 z}{dr^2} + \frac{1}{r^3}\frac{dz}{dr}\right) = Q' + F_r\frac{d^2 z}{dr^2} + F_\theta dz dr \tag{4.27}$$

Q' is the force exerted that may be exerted by the boss ring on the elemental unit under study. When the deflections are small, the nonlinear term $\frac{d^2 z}{dr^2}$ can be ignored. Therefore, the F_r and F_θ terms in Equation (4.21) and (4.22) can be regarded to be constant values that are independent of z and $\frac{1}{D}\left[\frac{Q}{2\pi d} + F_r\frac{d^2 z}{dr^2} + F_\theta dz dr\right]$ becomes a constant value C. Defining $\frac{dz}{dr}$ as k and substituting into Equation (4.27),

$$\frac{d^3 k}{dr^3} + \frac{2}{r}\frac{d^2 k}{dr^2} - \frac{1}{r^2}\frac{dk}{dr} + \frac{1}{r^3}k = C \tag{4.28}$$

The ordinary differential equation, labelled as Equation (4.28) can be solved by the variable replacement method. Let $r = e^t$, then $t = \ln r$ and

$$\begin{aligned} \frac{dk}{dr} &= \frac{dk}{dt}\frac{dt}{dr} = \frac{1}{r}\frac{dk}{dt} \\ \frac{d^2 k}{dr^2} &= \frac{d}{dt}\left(\frac{1}{r}\frac{dk}{dt}\right) = -\frac{1}{r^2}\frac{dk}{dt} + \frac{1}{r^2}\frac{d^2 k}{dt^2} \\ \frac{d^3 k}{dr^3} &= \frac{d}{dt}\left(-\frac{1}{r^2}\frac{dk}{dt} + \frac{1}{r^2}\frac{d^2 k}{dt^2}\right) = \frac{1}{r^3}\left(\frac{d^3 k}{dt} - 3\frac{d^2 k}{dt^2} + 2\frac{dk}{dt}\right) \end{aligned} \tag{4.29}$$

Substituting the expressions into Equation (4.28),

$$\frac{d^3k}{dt^3} - \frac{d^2k}{dt^2} - \frac{dk}{dt} + k = Ce^{3t} \tag{4.30}$$

The roots of the characteristic equation -1, 1 , 1, so the general solution is

$$k = C_1e^t + tC_2e^t + C_3e^{-t} \tag{4.31}$$

where C_1, C_2, C_3 are constant coefficients. Since $k = \frac{dz}{dr}$ by definition, $z(t)$ can be derived by integrating Equation (4.31).

$$\begin{aligned} z(t) &= \int r\frac{dz}{dr}dt = \int e^t(C_1e^t + tC_2e^t + C_3e^{-t})dt \\ &= C_0 + C_1e^{2t} + \frac{C_2}{2}\left(te^{2t} - e^{2t}\right) + C_3t \\ &= C_0 + \left[C_1 - \frac{1}{2}C_2\right]e^{2t} + C_3t + \frac{1}{2}C_2te^{2t} \end{aligned} \tag{4.32}$$

Replacing t by $\ln r$, the deflection of points on the circular middle plate are

$$z(r) = A_0 + A_1r^2 + A_2\ln r + A_3r^2\ln r \qquad 0 \leq r \leq 0.5a \tag{4.33}$$

A_0, A_1, A_2, A_3 are constant terms that depend on the boundary conditions. From the cross-sectional diagram of the middle plate shown in Figure. 4.5, it may be deduced that the plate can be divided into two regions : (i) the area inside the boss ring, referred to as the inner region ($b < r < d$), and (ii) the outer region ($d < r < 0.5a$). The coefficients of Equation (4.33) for each of the region will be derived next.

Inner region ($b < r < d$)

Both end-points of this region are constrained, one end ($r = b$) by the post supporting the plate and the other end ($r = d$) by contact area of the boss ring. Hence, the transverse shear force (N_z) is non-zero and should be equal to the external applied force. As Q represents the total force exerted by the boss ring on the middle plate and the circumference of the boss ring is $2\pi d$, the external force acting on an elemental unit is $\frac{Q}{2\pi d}$. Thus,

$$N_z = -D\left(\frac{1}{r^2}\frac{dz}{dr} - \frac{1}{r}\frac{d^2z}{dr^2} - \frac{d^3z}{dr^3}\right) = \frac{Q}{2\pi d} \tag{4.34}$$

Substituting Equation (4.33) into Equation (4.34) :

$$\frac{1}{r^2}\left[2A_1 r + A_2\frac{1}{r} + A_3(2r\ln r + r)\right] - \frac{1}{r}\left[2A_1 - A_2\frac{1}{r^2} + A_3(2\ln r + 3)\right] - \left[A_2\frac{1}{r^3} + A_3\frac{2}{r}\right] = \frac{-Q}{2\pi Dd} \tag{4.35}$$

The expression can been further simplified to:

$$\frac{A_2}{r^3} - 4\frac{A_3}{r} = \frac{-Q}{2\pi Dd} \tag{4.36}$$

Equation (4.34) is satisfied if $A_2 = 0, A_3 = \frac{Q}{8\pi D}$. $z(r)$ can therefore be expressed as:

$$z(r) = A_0 + A_1 r^2 + \frac{Q}{8\pi Dd} r^3 \ln r \tag{4.37}$$

The remaining parameters are selected using the boundary conditions. In this region, vertical displacement z and the slope $\frac{dz}{dr}$ must be zero at the edge of the post $r = b$. The boss ring touches the middle plate at the point $r = d$. Compared to top plate, the middle plate is thin and flexible. Therefore, displacement of points that comes into contact with the boss ring, $z(b)$, is determined by top plate movement so the following condition holds:

$$z(d) = w(d, 0) - g = w_d - g \tag{4.38}$$

where g is the gap between top plate boss ring and middle plate and $w_d = w(d, 0)$ is the deflection of the top plate near the boss ring. Thus, the boundary conditions of this regions are :

$$z(b) = 0, \qquad \frac{dz(b)}{dr(b)} = 0, \qquad z(d) = w_d - g \tag{4.39}$$

Using the conditions in Equation (4.39), the unknown terms in Equation (4.37) are found to be

$$A_0 = \frac{Qb^3}{16\pi Dd}(\ln b + 1) \tag{4.40a}$$

$$A_1 = -\frac{Qb}{16\pi Dd}(3\ln b + 1) \tag{4.40b}$$

$$Q = \frac{16\pi Dd(w_d - g)}{b^3 \ln b + b^3 - 3bd^2 \ln b - bd^2 + 2d^3 \ln d} \tag{4.40c}$$

Outer region ($d < r < 0.5a$)

Unlike the inner region where both ends are constrained, one edge ($r = 0.5a$) of the outer region is free because the middle plate is structured as a cantilever. Since the outer edge is unloaded,the transverse shearing force N_z is zero:

$$N_z = -D\left(\frac{1}{r^2}\frac{dz}{dr} - \frac{1}{r}\frac{d^2z}{dr^2} - \frac{d^3z}{dr^3}\right) = 0 \tag{4.41}$$

Substituting $\frac{dz}{dr}$ with k, Equation (4.41) becomes

$$\frac{d^2k}{dr^2} + \frac{1}{r}\frac{dk}{dr} - \frac{1}{r^2}k = 0 \tag{4.42}$$

Via the variable replacement approach where r is replaced by e^t, the preceding equations reduces to

$$\frac{d^2k}{dt^2} - k = 0 \tag{4.43}$$

The eigenvalues are 1 and -1, so the solution of the ordinary differential equation has following general form:

$$k = C_1e^t + C_2e^{-t} = C_1r + C_2\frac{1}{r} \tag{4.44}$$

By definition, $k = \frac{dz}{dr}$ so $z(r)$ can be recovered by integrating Equation (4.44).

$$\begin{aligned} z(r) &= \int k dr = C_0 + \frac{1}{2}C_2r^2 + C_3\ln r \\ &= B_0 + B_1r^2 + B_2\ln r \end{aligned} \tag{4.45}$$

where $C_0, C_1, C_2, B_0, B_1, B_2$ are constant coefficients that are determined by boundary conditions. Since one end of the region ($r = d$) comes into contact with the boss ring, the deflection at this point should be equal to the sensing plate deflection. The gradient of the surface must also be continuous. Lastly, the moment at the edge of the plate ($r = 0.5a$) is zero since it is unloaded. Therefore, the boundary conditions are

$$z(d) = w_d - g, \qquad \frac{dz(d^+)}{dr} = \frac{dz(d^-)}{dr}, \qquad M_r(0.5a) = 0 \tag{4.46}$$

Using the boundary conditions, the coefficients of Equation (4.45) are found to be

$$B_0 = w_d - g - B_2 \left[\ln d + \frac{2d^2(1-\nu)}{a^2(1+\nu)} \right] \quad (4.47a)$$

$$B_1 = \frac{2(1-\nu)}{a^2(1+\nu)} B_2 \quad (4.47b)$$

$$B_2 = \frac{Q}{4\pi D} d^2 \ln \frac{d}{b} - \frac{1-\nu}{1+\nu} \frac{4d^2}{a^2} \quad (4.47c)$$

4.4.2 Square Model

Linear interpolation method is used to extend the results of circular plates to square plate. As the square and circular models employ different co-ordinate systems, the cartesian co-ordinate (x, y) is first converted into cylindrical co-ordinates (r, θ) using the following relationship :

$$\theta = \tan^{-1}\left(\frac{y}{x}\right), \quad r = \sqrt{x^2 + y^2}$$

Then, the cylindrical co-ordinate is used in a circular model to get the plate displacement. The deflections of square plate may be computed by interpolating those diaplacements:

$$z(x, y) = \frac{1}{n} \sum_{i=1}^{n} z_i(r\cos\theta, r\sin\theta) \quad (4.48)$$

where n is the number of circular models. Since the deflection of the square can be assumed to be symmetrical, the deformation of only one quarter $(0 < \theta < 45^o)$ of the square plate needs to be found.

4.5 Evaluation of Analytical Model

The theoretical model of the proposed micro capacitance pressure sensor is evaluated by comparing against the results obtained using a commercial general-purpose FEM package, ABAQUS. The study is conducted using a device that has the following structure :

- Side length of square sensing and middle plates, $a = 500\mu m$

- Thickness of the sensing plate, $h_{sen} = 20\mu m$
- Thickness of the middle plate, $h_{mid} = 1.75\mu m$
- Distance between boss ring and the middle plate, $g = 6\mu m$
- Width of the square boss ring, $d = 75\mu m$
- Width of the square post supporting the middle plate, $b = 50\mu m$

The sensing diaphragm deformation is defined by Equation (4.15). Figure. 4.7 shows the three dimensional deflection of the sensing plate obtained by implementing Equation (4.15) in MATLAB and calculating the displacement of each node. In the simulation, the material of the diaphragm is set to be silicon, so the Young's modulus E and Poisson's ratio ν are $130GPa$ and 0.2783 respectively, as discussed in section 2.2.1. The internal stress N is taken to be $+0.5MPa$ and a load of 10.0 MPa is applied uniformly to the entire diaphragm. Figure. 4.8 compares the deflection of the center point obtained using the energy method (Equation 4.15) with the value generated via ABAQUS. The plot in Figure. 4.8 indicates that the difference between the deflection data obtained by the energy approach and that calculated by ABAQUS. Hence, it may be concluded that the simple theoretical model Equation (4.15) may be employed in place of the complex FEM package to ascertain the top plate deformation.

As discussed in Chapter 2, the middle diaphragm is made of polysilicon by using thin film technology. From section 2.2.1, typical mechanical properties of Polysilicon are used, including a Young's Modulus of $165GPa$, and a poisson's ratio of 0.22. To construct the deformation of the square cantilever middle plate, the four circular models tabulated in Table 5.1 are first derived. Using Equation (4.48), the results of the four circular models are interpolated to construct the deformation of the square plate. Figure. 4.9 shows 3-D deflection of a square middle plate under the force applied by the boss ring. Due to the cantilever structure, the largest deflection occurs at the corners of the plate. It shows that boss ring comes into contact with the cantilever middle plate when the applied pressure is around

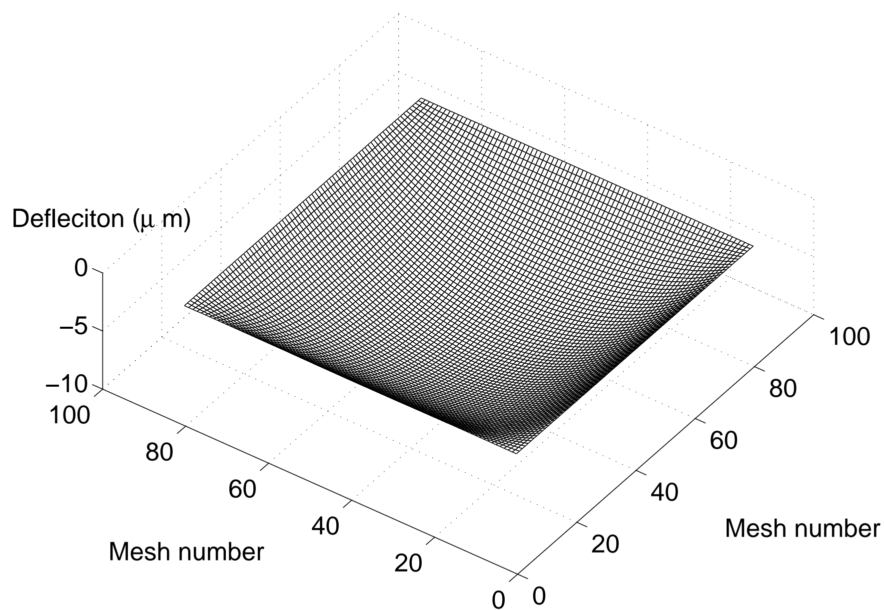

Figure 4.7. 3-D deformation shape of the top plate calculated by the energy method. side length $a = 500\mu m$, thickness $h_{sen} = 20.0\mu m$, mesh size $= 6.25\mu m$, internal stress $= 0.5MPa$

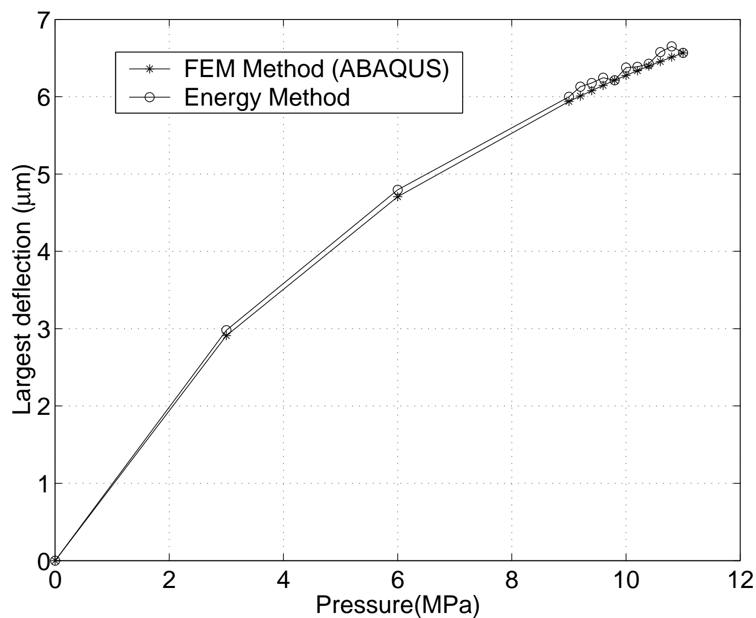

Figure 4.8. Comparison of diaphragm center deflections using different methods.

$9.8MPa$. After the two plates come into contact, the analytical method give rise to a deflection-pressure curve that has a larger slope. Although the difference

appear to be large, it should be noted that computing the largest deflections is more complex. The average deviation between the theoretical and FEM model is smaller than the difference at diaphragm corners.

Model Index (n)	Angle on square plate	Circular plate radius	Circular ring width	Circular post width
1	0°	$0.5a$	$1.0d$	$1.0b$
2	15°	$0.518a$	$1.036d$	$1.036b$
3	30°	$0.578a$	$1.156d$	$1.156b$
4	45°	$0.707a$	$1.414d$	$1.414b$

Table 4.2. Linear interpolation method using circular models

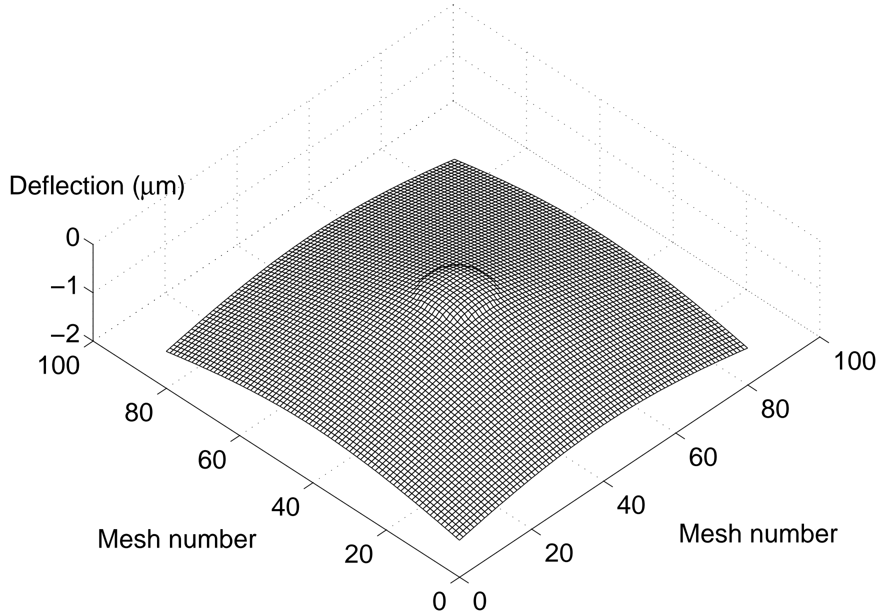

Figure 4.9. 3-D deformation of the square middle plate from the interpolation method. side length $a = 500\mu m$, thickness $h_{mid} = 1.75\mu m$, mesh size $s = 6.25\mu m$.

Since the deflection of points on both the sensing and middle diaphragms are known, the capacitance of the parallel plate capacitor formed by the middle diaphragm and the substrate can be calculated by the integration method, as described in section 2.3.

In Figure. 4.10, the result of ABAQUS simulation discussed in chapter 2 and result of the analytical method proposed in this chapter are compared. Initially, the output capacitance changes slowly as the pressure increases. After the applied pressure exceeds 9.8 MPa, the touch point, the two plates come into contact with each other and the capacitance begins to change at a higher rate. The maximum error between two methods occurs at the point where pressure is much larger than the touch point pressure. The percentage modelling error is defined as

$$\frac{C_{ANA} - C_{FEM}}{C_{EM}} \times 100\% \tag{4.49}$$

where C_{ANA} and C_{FEM} are the capacitances obtained using plate deformation data generated by the proposed analytical model and the FEM approach respectively. The maximum percentage modelling error for the case shown in Figure. 4.10 is 8.24%. Since the model accuracy depends on the mesh size, the percentage modelling error corresponding to plate deflection results obtained using different mesh sizes are tabulated in Table 4.3. When mesh size is reduced from 12.5μm to 6.25μm, the modelling errors between analytical model and ABAQUS simulation decreases to 3.21%.

Mesh size (μm)	$S_{FEM}(pF)$	$S_{ANA}(pF)$	Largest Modelling Error
12.5	0.8432	0.9127	8.24%
8.33	0.8432	0.8975	6.44%
6.25	0.8432	0.8703	3.21%

Table 4.3. Comparison of percentage modelling error for different mesh sizes, at touch point pressure 10.0MPa

The sensitivity $\frac{dC}{dP}$ of the device to pressure change is an important performance index that determines the usefulness of the sensor. It is, therefore, important for the theoretical model to provide an accurate prediction of the pressure sensitivity. Since the C-P curve is non-linear, the sensitivity is defined as the slope of C-P curve obtained by fitting the data, in a least-square sense, to a first order polynomial. Table 4.4 shows the pressure sensitivity of the proposed and FEM model, as well as the deviation between the two approaches. As the modelling error and the

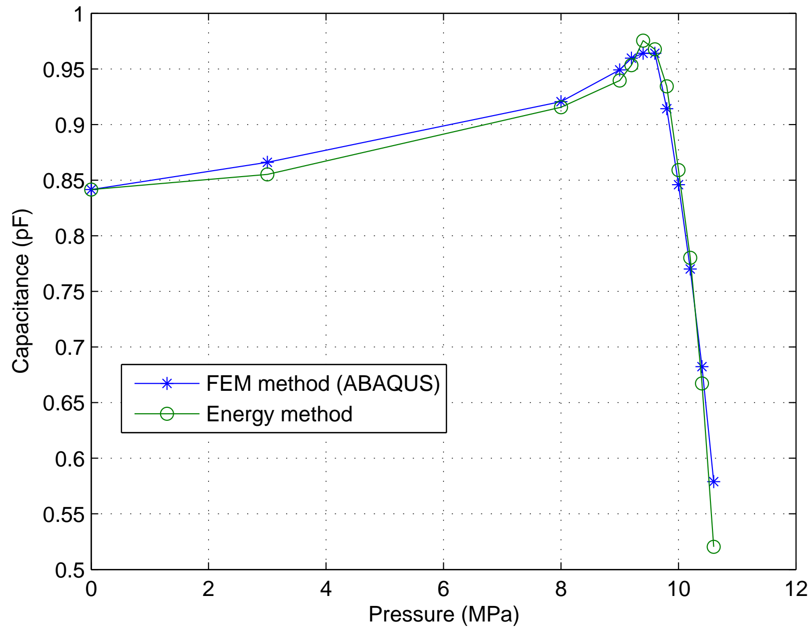

Figure 4.10. Comparison of sensor characteristics from the analytical model and ABAQUS

sensitivity variation is as low as 3.5% when mesh size is $6.25\mu m$, it can be concluded that the proposed analytical model is sufficiently accurate.

Mesh size (μm)	$S_{FEM}(fF/kPa)$ (ABAQUS)	$S_{ANA}(fF/kPa)$ (Analytical)	Sensitivity deviation $\frac{\lvert S_{ANA}-S_{FEM}\rvert}{S_{FEM}} \times 100\%$
12.5	0.5162	0.5689	10.21%
8.33	0.5162	0.5518	6.89%
6.25	0.5162	0.5347	3.5%

Table 4.4. Comparison of pressure sensitivity deviation for different mesh sizes

4.6 Conclusions

In this chapter, the analytical model of the proposed capacitive pressure sensor is developed. It provides a simple and quick alternative way to estimate characteristics of sensor device. In order to estimate the deflection of the sensing plate,

energy method is employed which can account for the effect the film internal stress. The middle plate deflection behavior is much complex and the analytical method based on plate theory is proposed. The analytical model can predict deformation behaviors of both plates, and capacitances computed accordingly have 3.21% difference with ABAQUS result when proper mesh sizes ($6.25\mu m$) are chosen. Since the model provides accurate prediction and can be easily implemented in general-purpose mathematical packages such as MATLAB, it can be combined with computational intelligence techniques and used to optimize the sensor structure.

Chapter 5

Sensor Optimal Design using Genetic Algorithm

5.1 Introduction

The analytical model of the proposed pressure sensor has been presented in Chapter 4. Compared with the simulation results of FEM software ABAQUS, the analytical model also shows a accurate prediction of the diaphragm behaviors, with a modelling error as small as 3.2%. Furthermore, the model is constructed and analyzed in Matlab, a widely used mathematical software, and sophisticated evolution techniques can be easily incorporated into the model so as to achieve optimal design. Design and optimization of sensor parameters using the established analytical model is desirable because the evaluation of sensor performance is based on the whole design space, where all the device parameters can be varied simultaneously.

The goal of the optimal design is to improve the sensor performance as much as possible. As discussed in Chapter 3, there are two performance specifications that need to be achieved, including touch point pressure P_t and Sensitivity S. The optimal design is implemented by searching through the large number of possible solutions to discover the best specific solution. Due to the unique sensor structure and the interactions between sensor parameters, the search process is often intricate and time consuming. However, by exploiting the natural evolution and adaptation

processes in biological systems, genetic algorithm can be used to solve the search problem in a quick and efficient way.

This chapter starts from explaining the basic idea of genetic algorithm. Then a multi-objective evolutionary algorithm (MOEA), is presented to solve the optimal design problem of the proposed pressure sensor. Optimization results are discussed and the sensor performance based on the optimal design is presented. Finally, the effect of the various variables in genetic algorithm on optimization process is also discussed.

5.2 Basic theory of genetic algorithm

Genetic algorithm is an evolutionary optimization method used to solve possible optimization problems. The genetic algorithm is modelled roughly on how natural biological systems evolve and adapt through the process of natural selection [75]. A possible solution to a particular optimization problem can be viewed as an individual, consisted of a finite set of parameters. The genetic algorithm uses a population of individuals to perform the search. The characteristics of an individual, so called chromosome, encodes one set of decision variables and so results in a single point in the solution space.

In the evolutionary process of genetic algorithm, a repetitive loop or a series of generations are used in order to evolve a population of individuals to find the fittest individual. The fitness of each individual is determined by a given fitness function that evaluates the level of aptitude that a particular individual has to achieve the optimization objective. Each generation in the evolutionary process produces a new population of individuals through genetic operations: Crossover and Mutation, which are governed by the crossover rate and the mutation rate respectively.

- Crossover is a genetic operator used to swap genetic information between the parent individuals, and it is an analogy to reproduction and biological mating.

- Mutation is a genetic operator used to introduce genetic modification in the parent individuals, and by this means genetic diversity is maintained form one generation to the next. It is analogous to biological mutation.

These operators produce a new generation of individuals with the intension to achieve better overall fitness in the population of individuals. New generations of individuals are produced containing, on average, more good chromosomes than individuals in a previous generation, i.e., each successive generation will contain more good candidate solutions than previous generations. Eventually, once the population has converged such that there is no noticeably difference in the population of consequent generations, the algorithm itself is said to have converged to a set of solutions to the problem.

5.3 Multi-objective genetic algorithm

The sensor design problem involve the simultaneously optimization of two objectives at once, the touch pressure P_t and the sensitivity S. Therefore, the optimal design is a multi-objective problem, where it is not always possible to reach an optimal solution with respect to all of the objectives evaluated individually [76][77]. In regards to evolutionary computation, Shaffer proposed the first implementation method for a multi objective evolutionary search [78]. The proposed method solves multi-objective problems by a linear combination of the objectives. In this way, a single objective function may be created or the objectives may be converted into restrictions imposed on the optimization problem.

Other methods propose a fitness function for each individual in a current population during an evolutionary search, based upon the concepts of dominance and non-dominance of optimality[79][65]. The optimization of multi-objective functions seldom admits a single perfect solution, but rather a set of alternative solutions, which is called a Pareto set [80][81]. The solutions in the Pareto set are optimal in a wider sense that no other solutions in the search space are superior to them. The main goal of multi-objectives optimization is to find one or multiple solutions

in the Pareto set.

A Matlab toolbox of multi-objective evolutionary algorithm (MOEA) based on these concepts has been developed [82][83][84]. This toolbox is employed to handle the sensor parameters optimization and the analytical model can also be easily incorporated into it under Matlab programming environment. The objective of the optimization problem is to find a parameter set which can achieve highest sensitivity in the touch-mode working range, from 9.5 to 10.0MPa.

5.3.1 Data structure of candidate individuals

For the sensor structure shown in Figure. 2.15, the geometrical parameters that govern the C-P relationship are:

- a - Side length of diaphragms;
- b - Half length of the post;
- d - Half length of the boss ring in the sensing diaphragm;
- g - Initial gap between the boss ring and the middle diaphragm;
- η - Initial gap between middle plate and the substrate, defined by SiO_2 layer thickness;
- h_{top} - Top plate thickness;
- h_{mid} - Middle plate thickness

As discussed in Chapter 3, both surface micromachining and bulk machining are employed to fabricate the pressure sensor. The cantilever middle diaphragm is fabricated by SiO_2 sacrificial etching after a polysilicon PECVD deposition. The top diaphragm is formed by the silicon handle layer of a SOI wafer. The whole device is formed by anodic bonding these two parts. Diaphragm thicknesses are restricted by fabrication processes and varying them requires to change process conditions, which may lead to problems including more internal stress, surface defects and diaphragm warpage. Thus, according to the rule of standard fabrication

process, the middle plate thickness is set as $h_{mid} = 1.50\mu m$, while the top plate thickness is $h_{sen} = 20\mu m$, which is within the standard oxide thickness range of SOI wafers. The initial gap between middle plate and substrate, which is defined by the removed SiO_2 layer, is set to $\eta = 1.0\mu m$.

Data structure of candidate individuals are formed by adjusting the parameters: $\lambda = [a, g, b, d]$. Instead of using binary values, the data of each candidate solution is represented in real number. The MOEA toolbox deals with a real coded population directly, and devises the crossover and mutation in the real number space. There are some advantages of using direct real parameter GA:

1. The real parameter need not be converted from decimal to binary every single time.

2. With the use of real parameters, there will be increased precision as there will be no loss in resolution during binary bit coding.

3. Real number crossover and mutation schemes can be applied to search the solution space.

5.3.2 Search space

From Figure. 2.15, it can be seen that the size of boss ring, d must be larger than the size of post, b, so as to make the cantilever plate deflect. In practice, the precision of mask alignment achieved is about $2 \sim 3\mu m$ [85] and the misalignment errors increase during processes such as wet etching, bonding [86]. Therefore, to avoid the interference between post and boss ring, the lower bound of d should be at least $10\mu m$ larger than the upper bound of b.

Assuming that the device is fabricated by combining a SOI wafer with a cantilever member with a pyrex wafer via anodic bonding, the gap between the top and middle plate is constrained by the anodic bonding process. During anodic bonding, the thin middle plate may be pulled up by electrostatic force. This probability of this undesirable outcome may be minimized by laying a metal layer on the middle plate and applying the same voltage to it as the silicon substrate so

no electrostatic forces act on these areas. By using this technique, the achievable gap between the top and middle plate is between $2\mu m$ and $10\mu m$, as discussed in section 3.1. According to design and fabrication constraints, the search space Λ in the GA optimization is defined as:

- Diaphragm Sizes, $a \in [300, 900]\mu m$;
- Gap between diaphragms: $g \in [2, 10]\mu m$;
- Half length of the post, $b \in [10, 20]\mu m$;
- Half length of the boss ring, $d \in [30, 80]\mu m$;

5.3.3 Fitness functions

The multi-objective optimization problem can be expressed as minimization of $f(\lambda) = \{f_1(\lambda), f_2(\lambda)...\}$, where $\lambda \in \Lambda$. In the sensor optimal design, two fitness functions are considered.

The first fitness function $f_1(\lambda)$ is the reciprocal of the sensitivity, which is computed by using the analytical model discussed in Chapter 4. Since the objective is to maximize the sensitivity, the lower value of the $f_1(\lambda)$, the fitter of λ. Therefore, following fitness function is employed:

$$f_1(\lambda) = \frac{1}{S_{ANA}} \tag{5.1}$$

Where S_{ANA} is the sensitivity obtained from the analytical model.

The second fitness function $f_2(\lambda)$ is the performance index that evaluate the sensor touch point pressure P_t. Since the objective is to make the designed P_t close to required touch point P_{t0}, the function can be defined as:

$$f_2(\lambda) = |P_t(\lambda) - P_{t0}| \tag{5.2}$$

5.3.4 Evolution conditions

Each population consists of a certain number of individuals. The initial population is generated randomly for each evolution run. Two points uniform crossover

operator is used, where common genes of the parents are retained in the child and non-common genes are selected with equal probability from their parent. After crossover breeding, the best solutions from among the parents and the new child are retained to form the next generation. Mutation is then conducted by cutting an inferior solution from the population. Figure. 3.12. The best solution in the population is never used for mutation to ensure that the optimal solution is always been kept during the evolution.

5.4 Optimization results

In solving the geometric optimization problem, the object is not limited to get the largest sensitivity, but also the closest touch point pressure to desired one. The two criteria are often competing with each other. Figure. 5.1 shows the evolution progress of Pareto front. The various Pareto fronts obtained at the initial generation, the intermediate generations and the final generation are plotted in Figure. 5.1 with different markers. It can be seen that there is only a small number of non-dominated solutions appear in the initial generations, which also congregated in a small portion of the solution space. However, as the evolution proceeds, the diversity of the population increases significantly and the non-dominated solutions gradually evolve towards the final trade-off curve. A solid line connecting all the final solutions forms the Pareto set, which clearly shows the final trade-off by the MOEA.

The population used in the genetic search is initialized with 10 total individuals that are generated randomly. In each generation, new members are produced by gene exchange using crossover operator (0.7 crossover probability and 2 crossover points) and the classic mutation method with a mutation probability of 0.01. The fitness values of each individuals are computed in regards to minimizing the fitness function $f(\lambda) = \{f_1(\lambda), f_2(\lambda)\}$.

The GA evolution progress is shown in Figure. 5.2. Both the best fitness value $f(\lambda)$ (Solid line) and the average fitness value (Dash line) decrease abruptly within the first 10 generations. The best fitness value of $f(\lambda)$ drops continually until it

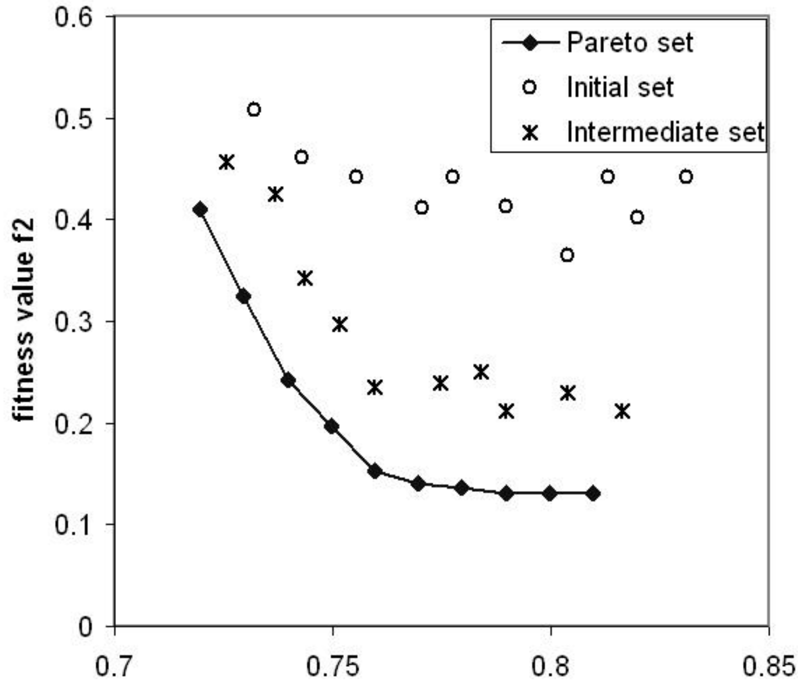

Figure 5.1. The evolution of Pareto front for the multi objective optimization

converges to 0.6121 after 40 generations. From Figure. 5.1, one of the solutions in the Pareto set has been studied, and it has a smallest $f(\lambda)$ value. The fitness values of the solution in the Pareto set, $f(\lambda)$, $f_1(\lambda)$ and $f_2(\lambda)$, are shown in Table 5.1.

After the group evolution stopped at maximum 100 generations, the best solution is obtained as $\lambda_o = [a, g, b, d] = [680.2301, 5.8612, 13.1282, 50.0402]$, which has a lowest fitness value of $f(\lambda_o) = 0.6121$. Thus, the highest sensitivity from this solution is $1/f_1(\lambda_o) = 1/0.8096 = 1.2351(fF/kPa)$, with the touch point pressure $P_t = 9.867MPa$. The capacitance-pressure characteristics of the pressure sensor with optimal parameters estimated by genetic algorithm is shown in Figure. 5.3.

Figure. 5.3 also present the capacitance-pressure characteristics of the parameter set generated by the graphical design method in Chapter 3, where $\lambda_{de} = [a, g, b, d] = [500.0, 6.0, 12, 42]$. The sensor performance designed from two methods are compared in Table. 5.2. It can be seen that the optimal design by GA gives larger expected sensitivity and a touch point closer to $10MPa$ than graphical design. That is because the graphical design is based on typical parameter curves

Generation	Best $f(\lambda)$	Best $f_1(\lambda)$	Best $f_2(\lambda)$	Average $f(\lambda)$
1	0.9348	1.4301	0.4421	1.7432
5	0.6482	0.9723	0.4011	0.7255
10	0.6477	0.9436	0.3823	0.7201
15	0.6478	0.9553	0.3621	0.6577
20	0.6467	0.8965	0.3242	0.6545
25	0.6437	0.8942	0.2012	0.6647
30	0.6429	0.8837	0.1728	0.6546
40	0.6151	0.8102	0.1323	0.6297
50	0.6121	0.8096	0.1301	0.6121
100	0.6121	0.8096	0.1301	0.6121

Table 5.1. Evolution of fitness values, population=10, crossover probability=0.7, mutation probability=0.01

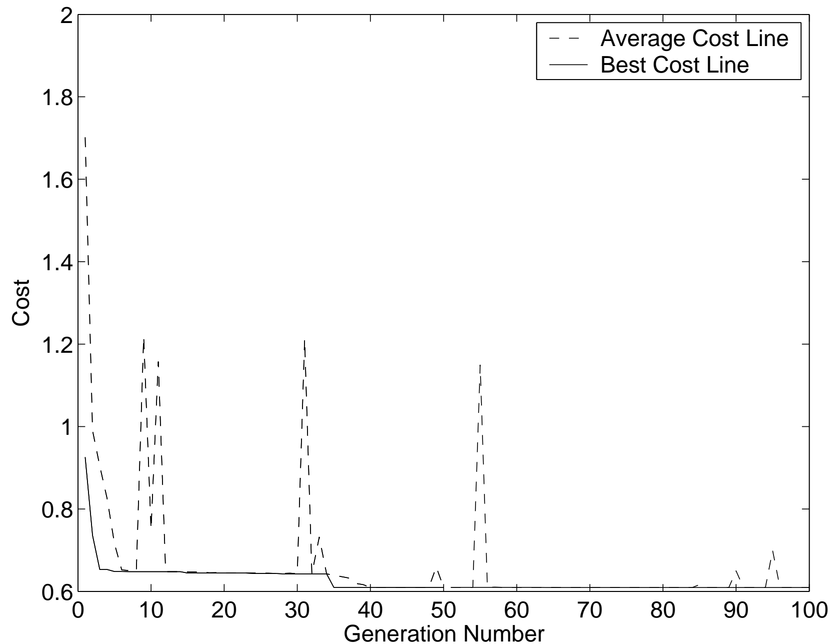

Figure 5.2. Cost value curves in the MOEA evolution, population size 10

and the parameters cannot be varied simultaneously, while the GA optimal design can evaluate parameter sets over the whole search space.

In searching the optimal parameter sets, the genetic algorithm design use ran-

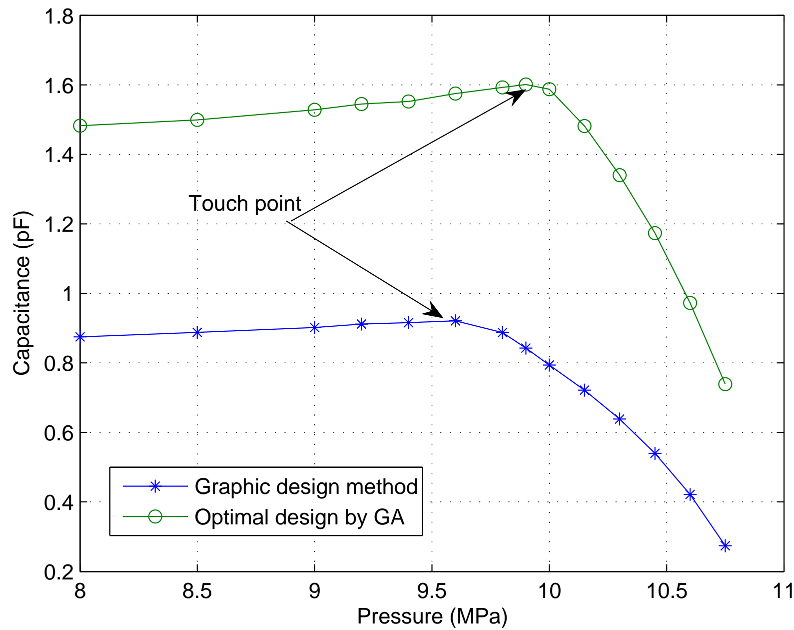

Figure 5.3. The capacitance-pressure characteristics of the designed sensors

	Nominal capacitance (pF)	Touch point (MPa)	Sensitivity (fF/kPa)
Graphical design	0.7995	9.530	0.7448
GA optimal design	1.3550	9.867	1.2351

Table 5.2. Comparison of sensor performances between graphical design and GA optimal design

dom processes to transition from one search state to another. The random processes give the sensor design a good balance between wide exploration of the search space and exploration of local fitness functions. The variables of genetic algorithm such as population size, crossover probability may affect GA evolutional processes, thus should be discussed and chosen properly.

5.5 Effect of GA varaibles

5.5.1 Population size

The population size of candidate solutions is one of the factor that affect GA evolution. In the study, the population size is increased from 10 to 20, and 30. When the population is 20, the GA evolution process needs 1341 seconds, compared to 412 seconds when population is 10. The evolution results are shown in Fig. 5.2. After the group evolution, best solution is obtained as $\lambda_o = [674.5103, 5.8911, 13.2696, 50.513]$, which has a lowest fitness of $f(\lambda) = 0.5957$. Thus the sensitivity from this solution is $1.2465 fF/kPa$.

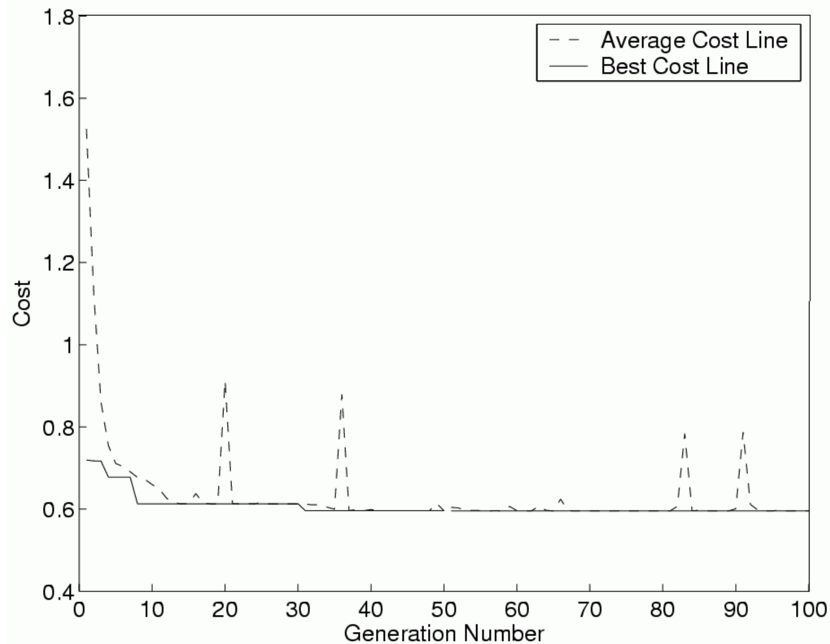

Figure 5.4. Cost value curves in the MOEA evolution, population size 20

The group size is further increased to 30, the GA evolution procedure needs 5623 seconds. When the evolution process is terminated at generation 100, the best pattern obtained is $\lambda_{op} = [672.3827, 5.9012, 13.6734, 50.6723]$, which has a lowest fitness of 0.5956. The sensitivity of $1.2473 fF/kPa$ can be achieved by adopting this solution.

The comparison of sensor optimal design for different population sizes is shown in Table 5.3. It can be seen that large population size needs much more time to

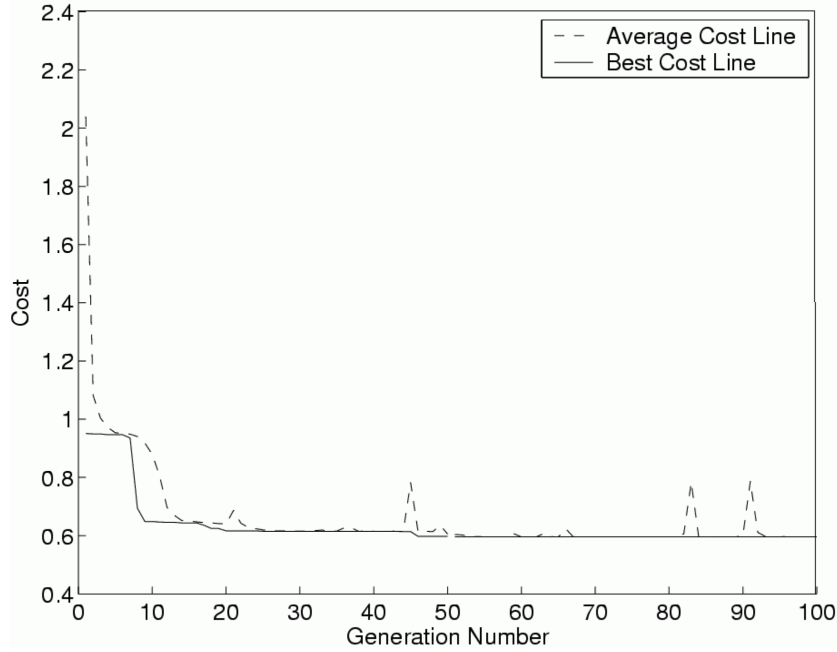

Figure 5.5. Cost value curves in the MOEA evolution, population size 30

	Population = 10	Population = 20	Population = 30
Evolution time (seconds)	412	1341	5623
Best fitness $f(\lambda)$	0.6121	0.5957	0.5956
Sensitivity (fF/kPa)	1.2351	1.2465	1.2473
Touch point (MPa)	9.867	9.873	9.923

Table 5.3. Effect of population size on GA evolution

evolve. Although the computation speed of a small population size is faster, it may stop at some local optimal points. For larger population, the number of generations to convergence increases with some increase in accuracy. That is because that the larger the population size, the greater chance that the initial state of the population will contain a pattern close to the global optimal solution.

In the optimization procedure, the evolution curve may not always converges to the same value. Several rounds of evolution are performed to determine the influence of population size on modelling errors. The following conditions are used in the study:

- crossover = 0.7;

- mutation probability = 0.01;
- evolution step = 100;

For each different population size, GA evolutions are performed 10 times with initial individuals chosen randomly. When population size is 10, the lowest fitness value of the evolutions is 0.6121, and the highest result value is 0.6987, as shown in Figure. 5.6. As the population size increases to 20, the lowest value slightly decreases to 0.5957, while the highest cost drops greatly to 0.6593. It can be seen

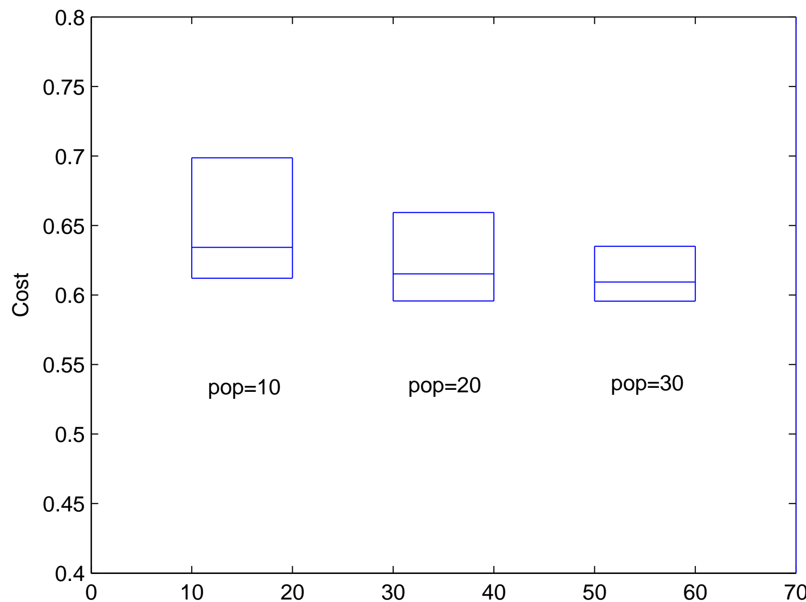

Figure 5.6. Deviation of 10 runs in different population size, crossover = 0.7

that larger population size will help to minimize the deviation of GA results. Too small a population size, for example, the population size of 10, may make the group of individuals converge to a suboptimal solution too early and result in a high fitness value. On the other hand, a large population size can overcome these local optimal points but requires longer computation time.

5.5.2 Crossover probability

The genetic operation of crossover allows the creation of new individuals which accounts for the generation of new parameters in the search space. The crossover probability is an important factor in GA optimization and it represents the chances of two parent individuals selected from the population on basis of their fitness. A crossover probability of 1 means that all children in the new generation are generated by crossover operation, while a crossover probability of 0 means that all children are mutation children.

Figure. 5.7 and Figure. 5.8 show the evolution process under different crossover probabilities. From Figure. 5.7, it can be seen that large crossover probability, such as 0.8, may lead to more inclinations to keep the genetic patterns of parent individuals, thus slowing down the process of finding new genetic patterns. Moreover, there are larger fluctuations in the evolution curves of average fitness in both figures, compared to Figure. 5.2. Therefore, neither high nor low of crossover probability is an effective strategy for optimizing the design problem.

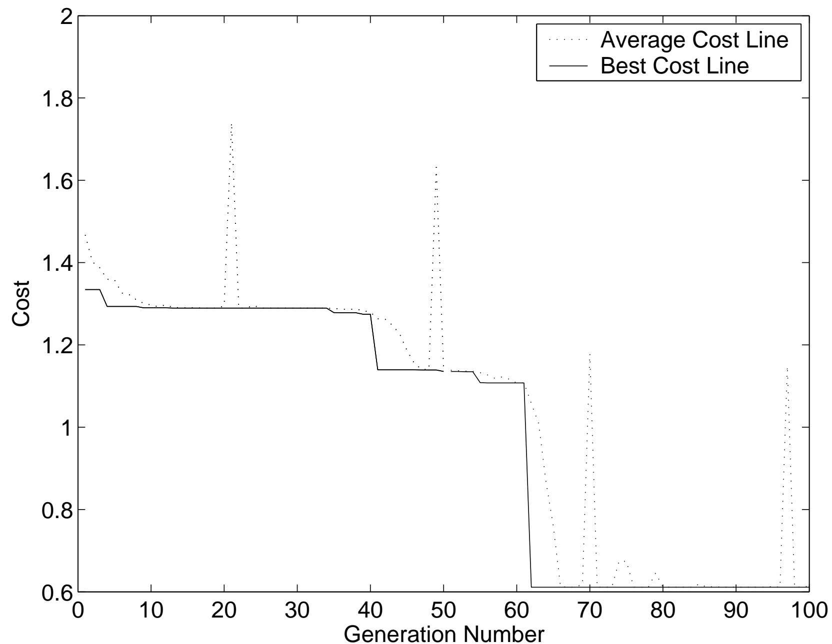

Figure 5.7. GA evolution at crossover probability 0.8, population 10

Figure. 5.9 shows the deviation of evolution results in different crossover prob-

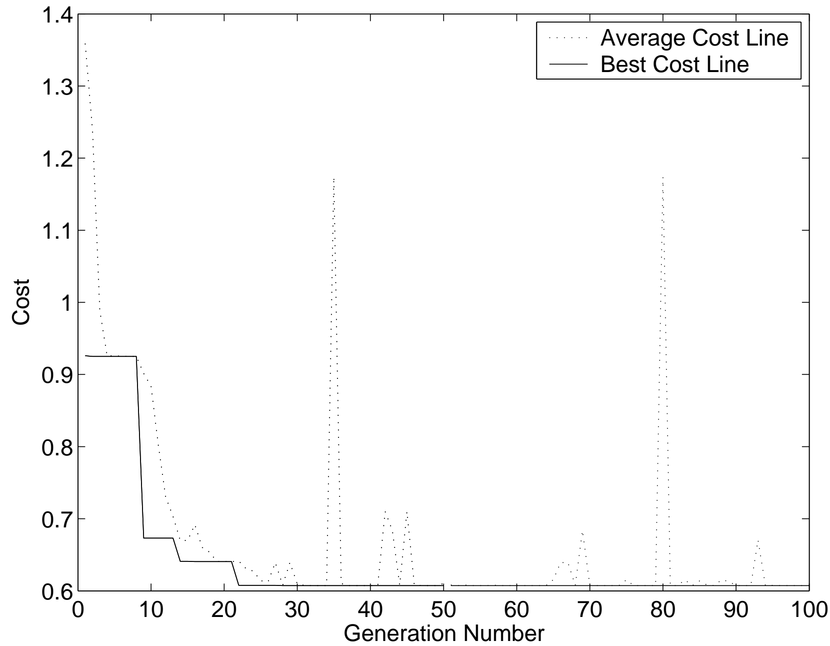

Figure 5.8. GA evolution at crossover probability 0.6, population 10

abilities. Each cases have the same lowest fitness value of 0.5960. For crossover probabilities of 0.6 and 0.8, the highest fitness value is 0.6818 and 0.6918, respectively. For crossover probability of 0.7, the highest fitness value is 0.6593. Thus, proper choice of crossover probability value may help to reduce the deviation of evolution results.

5.6 Conclusions

This chapter proposed an optimal sensor design method using genetic algorithm. Multi Objective Evolution Algorithm (MOEA) has been utilized to solve the optimal design problem of the pressure sensor, with two major objectives, including touch point pressure P_t and sensitivity S in the working range. The algorithm uses the selection, crossover recombination, and mutation operators on the population of individuals to perform the search. The evolution process gradually converges to a static point, regardless of the individual values randomly created at the start of the search.

The optimal design method using genetic algorithm has some powerful advan-

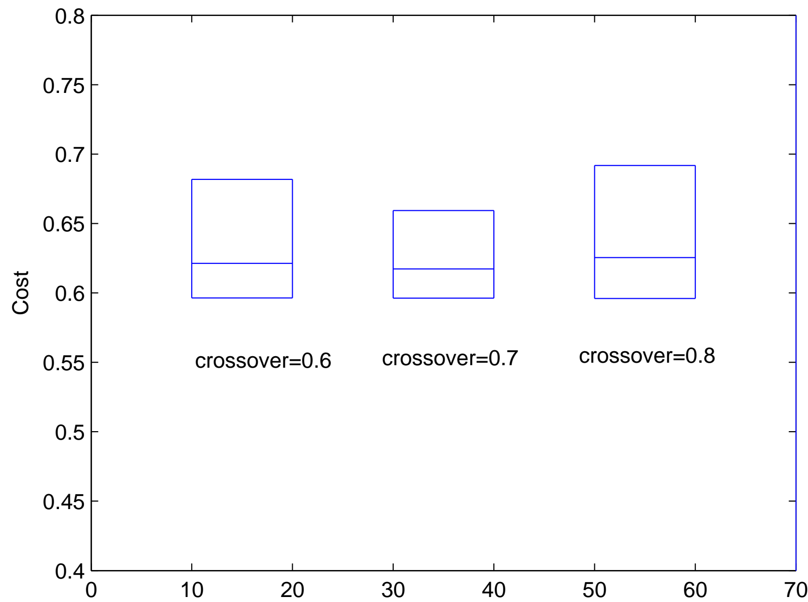

Figure 5.9. Deviation of 10 runs in different crossover probabilities, population 20

tages over the graphical method discussed previously. It provides the means of varying parameters continuously and simultaneously in the solution space. The result of GA optimization shows that the device sensitivity after touch point pressure $9.86MPa$ can be high as $1.2351fF/kPa$. Compared to the sensitivity of $0.7448fF/kPa$ obtained by the graphical method in Chapter 3, 65.8% improvement in sensitivity can be achieved by using GA methods.

Genetic algorithm variables, such as population size and crossover probability, may affect the evolution process. Large population size can help to avoid the problem that the fitness function may get stuck at local minimum points, at the expense of more evolution time. The evolution results also shows that impropriate crossover probability may not reach a convergence point effectively. Meanwhile, since the genetic algorithm uses random processes to transition from one generation to the next, it is unlikely to obtain the same answer in any two attempts with the same problem. The deviations of the GA evolution results under different conditions are also discussed.

Chapter 6

Sensor Fabrication and Testing

6.1 Introduction

The design and optimization of the capacitive pressure sensor with two deformable diaphragms has been discussed in Chapter 5. In micro device manufacturing process, the realization of a design by fabrication can be as important as the design process itself. The purpose of this chapter is to describe the fabrication sequence and masking layers.

Fabrication steps are discussed with the help of schematic drawings. As designed and simulated in previous chapters, diaphragm sizes are on the order of hundreds of microns, whereas film thickness are several microns. Schematic cross sections of processing steps are therefore, not drawn to scale, as the aspect ratio of height to width are rather small in the real device. In additional, step coverage for most films is presumed to be conformal and the perfect conformal corner would be a 90° arc with radius of the film thickness. However, in this chapter all the corner are drawn as right angles, as shown in Figure. 6.1.

The chapter starts by introducing the fabrication process flow, including the fabrication steps on a glass wafer, a silicon SOI wafer and wafer bonding. Subsequently, the details of the fabrication processes are presented, such as glass etching, chemical vapor deposition, metallization and anodic bonding, etc. For each process, the process equipments, conditions, experimental results as well as the problems

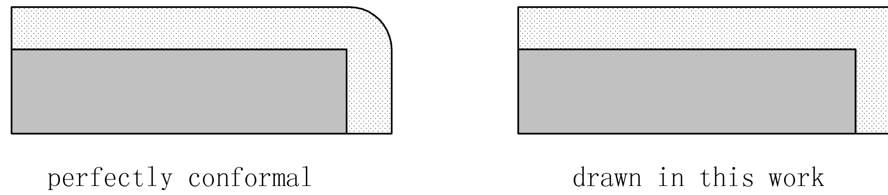

Figure 6.1. Step height coverage. (a) perfect conformal coverage (b) step coverage as drawn in this work

are discussed. Then, a specialized testing system for the pressure sensor is presented. The measurement results from LCR meter is presented, and compared with computer simulation results. The capacitance change was also converted to voltage output by using the measurement board MS3110. Finally, conclusions are drawn based on the fabrication and measurement results.

6.2 Fabrication Flow

In this section, the process flow of the fabrication steps and cross sections for each typical fabrication steps are described in a comprehensive way. Fabrication techniques, materials and conditions are discussed briefly in each steps.

Both bulk micromachining and surface micromachining technology are used to form the proposed capacitive pressure sensor with two deformable diaphragms. The sensing diaphragm of the pressure sensor is formed by deep RIE etching on a SOI wafer, with the intermediate oxide layer acting as the etch stop. The middle cantilever diaphragm is formed by surface micromachining that remove the sacrificial silicon dioxide layer. A Pyrex glass wafer after patterned with the boss ring is then anodically bonded to the SOI wafer to complete the sensor structure.

Both SOI and glass wafer are 4 inch wafers. The glass wafer used is the Corning #7740 Pyrex wafer with $500 \pm 25\mu m$ thick. The specifications of the SOI wafers in the fabrication is shown in Table 6.2.

Photo resist is a radiation sensitive material that is rendered soluble in a developer when it is exposed to radiation. There are two types of photo resist (PR) materials are used during the fabrication processes, namely AZ-9260 and AZ-7220.

	Main Fabrication Steps	Remarks
Glass Wafer	1. glass etching by HF based solution	the cavity of the sensor
	2. second HF based glass etching	the boss ring
	3. metal Cr/Au sputtering	electrode and lead
SOI Wafer	4. nitride deposition	dielectric layer
	5. metallization	electrode and lead
	6. SO_2 deposition and patterning	space for cantilever
	7. polysilicon deposition	cantilever middle diaphragm
	8. sacrificial etching	cantilever middle diaphragm
Glass + SOI	9. wafer bonding	seal the cavity
	10. backside silicon etching	sensing diaphragm

Table 6.1. Run sheet of major fabrication processes

Thick PR AZ-9260 is for large pattern lithography. Thin PR AZ-7220 is for small pattern lithography where critical dimension can be below $2-3\mu m$. The details of both PR types are in Appendix B.

	SOI wafer
Diameter	4 inches
Orientation	[1 0 0]
Device thickness	$5.0 \pm 0.5\mu m$
Handle thickness	$395 \pm 5\mu m$
Oxide thickness	$2\mu m$

Table 6.2. Specifications of SOI wafer

6.2.1 Glass wafer fabrication steps

In summary, the fabrication steps on glass wafer start with the first glass wet etching to form the cavity of the pressure sensor. Subsequently, the boss ring structure is created by the second glass etching. Metal layer is sputtered to form the capacitor electrode and electrical leads. Detailed steps will now be presented.

After the glass wafer is cleaned in a wet bench, a $10\mu m$ thick PR AZ-9260 for large pattern lithography is spin-coated and patterned, as shown in Figure. 6.2(a). In Figure. 6.2(b), a cavity of $10.0\mu m$ is formed after wet etching by use of a HF based solution. The photo resist (PR) layer is removed by immersing the wafer into Acetone after glass etching and the glass wafer after first etching step is shown in Figure. 6.2(c). The cavity in the glass wafer will be used as the chamber of the pressure sensor.

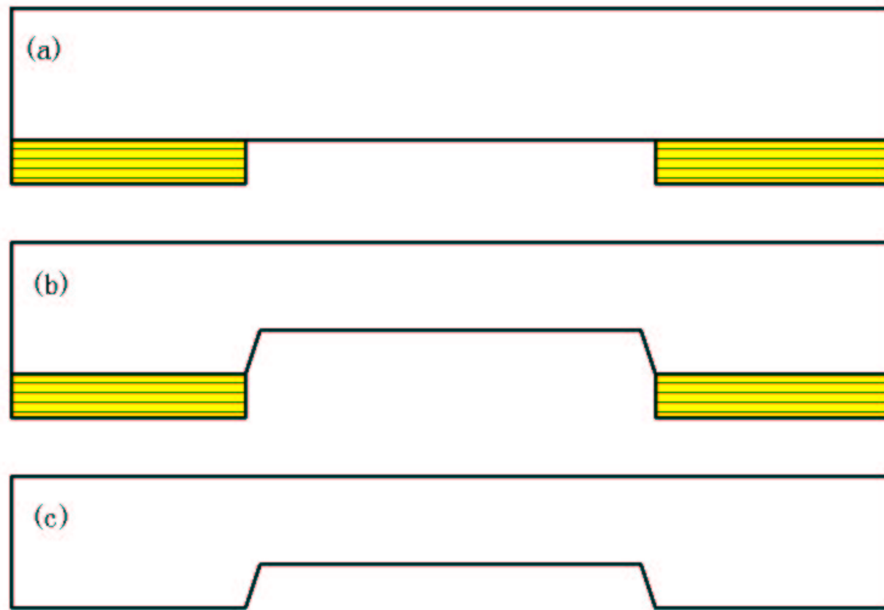

Figure 6.2. Glass 1st etching step. (a)Spin coat and pattern PR (b)Glass etching (c)PR striping

Another similar glass etching step is performed afterwards to construct the boss ring, as shown in Figure. 6.3. The boss ring acts as the stopper that force the cantilever diaphragm bend. After growing and patterning the thin PR layer AZ-7220, a HF wet etching is utilized to make a protrudent ring with a height of $2.0\mu m$.

In Figure. 6.4(a), the glass wafer is coated by a positive thick AZ-9260 PR, and the PR layer is patterned. Figure. 6.4(b) shows that a layer of 20 nm of chromium (Cr) and 200 nm of gold (Au) is formed by E-beam evaporation. The PR layer is lifted off by the material Shipley 1827 and the remaining Cr/Au layer form the

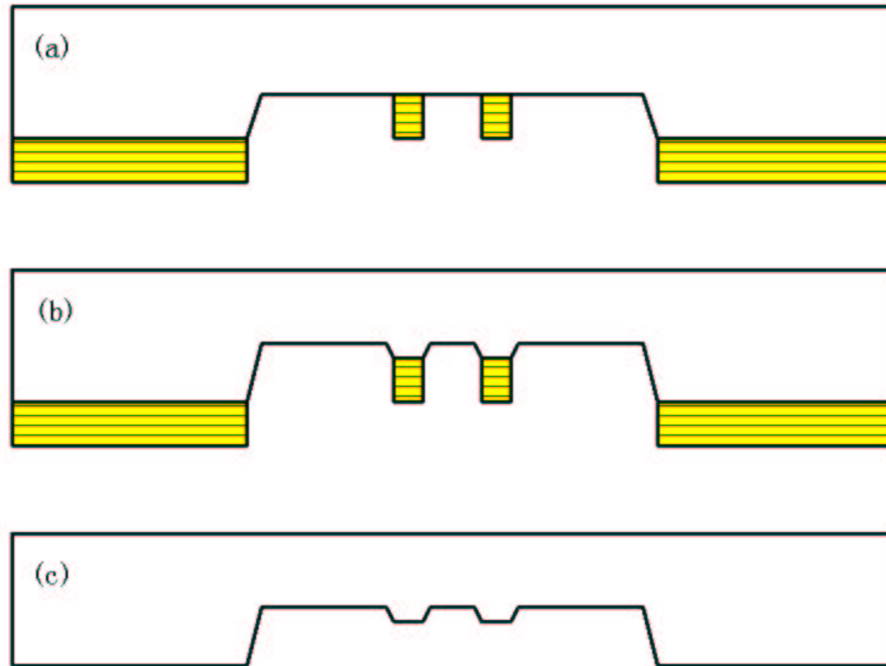

Figure 6.3. Glass 2nd etching step. (a)Spin coat and pattern PR (b)Glass etching (c)PR striping

capacitor electrode and the electrical connection path, as shown in Figure. 6.5(c). In Figure. 6.5(d), glass milling is performed to define the area of bond pads, at which region a $120 \sim 160 \mu m$ deep cavity is formed.

6.2.2 SOI wafer fabrication steps

The fabrication procedure on the SOI wafer includes the formation of passivation nitride layer, a metal layer and the freestanding cantilever structure layer by sacrificial etching. Firstly, a 400 nm thick nitride layer is coated on the device side of the SOI wafer by Low Pressure Chemical Plasma Deposition (LPCVD), as shown in Figure. 6.5(a). Silicon nitride acts as a passivation layer due to its extremely useful dielectric property. Si_3N_4 is deposited at moderately high temperatures (800^oC) and low pressure (250 mtorr), using dichlorosilane ($SiCl_2H_2$) and ammonia (NH_3). The deposition rate is roughly about 30A/min for 4 inch wafers by using the low stress nitride recipe LSN 850.

In Figure. 6.5(b), the SOI wafer is coated by a thick AZ-9260 PR layer, and

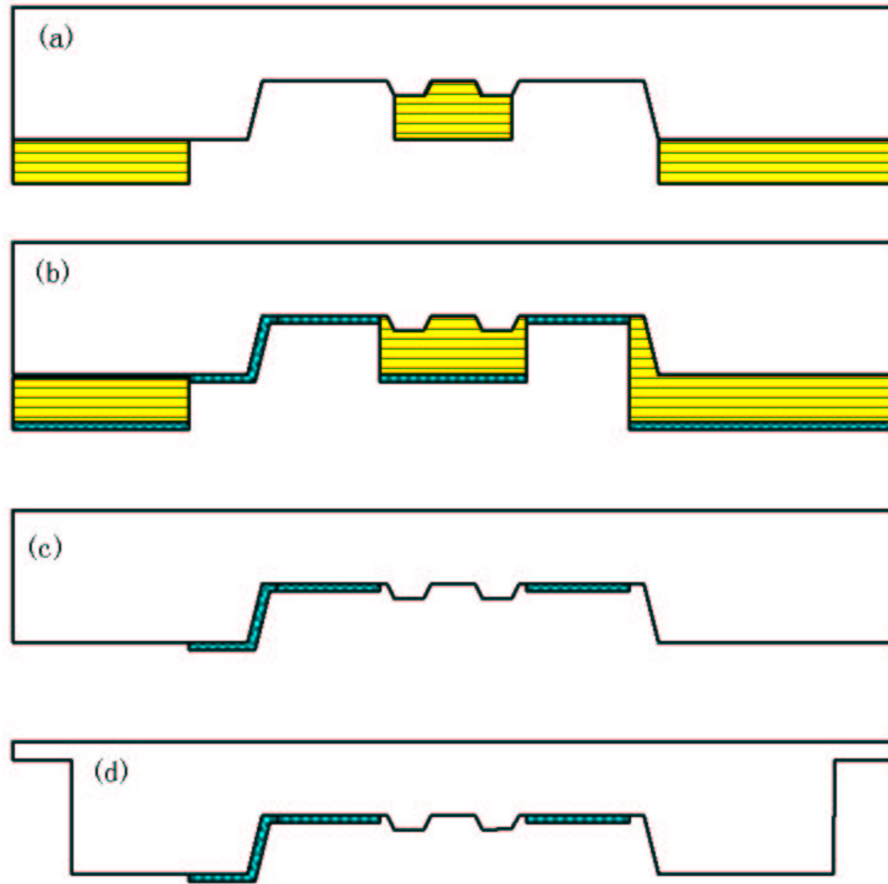

Figure 6.4. Metal sputtering on the glass wafer. (a)Pattern PR (b)Sputter Cr/Au (c)PR lift off (d)glass milling

the PR layer is patterned by the lithography procedure. Then, a layer of Au/Cr is formed by E-beam evaporation. The PR layer is lift off by the material Shipley 1827 and the Cr/Au layer remains at the region without the PR layer, as shown in Figure. 6.5(c).

A 2.0 μm thick silicon oxide layer is formed by Plasma Enhanced Chemical Vapor Deposition (PECVD) at a low temperature of 100^oC, as shown in Figure 6.6(a). Since after the Cr/Au deposition, the temperature has to be kept below 400^oC, PECVD oxide is the material of choice at this step and its property rival the regular LPCVD oxide. After the thin PR layer AZ-7220 is grown and patterned in Figure 6.6(b), silicon dioxide is etched by Reactive Ion Etching (RIE) in a CHF_3/O_2 plasma ambient. The chamber pressure is $30mTorr$ and DC self-bias is $470V$.

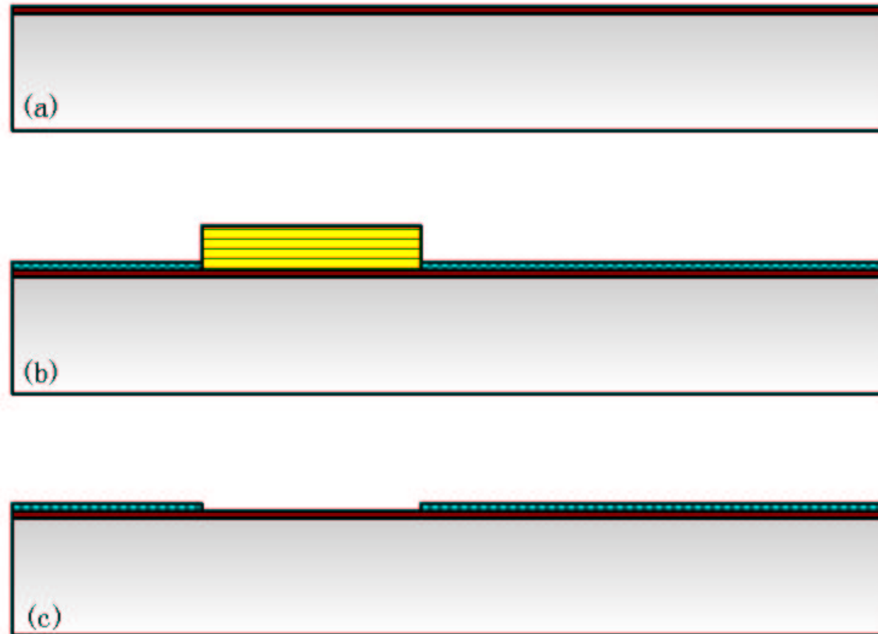

Figure 6.5. Dielectric layer and Lead formation on a SOI wafer. (a) LPCVD silicon nitride (b) Spin coat and pattern PR (c) Metallization

Figure 6.6(c) shows the pattern region of oxide layer is left after removing PR layer.

Figure 6.7(a) shows a 1.5μm thick polysilicon layer that is grown by PECVD. The deposition is performed at a substrate temperature of 194^oC and a chamber pressure of 1.5$mTorr$ from Hydrogen (H_2) and silane (SiH_4) plasma. As shown in Figure 6.7(b), the thin PR layer AZ-7220 is then spin-coated and patterned. Subsequently, the PECVD polysilicon layer is patterned by fluorine based plasma etching process using Freons/SF_6 , followed by PR strip. The resulting structure is shown in Figure 6.7(c). The silicon dioxide is removed by sacrificial etching by use of Hydrofluoric acid (HF), and the cantilever polysilicon structure is left, as shown in Figure 6.7(d).

6.2.3 Wafer bonding and backside etching

The sensor device is then formed by connecting the glass wafer to the SOI wafer by means of anodic bonding technology, as shown in Figure. 6.8(a). Anodic bonding

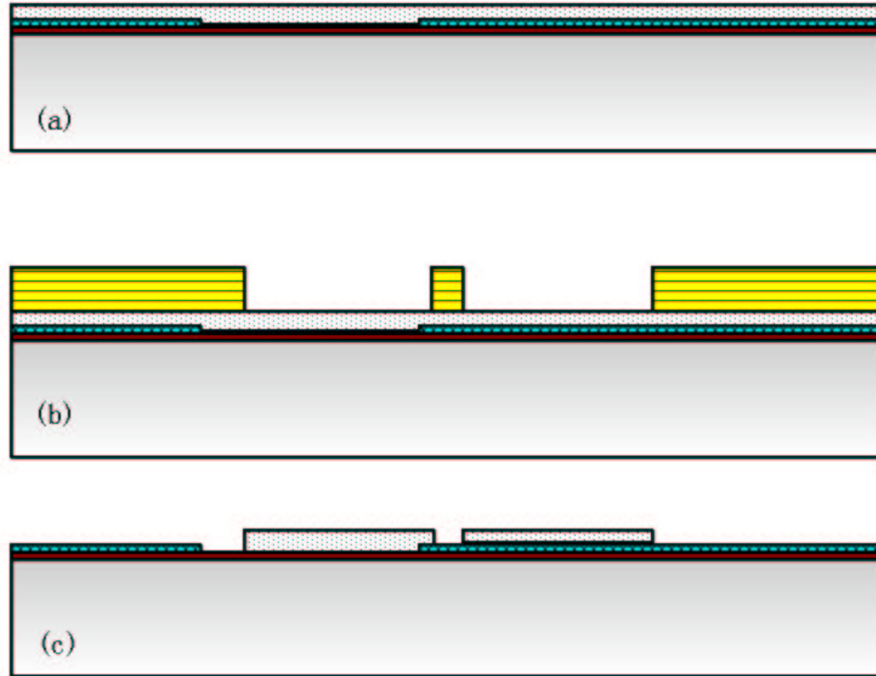

Figure 6.6. Silicon oxide deposition and patterning. (a) PECVD oxide (b) PR patterning (c) oxide RIE etching

was performed in an SB-6 Substrate Bonder (Suss) at 300^oC with a bonding bias of 800 V applied for five minutes. The next step is glass grinding that reduce the glass wafer thickness to $100 \pm 120\mu m$. After the grinding, the bond pads are exposed so that a probe station can be used to connect the device to external circuits during the test and characterization phrases, as shown in Figure. 6.8(b).

In Figure. 6.9(a), a $10\mu m$ thick PR layer AZ-9260 is spin-coated and patterned on the backside of SOI wafer. The optical manual back-side aligner, the OAI Model 800, is employed to pattern the PR, with respect to the structure locations on the frontside wafer. Subsequently, silicon deep RIE etching is performed in the Unaxis VLR 700 Bosch Chamber, with an etching temperature of 25^oC. The depth removed by etch process is $400\mu m$ with a etch rate $2\mu m/min$ and the high selectivity of Si dioxide: Si (150:1) enable the etching process to stop at the intermediate oxide layer of the SOI wafer. The completed sensor device after back side etching is shown in Figure. 6.9(b).

The process flow given above shows the general steps that used to fabricate the

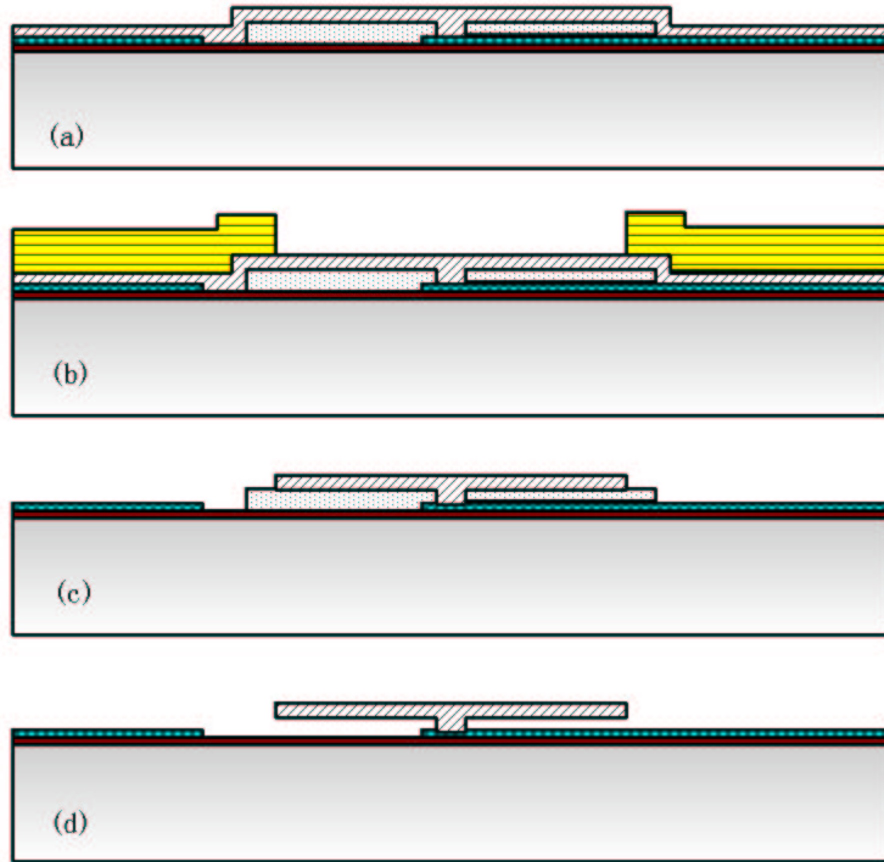

Figure 6.7. Polysilicon deposition and patterning, followed by sacrificial etching. (a) PECVD polysilicon (b) PR patterning (c) polysilicon plasma etching (c) sacrificial etching

pressure sensor. More detailed discussions of fabrication practice are presented in the following sections.

6.3 Fabrication results

In the fabrication, the following sensor dimensions are aimed to achieve:

- Initial gap height $g = 6.0\mu m$;
- Sensing plate thickness $h_{sen} = 5.0\mu m$;
- Middle plate polysilicon thickness $h_{mid} = 1.50\mu m$;

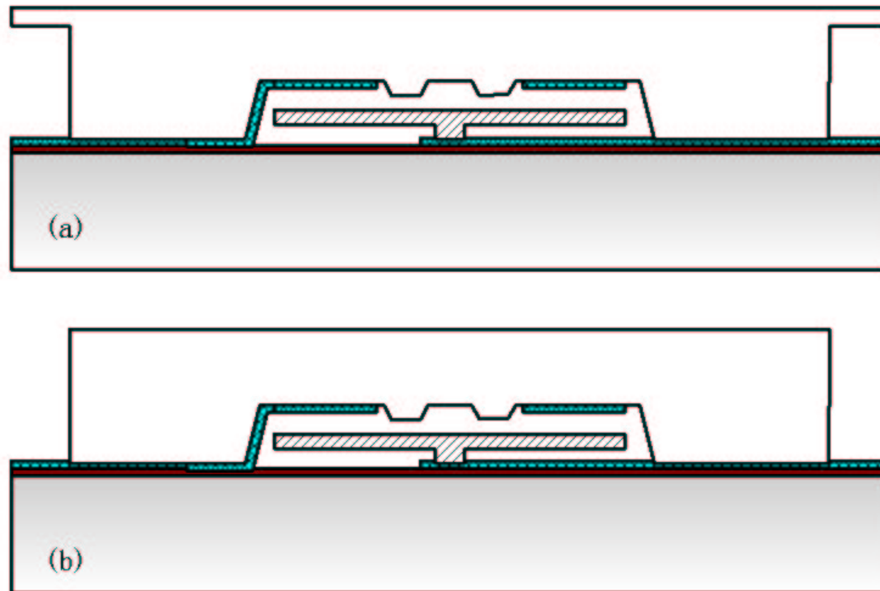

Figure 6.8. Wafer bonding. (a)anodic bonding (b)glass grinding

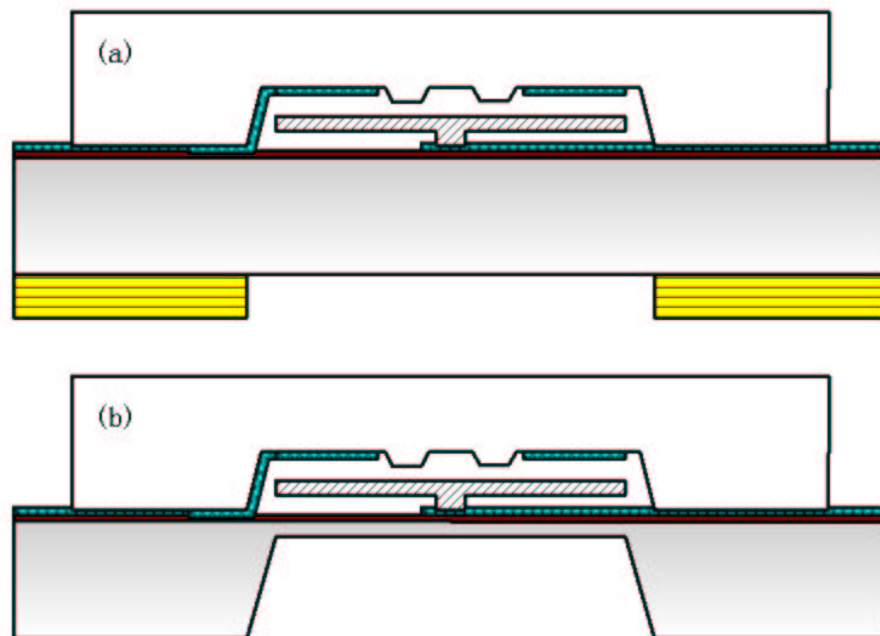

Figure 6.9. Backside etching (a)PR patterning (b)Deep RIE

- Gap between middle plate and substrate, or oxide thickness, $g_o = 2.0\mu m$
- Insulating nitride layer thickness $h_{nitride} = 400nm$
- Side length of both diaphragms $a = 500, 600, 670, 700\mu m$;

- Half length of the post $b = 13.0\mu m$;

- Half length of the boss ring $d = 50\mu m$.

6.3.1 Glass etching

Beside silicon wafers, various types of glass wafers are widely used in micro sensor and micro actuator technologies. The type of glass used in the field of microsystem technology must be microstructurable, preferably using a standard lithography process [87]. Moreover, glass contains easily movable ions to perform anodic bonding [88]. The glass wafer used for fabrication is the Corning Pyrex 7740 wafer with double side polished, which are commonly used for anodic bonding in micro system technology. The wafers also have a thermal expansion coefficient matching that of silicon so as to avoid thermal stress.

There are some issues need to be considered during the glass etching process. The cavity that needs to be etched is relatively deep. However, the etching time cannot be too long, otherwise the PR layer may peel off. Figure 6.10 shows the die line area in a glass wafer after 160 minutes etching. At the corner of the lines, some photo resist have been removed and the glass area underneath is exposed. Hence, the choice of etchant is important.

Figure 6.10. PR peel off due to long time wet etching

The mask layer used for glass etching is the thick PR layer AZ-9260. The PR layer is 10 μm thick and exposed under a $365nm$ wave-length ultra violet (UV) light for 6 minutes. The UV light has a intensity of $9.3MV/cm^3$. After exposure, the wafer is immersed into the developer for 10 minutes and the exposed part in PR layer is pulled off, as shown in Figure. 6.2(a). A typical device pattern in the glass wafer after the first etching is examined by stereo scope, as shown in Figure. 6.11. Two square cavities represent the pressure sensor and the reference capacitor, respectively. The straight lines are the dice lines to separate different sensor dices.

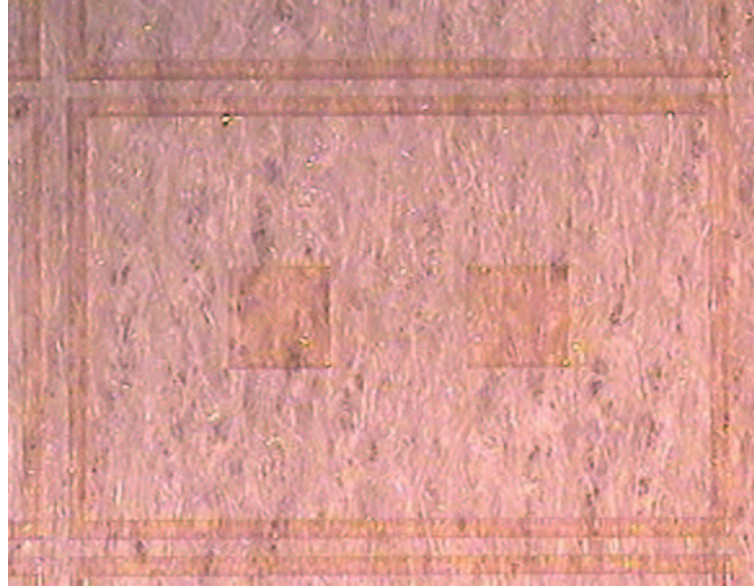

Figure 6.11. Glass wafer after 1st etching with PR remained

The Pyrex glass wafers are then submerged in a solution mixture of $HF(49\%)$: $H_2O(1:5)$ (buffered HF) for etching experiments. The concentration of 1 : 5 was chosen to obtain smooth and regular surfaces [89]. Another solution of BOE (Buffered Oxide Etch) containing $HF(49\%) : NH_4F(40\%)$ in 1:6 ratio, is also used to compare the etch rates. The etching is conducted in the wet etching bench at a room temperature and the etching reactions of the glass is:

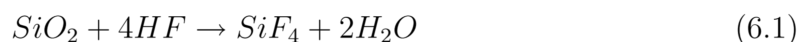

$$SiO_2 + 4HF \rightarrow SiF_4 + 2H_2O \quad (6.1)$$

Figure. 6.2(b) shows that after glass etching, a cave is left at the area without

Etchant No.	Etch time (min)	Min depth (μm)	Max depth (μm)	Etch depth (μm)
1	0	8.7840	9.1432	
(Buffered HF)	15	10.7372	11.7069	1.9532~2.5637
	30	13.9138	15.0195	5.1298~5.8763
	60	19.6416	20.2757	9.8576~10.1325
2	0	9.4870	9.7034	
(BOE)	15	9.6750	9.9876	0.1880~0.2842
	60	10.7589	10.9573	1.2539~1.2719
	100	12.2409	12.9637	2.7539~3.2603
	160	5.322	7.726	PR peels off

Table 6.3. Etch depths on glass wafer with PR layer

PR layer. The actual depths formed by PR layer and the glass cavity are listed in Table 6.3. The initial depths indicate that the thickness of the PR layer is close to $10\mu m$ where no glass cavity is formed. It can be concluded from the Table 6.3 that the etch rate of buffered HF is $0.168\mu m/min$ and the etch rate of BOE is $0.021\mu m/min$. Thus, the BOE etchant is not appropriate to form deep cavity and the etchant buffered HF is used to etch a $10\mu m$ deep cavity on the glass wafer. After the wet etching, PR is removed by putting the wafer into Acetone.

6.3.2 Metallization

After the glass etching, an electrode of the capacitor as well as the electrical leads need to be formed and patterned on the glass cavity. Besides, another electrode of the capacitor is formed on the front side of SOI wafer. All these electrical parts are formed by metallic thin films, and there are a variety of metal deposition techniques including sputter deposition and electron-beam evaporation. Aluminum (Al) is probably the most common metal used sputter deposition at low temperature[90]. However, Al has a melting temperature point of 400^oC. As subsequent processes, such as PECVD and anodic bonding, normally require process temperatures of

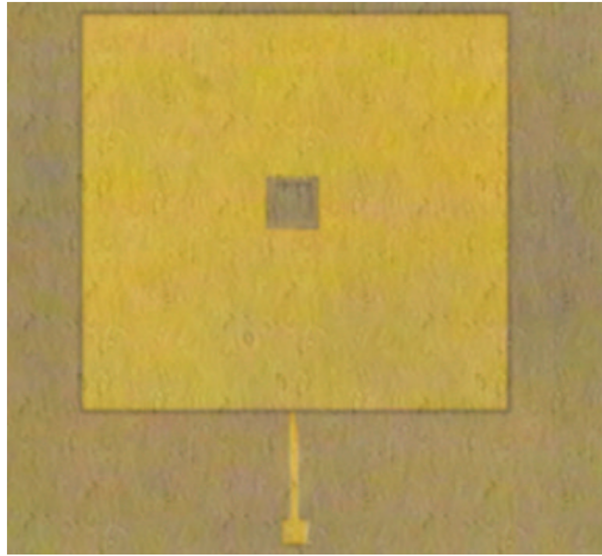

Figure 6.12. Glass wafer after e-beam evaporation of Au/Cr

$300 \sim 400^oC$, Al is not suitable.

Besides the Al sputtering, another metallization method, E-beam evaporation, is a high-temperature process that typically form Au/Cr compounds that can sustain temperature as high as 700^oC [91][92]. Moreover, high deposition rates, typically 50nm/s, are possible with electron e-beam evaporation, generally 10 times faster than sputtering [7]. Therefore, E-beam evaporation of Au/Cr together with lift-off technique are employed to form and pattern the metal layers. The E-Beam

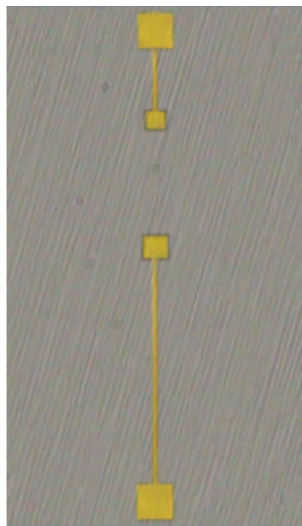

Figure 6.13. E-beam evaporation Au/Cr film on the SOI wafer

evaporation is conducted on the model ZBA-23 variable rectangular beam spot system. After the thick AZ-9260 PR layer is patterned, an electron beam of 20 keV acceleration voltage, is scanned over the wafer, generating a vapor for deposition. E-Beam evaporation emission of electrons from a filament source always heat wafers to high temperatures. Magnetic field are used to steer the electron beam into the wafer surface and locally melt the wafer materials under high temperatures. Figure. 6.12 shows the glass wafer after Au/Cr e-beam evaporation, where electrical leads and the electrode of capacitor are formed. The metal layer is also formed on the front side of SOI wafer, as shown in Figure. 6.13.

6.3.3 Thin film deposition

On the front side of SOI wafer, the passivation layer silicon nitride, the sacrificial layer silicon dioxide and the structure layer polysilicon are all fabricated by chemical vapor depositions, including LPCVD and PECVD. LPCVD is performed in a reactor at temperatures up to 900^oC, and this may cause thermal stress and potential damage to the metal layer. On the other hand, PECVD can be performed at a much safe temperature as low as 25^oC[93][94].

LPCVD silicon nitride

The 400 nm thick nitride layer is deposited on the front side of SOI wafer before metallization. Therefore, LPCVD with high process temperature of $775 \sim 800^oC$ can be used to grow low-stress silicon nitride layer. Besides LPCVD, PEVCD can also been used to form silicon nitride. However, PEVCD nitrides are not stoichiometric (Si_xN_y) and incorporate hydrogen. Compare to PECVD films, LPCVD nitride is extremely resistant to chemical attack, thereby making it the material of choice for many Si bulk and surface micromachining applications. LPCVD nitride is commonly used as an insulating layer to isolate device structures from the substrate, because it is a good insulator with a resistivity of $10^{16}\Omega - cm$ and a field breakdown limit of $10^7 V/cm$ [95]. The average Young's modulus of LPCVD silicon nitride thin films is 260.5 GPa at room temperature 25^oC [96].

The deposition temperature and pressure used are 800^oC and 500 mTorr, respectively. Under this conditions, an approximate deposition rate of $30A/min$ can be achieved. After two hours deposition process in the furnace, a $400nm$ thick LPCVD silicon nitride layer is coated on the SOI wafer surface. The common LPCVD silicon nitride deposition reactions are:

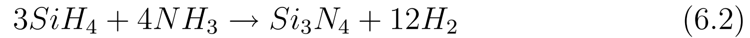

$$3SiH_4 + 4NH_3 \rightarrow Si_3N_4 + 12H_2 \quad (6.2)$$

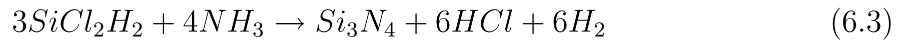

$$3SiCl_2H_2 + 4NH_3 \rightarrow Si_3N_4 + 6HCl + 6H_2 \quad (6.3)$$

The standard source gases are silane(SiH_4), dichlorosilane (SiH_2Cl_2) and ammonia (NH_3). SiH_2Cl_2 is used in place of SiH_4 because it produces films with a higher degree of thickness uniformity at the required deposition temperature. The thickness and uniformity of silicon nitride layer as measured by the SENTECH ellipsometer is shown in Table 6.4. It shows that the desired nitride thickness has been deposited.

Location No.	Film thickness (nm)
1	398.98
2	397.72
3	398.43
4	397.87
5	396.12

Table 6.4. Nitride layer thickness measured by the SENTECH ellipsometer

PECVD silicon oxide

On the SOI wafer, after LPCVD nitride and e-beam metallization, a sacrificial silicon dioxide is formed, as it can be easily dissolved using etchant that do not attack polysilicon. The SiO_2 can be grown thermally on Silicon substrates as well as deposited using a variety of processes, including LPCVD, thermal oxidation and PECVD. Thermal oxidation is performed at high temperatures from 900 to 1100

^oC [97][98], in the presence of oxygen or steam. LPCVD process is generally used for depositing thick ($> 2\mu m$) SiO_2 films at 450^oC using silane and oxygen[99], followed by an annealing step at 1000^oC. Therefore, the SOI wafers with metal layer can not be put into the thermal oxidation and LPCVD furnace due to the high process temperatures. Consequently, PECVD is selected to form the sacrificial oxide layer, because it offers the possibility to deposit films of the desired thickness at room temperature.

The PECVD process uses IPE 1000 PECVD reactors with tetraethylorthosilicate (TEOS) as the source gas. The gas pressure is typically 500 mTorr. The 50kHz and 1.2kW power supply pump electrical energy into the gas to reach the plasma stage. In the gas plasma, the atoms are ionized and both free electrons and ions are accelerated in the electrical field, and thus energy of individual atoms increases. However, the average kinetic energy of the plasma remains low, and so does the process temperature of PECVD. The PECVD silicon dioxide deposition reactions rely on TEOS decomposition:

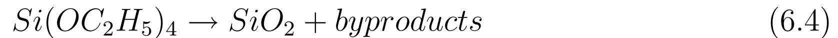

$$Si(OC_2H_5)_4 \rightarrow SiO_2 + byproducts \tag{6.4}$$

High deposition rate of 4.5 nm/min was obtained for low PECVD process temperatures at 25^oC. After the patterning in Alcatel RIE machine, the profile and thickness of the silicon dioxide layer was measured by Dektak profile scanner, as shown in Figure. 6.15. The measurement results are shown in Table 6.5.

Location No.	Film thickness (nm)
1	2043.82
2	2022.37
3	2034.03

Table 6.5. Thickness of PECVD silicon oxide layer measured by profile scanner

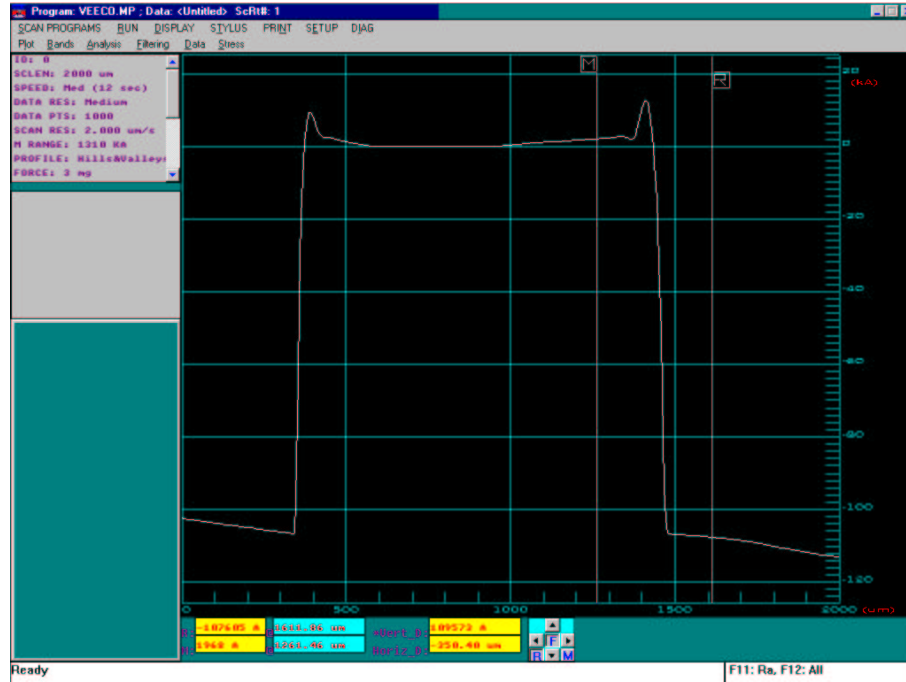

Figure 6.14. Profile of PECVD oxide layer measured in Dektak profile scanner

PECVD silicon polysilicon

As the structural material for cantilever middle diaphragm, Polysilicon is typically deposited using LPCVD by pyrolizing silane in a low pressure reactor at $600 \sim 650^oC$. To avoid the thermal damage on the metal layer, low temperature PECVD process can be used to deposit polysilicon [100] and the deposition reaction is:

$$SiH_4 \rightarrow Si + 2H_2 \tag{6.5}$$

The PECVD process is performed in a parallel plate PECVD deposition system, where 13.5 MHz and 12 W RF supply excite the gas to the plasma state. Silane (SiH_4) is used as the main process gas. The deposition is performed at the substrate temperature 194^oC and the total chamber pressure 200 Pa from hydrogen (H_2) to silane plasma. After the patterning in Alcatel RIE machine, the polysilicon thickness at various locations are shown in Table 6.6.

Figure. 6.15 shows silicon oxide layer after patterning, the center square box represents the cavity where the polysilicon post will be formed subsequently. The polysilicon layer is shown in Figure. 6.16. The size of polysilicon diaphragm is

Location No.	Film thickness (nm)
1	1423.82
2	1512.54
3	1458.12

Table 6.6. Thickness of PECVD polysilicon layer measured by profile scanner

designed to be smaller than that of oxide, so that polysilicon does not connect to nitride underneath the oxide layer, so free-standing edges of polysilicon diaphragm can be secured.

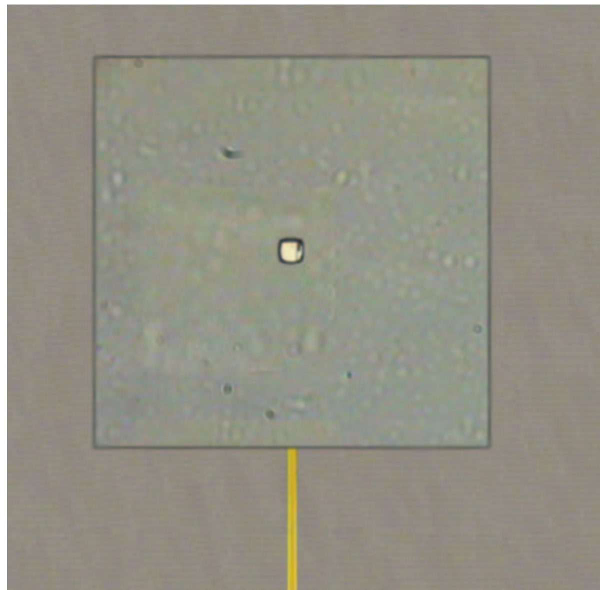

Figure 6.15. Silicon oxide layer after patterning observed in microscope

6.3.4 Release etching and drying

The cantilever middle diaphragm is formed by surface micromachining process, where the PECVD polysilicon and silicon dioxide films act as the structural material and sacrificial material, respectively. The oxide is readily dissolved in HF solution without the polysilicon being affected. There are some fabrication issues associated with the sacrificial etching process, including the geometry of the

diaphragm, and the chemistry of the release etching process.

Diaphragm geometry

In the release etching process, the selectivity of HF based solutions to oxide vs. polysilicon is very high. However, unlike the nitride layer, polysilicon layer is more liable to be etched through, by the fact that both sides of polysilicon diaphragm are eventually exposed to the etchant during the course of release etching. Therefore, for large diaphragm cases, where long time release etching is required, the selectivity may not be high enough. In the fabrication of proposed sensor, the PECVD polysilicon layer is $1.5\mu m$ thick at the time of release etching. The 120:1 selectivity to oxide vs. polysilicon limit the diaphragm sidelength to $900\mu m$. A large diaphragm would be completely etched through its thickness before the lateral etch of the oxide is complete. Furthermore, the lateral oxide etch rate is

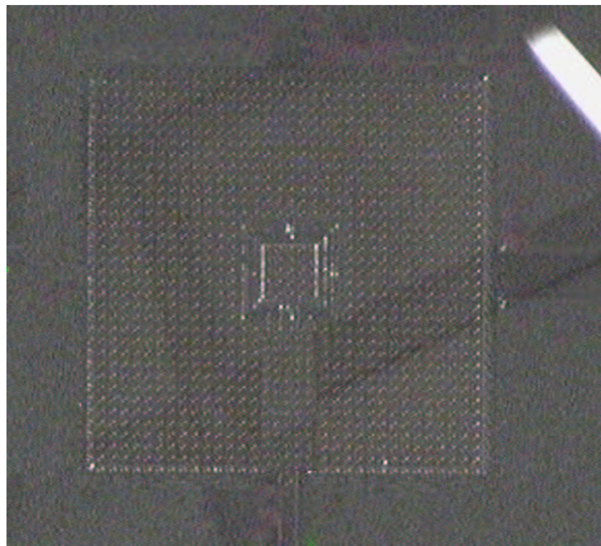

Figure 6.16. Improve release etch property by adding etch holes in polysilicon diaphragm

reduced dramatically by diffusion limitations at the region close to the center post. To improve release etch characteristics by diaphragm geometry, it is desirable to decrease the lateral distance of release etching. By introducing square etch holes of $10\mu m \times 10\mu m$ in the polysilicon diaphragm, as shown in Figure. 6.16, the perime-

ter of exposed thin oxide increases so that better release property as well as faster etch rate can be achieved. The lateral spacing of etch holes are $15\mu m$. For all sizes of diaphragm, the size and spacing of the etch holes are identical, the amount of perimeter occupied by the etch holes is summarized in Table 6.7. As a result of identical etch holes and spacings, a constant percentage of release etching perimeter is occupied by etch holes. Therefore transport of etchant during the etch of large diaphragm is not significantly restricted, and the mechanical characteristics of the large diaphragm is not changed much as well.

Diaphragm size (μm)	Number of etch holes	Percent perimeter occupied by etch holes
500	320	5.12%
600	446	4.95%
680	584	5.05%

Table 6.7. Percent perimeter occupied by etch holes for different diaphragm sizes

Due to the existence of etch holes, the typical process time of release etching is 30 to 40 minutes at room temperature, using $HF(49\%) : H_2O(1:1)$ solution. However, some regions in the $0.40\mu m$ thick nitride layer may be etched through, as shown in Figure. 6.17.

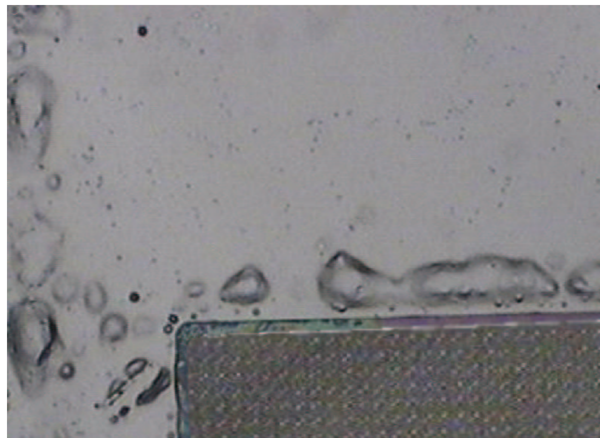

Figure 6.17. Damage in nitride layer due to poor selectivity of release etching

Etch chemistry

In the release etching, HF solutions will attack silicon nitride as well as polysilicon. Since the nitride layer is $0.4\mu m$, high selectivity to oxide vs. nitride is required to avoid etch through in the nitride insulation layer. The approach for optimizing release etch characteristics by changing the chemistry of the etchant, can be realized by adding HCl to HF [101][102].

Two solutions are used to release the silicon oxide: $HF(49\%) : H_2O(1 : 1)$ and $HF : HCl(37\%)(1 : 1)$. Lateral oxide etch rates are estimated from optical micrographs of release etching structures, while nitride etch rates are measured by ellipsometer. The results are compared in Table 6.8. It can be seen that by adding HCl to HF solution, both oxide etch rate and selectivity are improved and the fabrication objectives can be met.

Etchant	Oxide etch rate	Nitride etch rate	Selectivity
$HF(49\%) : H_2O(1 : 1)$	$20\mu m/hr$	$0.22\mu m/hr$	91
$HF : HCl(37\%)(1 : 1)$	$37\mu m/hr$	$0.12\mu m/hr$	310

Table 6.8. Etch characteristics for different etchant

6.3.5 Anodic bonding and backside etching

The glass and SOI wafers are bonded together by anodic bonding technology in an SB-6 Substrate Bonder (Suss). The two wafers are brought into point contact under pressure in the central area. Next, the spacers are pulled out to allow the rest area of the glass wafer to be in contact with the silicon wafer. Finally, anodic bonding is carried out to bind the SOI and glass wafer by applying a voltage on both wafers. The negative electrode is connected to the glass wafer, with the respect to the voltage applied on the SOI wafer. After the wafer level anodic bonding, the qualities of the bonded pairs can be directly checked with visual inspection.

Parameters for the anodic bonding process, which include magnitude of the applied DC voltage, bonding pressure, nature of surface to be bonded, and bonding time, are illustrated in Table 6.9. The bonding properties between 4 inch silicon

wafer, nitride coated SOI wafer and Pyrex 7740 glass wafer are studied. Bonding between silicon and glass is easy to achieve in a very short time, and more than 95% area in 4 inch wafer scale is completely bonded. When negative voltage is applied, mobile sodium ions in the glass are attracted toward the cathode, creating a high electrostatic field at silicon-glass interface[103]. However, a dielectric silicon nitride thin film on SOI prevented the formation of electrostatic field and poor bonding may result. More bonding time and bonding pressure are required to overcome the influence of dielectric layer. Only 85 % bonded area is observed even if the same voltage is applied for more than 30 minutes and the bonding pressure is increased to 2000 mbar (Case 4).

Case No.	Deposited film	Bonding pressure	Bonding time	Bonded area
1	Glass to Si	1000 mbar	5 min	95 %
2	400 nm SiN_4	1000 mbar	5 min	45 %
3	400 nm SiN_4	2000 mbar	5 min	55 %
4	400 nm SiN_4	2000 mbar	30 min	85%

Table 6.9. Bonding parameters for SiN_4 deposited silicon to glass. applied voltage 800 V, bonding temperature: 400^oC

Using the optimized bonding condition (Case 4), the SOI wafer with insulating silicon nitride is successful bonded with Pyrex 7740 wafer, as shown in Figure. 6.18

After bonding the glass and SOI wafer, the sensing diaphragms are formed on the SOI wafers by back etching to the handle layer. A silicon dioxide layer (buried oxide) acts as a separator between device and handle layers of silicon in a SOI wafer. It can act as an etch stop during wafer back etching. Deep RIE process can be used to etch through the handle layer of SOI. In contrast with wet etching, RIE allows for the creation profiles with high depth and with vertical walls. Figure. 6.19 shows a typical cavity obtained by deep RIE on a SOI wafer with a $400\mu m$ thick handle layer.

Deep RIE is performed using STS ICP RIE etcher and an etch rate up to 2 $\sim$

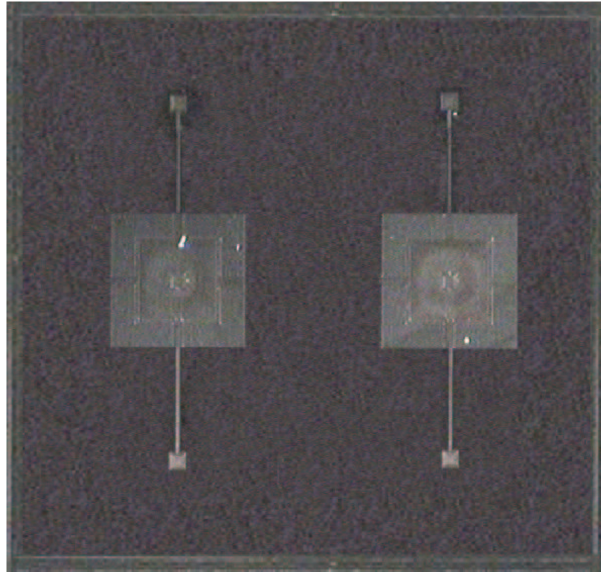

Figure 6.18. Sensor device after anodic bonding

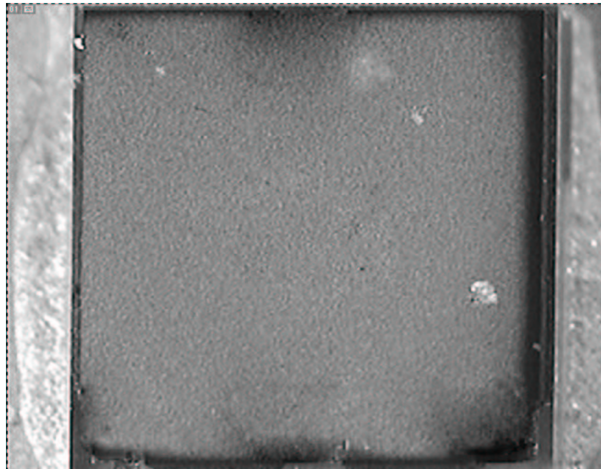

Figure 6.19. Backside of SOI wafer after deep RIE etching

$3\mu m/min$ can be achieved due to the large open area. There are some important issues during deep RIE, such as over heating of wafers, masking materials, etch depth non-uniformity. Overheating of the bonded wafer stack during deep RIE may bring thermal stress for bonding area. It may also cause a significant change of masking material etch rate, thereby, decreasing its selectivity to silicon. In order to compensate for overheating, the deep RIE process is separated into 2 or 3 steps. Photo resist AZ-9260 is used as the masking material for deep RIE. However, the etch selectivity is about 100:1. Therefore, to etch through $400\mu m$ thick handle

layer, photo resist has to be thicker than $5\mu m$. In the back etching, since the area open for RIE is less than 15%, then etch rate non-uniformity across the wafer is typically within the $3 \sim 5\%$ range. Etch depth uniformity requires over etching which may strip off buried oxide. Therefore, the sensing diaphragm is a single layer film made of silicon, without the problems in multi-layer films, including delamination and thermal stress between different layers. Typically, over-etch time occupies as much as $15 \sim 35\%$ of the process time.

6.4 Test of sensor performance

Four different sizes of diaphragm are fabricated: 500, 600, 670, 700 μm. Sensor geometries are decided by the optimization design in Chapter 5. These four sizes are in group of six chips each. Each sensor chip has a active and a dummy diaphragm, and the dummy unit works as the reference capacitor. Both the active sensor and the dummy capacitor has two bond pads for signal output. There are two category for each size group, with different wiring configuration. One category has active and dummy units electrically separated, which means both can be independently tested. In another configuration, active and dummy units have one of their electrode being connected. In this manner, the two capacitors can be connected to a AC power supply in parallel.

6.4.1 Testing rig

The testing rig for the pressure sensors is constructed, and the schematic of the test system is shown in Figure. 6.20. The test set consists of a steel pressure box, a pressure source vessel and pump, a probe station with microscope, and a measurement equipment. In all the measurement, the pressure source is silicon oil that can be pressurized to $700kPa$. By penetrating through the small holes in the pressure box, the pressurized oil is in contact with the sensor sensing diaphragm and can force it to deflect, as shown in Figure. 6.20. A cover with eight screws is used to hold the testing wafer on the pressure box, and two rubber O-rings is used

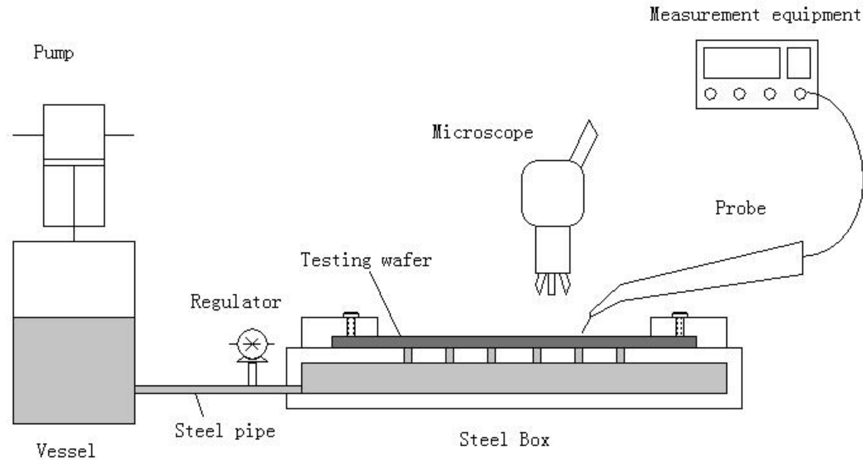

Figure 6.20. Schematic of pressure sensor test setup

to prevent oil leakage. To withstand the high pressure, both pressure box and the cover is made of stainless steel. At the side of the steel box, there is a pressure inlet connecting a steel pipeline and a pressure regulator used for monitoring the pressure inside the box. The steel pressure box has a diameter of 160mm, a height of 30mm and a wall thickness of 5mm. The highest pressure the box can sustained is 1000kPa. This upper limit is designed to comply with the safety requirement in the lab.

The probe station with a microscope is used to connect the sensor bond pads to the measurement equipment, such as a LCR meter or a signal conditioning board. In most measurements the pressure box is pressurized to a high house pressure, and then slowly depressurized while the in-house pressure and sensor output are observed. The change in the sensor capacitance is manually read from the measuring instrument, and the magnitude of pressure is indicated by the pressure regulator.

6.4.2 Capacitance Measurement using LCR meter

Unlike the multi-meter that measure capacitance using a DC source, the typical method for high accuracy capacitance measurement is to stimulate the capacitor under test with an AC source, such as in high-performance LCR meters. An AC signal of known frequency is applied through an internal low value resistor and

the capacitor under test in a series configuration. The AC current flowing into the capacitor must also flow through the resistor, creating an AC voltage across the resistor. The magnitude and phase of this voltage can be measured and compared to the original AC signal, and the capacitance can be computed. Techniques such as this frequency-domain measurement can be very accurate. However, the error terms inherent in a capacitance measurement cannot be thoroughly avoided, for example, the parasitic capacitance.

Estimation of parasitic capacitance

One of the challenges of capacitance measurement is the effect of parasitic capacitance. Before characterizing the actual sensor components, the parasitic effect due to connecting wires and surrounding fixture is first measured. In order to determine values of these parasitic elements and to find an equivalent circuit for the measurement fixture, it is necessary to make some measurements of the fixture itself, and extract the values of the parasitic capacitance from these measurements. The parasitic capacitor can be regarded to be connected in parallel to the device, thus following equation holds:

$$C_{system} = C_{device} + C_{parasitic} \tag{6.6}$$

In order to accurately determine the parasitic capacitance associated with the test fixture, measurements are made at frequency of 10, 50, and $100kHz$. The sinusoidal amplitude is set to $20mV$ in the measurement. To estimate the parasitic capacitance, the capacitance $C_{parasitic}$ is measured when the probes are not in contact with the sensor bond pads. The results is shown in Table. 6.10.

	Test 1	Test 2	Test 3	Average
10 kHz	0.5911 (pF)	0.5904 (pF)	0.5967 (pF)	0.5927 (pF)
50 kHz	0.6093 (pF)	0.6117 (pF)	0.6269 (pF)	0.6160 (pF)
100 kHz	0.6204 (pF)	0.6187 (pF)	0.6171 (pF)	0.6187 (pF)

Table 6.10. Parasitic capacitance for the testing system

It can be seen that the capacitance of both LCR meter and probe station changes from $0.5927pF$ to $0.6187pF$ as the measurement frequency is altered. The parasitic capacitance is estimated by applying a sinusoidal activation signal with a magnitude of $20mV$, under different testing frequencies from 10 to $100kHz$. By applying high frequency of $100kHz$, the measurement data in Table. 6.10 indicates that the error bounds may have a magnitude of $0.017pF$, or in terms of percentage, the errors seen in the test are on the order of 2.7%.

To measure capacitance as small as several picofarads, the results may be more accurate if applying sinusoid activation signals of high frequency, such as $100kHz$. In this case, the parasitic capacitance is equal to $0.6187pF$. This parasitic capacitance value of $0.6187pF$ significantly affects extracted device capacitance value C_{device} when the latter was smaller e.g. more than 2.7% error below $0.017pF$. The remaining error, at low C_{device} value, could be caused by leakage currents at the pins. The smaller C_{device} value is, the greater this effect would be. Because the physical mechanisms that degrade the measurement accuracy vary significantly with process, temperature, time and other environmental variables, it is difficult to correct these errors. The measurement results presented in the thesis are relatively consistent over a short period of time. Comparing measurements over a long period of time gave results that were not as consistent. It appears that drift with temperature and capacitor dielectric absorption may cause the inconsistencies.

Capacitance pressure characteristics

After determining the magnitude of the parasitic capacitance due to testing fixtures and neighboring circuits, the capacitance of the sensor device is then measured. Further measurement can be done to find the capacitance pressure characteristics for the sensors. The geometry of the sensors under test are as follows:

Experimental capacitance pressure characteristics is shown in Figure. 6.21. These curves are shown for four sizes of diaphragms: 500, 600, 670 and 700 μm. In the figure, the sensor capacitance is obtained by subtracting parasitic capacitance of $0.6187pF$ from the LCR readings. In general, larger diaphragms will lead to

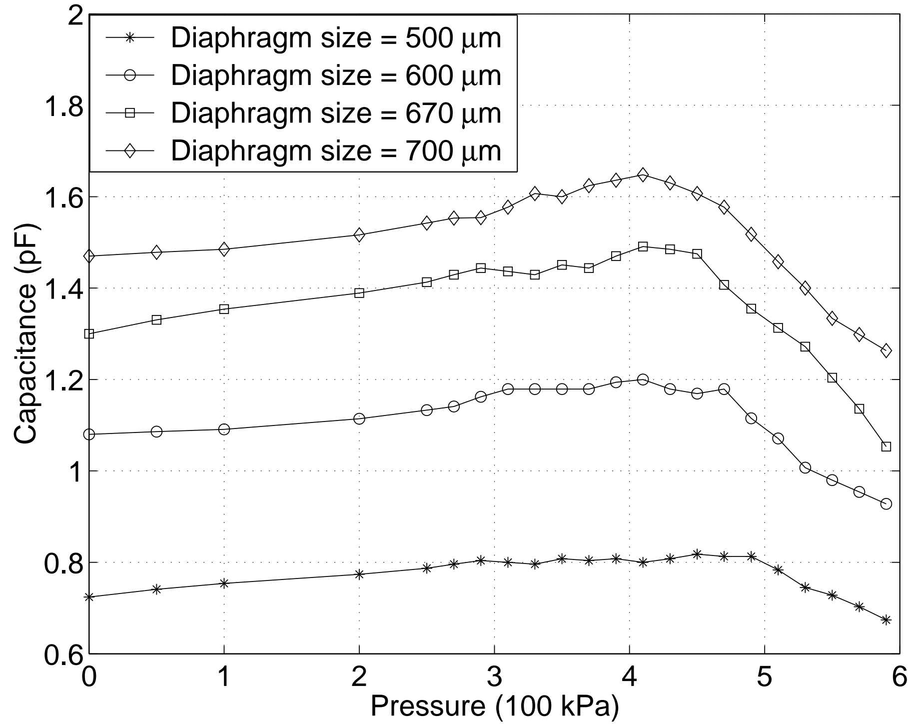

Figure 6.21. Capacitance-pressure characteristics for sensors with different diaphragm sizes

higher nominal capacitance, and the case of diaphragm size $700\mu m$ has the largest nominal capacitance of $1.47pF$. There is not a monotonic relationship between output capacitance and applied pressure. It can be found that there are turning points at all the capacitance-pressure curves, near 400 to $500kPa$. The changes in the slope of curves indicate that the middle diaphragm contacts the substrate and deflects in the opposite way. The slopes increase obviously after the turning points.

The sensitivity is obtained by fitting a straight line to the data points in Figure. 6.21 in least square sense, and calculating the slope. For each diaphragm size, both the sensitivities before and after the touch point are computed, and the results are listed in Table. 6.11. For larger diaphragms, the touch point pressure decreases, or in other words, the diaphragm contact occurs earlier. The sensitivity is enhanced greatly after the touch point, the percentage of enhancement varies from 441% to 709%, for different diaphragm sizes. The largest sensitivity enhance-

ment is at the case of 670μm diaphragm size, which also has the largest sensitivity of 3.28fF/kPa in the contact mode. This is consistent with MOEA optimization presented in Chapter 5 that a diaphragm with side length of 670μm has optimal sensitivity.

Diaphragm Size	Touch point pressure	Sensitivity (fF/kPa)	
(μm)	(kPa)	Before touch	After touch
500	470	0.217	1.305
600	430	0.313	1.695
670	410	0.405	3.280
700	410	0.429	2.455

Table 6.11. Sensitivity of capacitive pressure sensors obtained from measurement

The measurement results of sensors with 670μm diaphragm size are compared to the results from computer simulation, as shown in Figure. 6.22. In the region before the touch point pressure, the two curves are close to each other. Even at the transient region, the error between the two curves is small, without exceeding 5%. However, after the touch point region, the curve of measurement data does not change as fast as the simulation curve, and the error is larger.

6.4.3 Capacitance Voltage conversion

The capacitance of the pressure sensor is mainly determined by the geometrical dimensions. The typical nominal capacitance of the sensor is from 0.724 to 1.41pF, as measured in previous section. To measure these small capacitance, a sinusoid activation signal and a sensitive detecting circuit is needed. The capacitance is so small that the readout may be interfered by surrounding environment. Therefore, the circuit must have good suppression ability of parasitic effects, and the circuit layout should be designed carefully. Hence, a commercial C-V conversion board designed specially for MEMS is used to characterize the sensor.

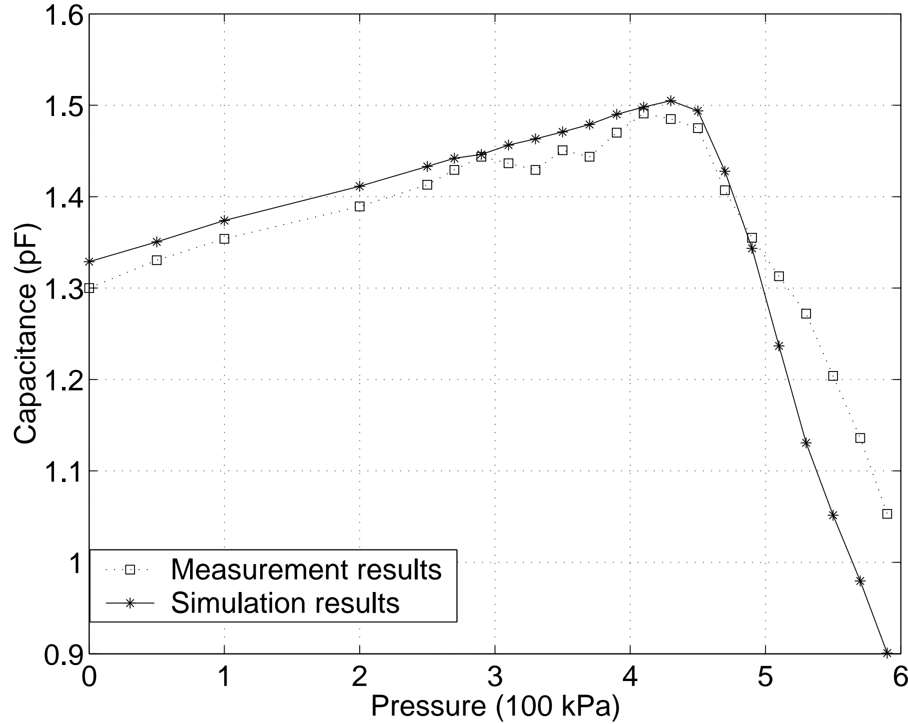

Figure 6.22. Characteristics of the sensor with $670\mu m$ diaphragms, comparison between measurement and simulation results

MS3110 board

For practical purpose, it is very important to have a high resolution circuit that can detect small changes in capacitance. This high precision can not achieved by traditional methods, such as RC oscillation circuit, Pulse Width Modulator. On the other hand, the capacitive sensor has small capacitance, which results in large impedance, so it is difficult to detect using a DC signal. An AC signal is helpful to decrease the impedance. The Universal Capacitive Readout IC (MS3110) is a general purpose, ultra-low noise CMOS IC. This chip support a variety of applications that demands a high resolution capacitive readout interface. The basic concept of the measurement board is shown in Figure 6.23. Here,$U(t)$ must be a high frequency sinusoid signal since capacitor blocks DC signals. C_1, C_2 are sensing and reference capacitor, respectively. U_{out} is the output voltage of the circuit. Since the impedances of the capacitors are inversely proportional to frequency, the frequency should be chosen for $U(t)$ so that create a voltage across

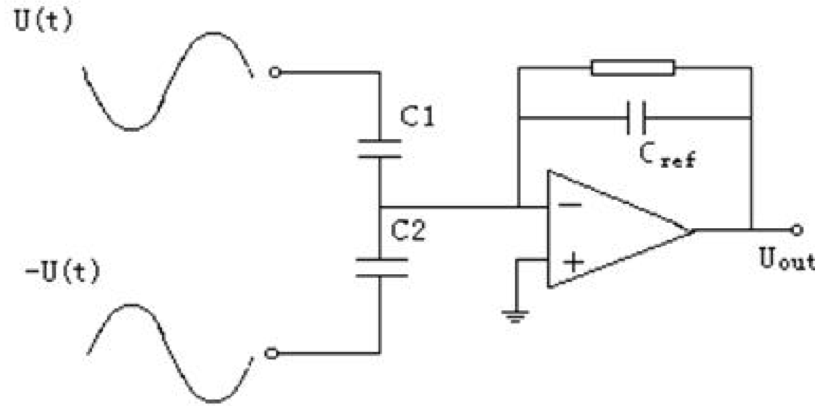

Figure 6.23. Working theory of MS3110 measurement board

the capacitors which is appropriate for amplification. A resistor must be placed at the feedback part so as to form a path for the input bias current of the amplifier to flow. Otherwise, charges will accumulate at the negative input terminal and the operational amplifier will be saturated. The magnitude of output voltage signal is given by:

$$U_{out}(t) = \frac{C_1 - C_2}{C_{ref}} U(t) = \frac{\Delta C}{C_{ref}} U(t) \tag{6.7}$$

The Evaluation Board needs a $+5V$ DC supply for operation. The DC supply is connected to the banana jacks located on the upper edge of the board. In the measurement, the MS3110 chip works in different mode. The calibration data is listed in Table. 6.12 The settings of the measurement are:

Reference Voltage $= 2.259V$; (nominal)

Reference Current $= 0.010mA$; (nominal)

Frequency of Square Wave $= 100.6kHz$; (+24%)

$C_{ref} = 0.513pF$;

The relationship between $CS_2 - CS_1$ and V_{out} is shown in Figure. 6.24. The output voltage goes into saturation for a large capacitance difference. The output voltage is always within $0.25 \sim 5.0V$, which is decided by input voltage of the amplifier. When capacitance difference is between $-0.095pF$ and $0.095pF$, the

CS2-CS1 (pF)	-0.323	-0.266	-0.247	-0.209	-0.133	-0.095	-0.057	-0.038
Vout (V)	0.263	0.287	0.305	0.365	0.916	1.277	1.630	1.817
CS2-CS1 (pF)	-0.019	0	0.019	0.038	0.057	0.095	0.133	0.209
Vout (V)	1.993	2.180	2.358	2.536	2.714	3.071	3.43	4.15
CS2-CS1 (pF)	0.247	0.266	0.323	0.342				
Vout (V)	4.50	4.68	4.99	4.99				

Table 6.12. Calibration data of MS3110 measurement board

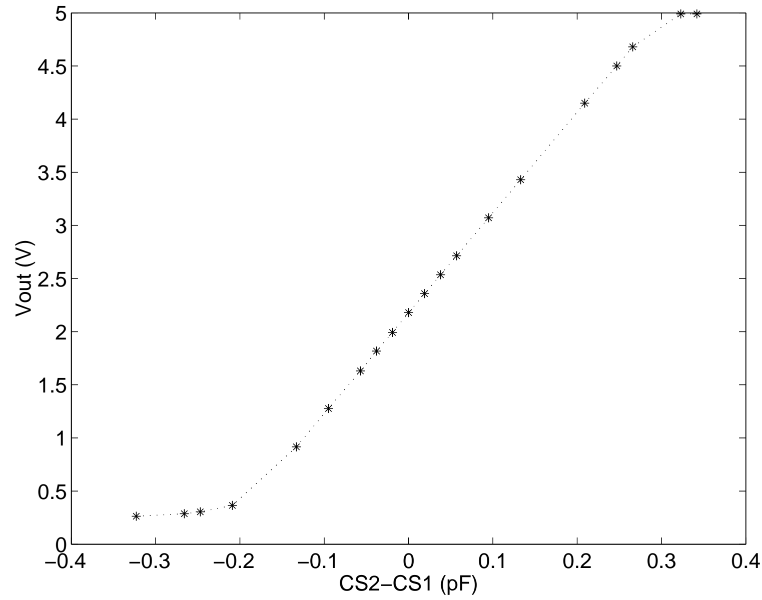

Figure 6.24. V_{out} vs Differential Capacitance $CS_2 - CS_1$ ($C_{ref} = 0.513pF$)

response of the chip is in a linear range. From data in this range, a first order function can be obtained:

$$V_{out} = 9.4636 * (CS_2 - CS_1) + 2.1751 \tag{6.8}$$

Theoretically, the above function can be verified by following expressions provided by MS3110 data sheet:

$$\begin{aligned} V_{out} &= (V_{ref})(1.14)(GAINSEL)\frac{CS_2 - CS_1}{C_{ref}} + V_{ref} \\ &= 2.259 * 1.14 * 2 * \frac{CS_2 - CS_1}{0.513} + 2.259 \\ &= 10.040 * (CS_2 - CS_1) + 2.259 \end{aligned} \tag{6.9}$$

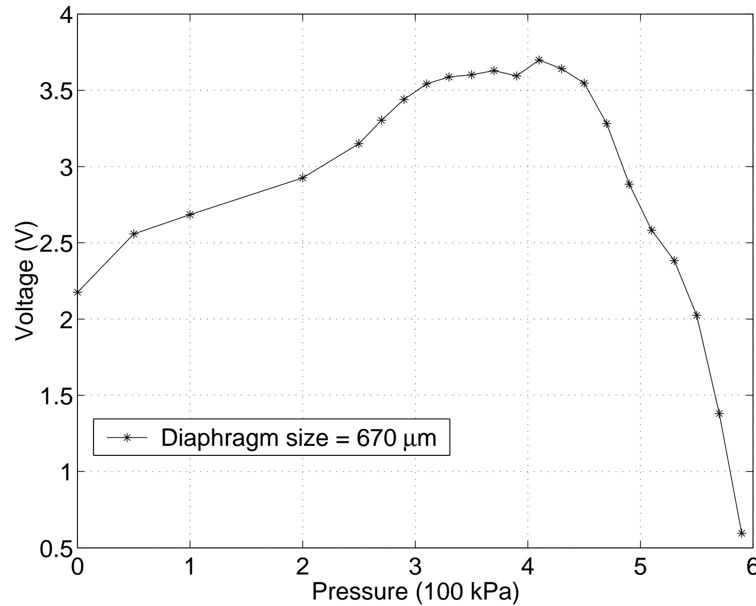

Figure 6.25. Voltage output vs applied pressure

Voltage pressure characteristics

Besides the conversion from capacitance to voltage, another merit of using MS3110 board is it only concern on the differential capacitance between the active and the reference capacitor. Since the reference capacitor has the identical nominal value as the active one, the effect of temperature, surrounding environment, and the parasitic capacitance can be reduced greatly. The voltage output under the applied pressure is shown in Figure. 6.25. From Figure. 6.25, sensitivity is $15.25mV/kPa$ when the sensor operates in the contact mode. The voltage pressure curve swings from $2.1V$ to $4.0V$, and then drops steeply to $0V$. These voltages are quite easy to detect or handled in the electronic circuits. The output voltage can be monitored by an oscilloscope or a high accuracy multi-meter. In the oscilloscope, V_{out} is a thick straight line of $0.1V$ width.

Figure. 6.26 shows the corresponding capacitance vs pressure characteristics measured by MS3110 board. The results are used to compare with the curve directly obtained by LCR meter. The change in MS3110 measurement curve is more smooth than in LCR results. Since the MS3110 board works in a differential mode, the disturbance of surrounding environment have been cancel out largely by

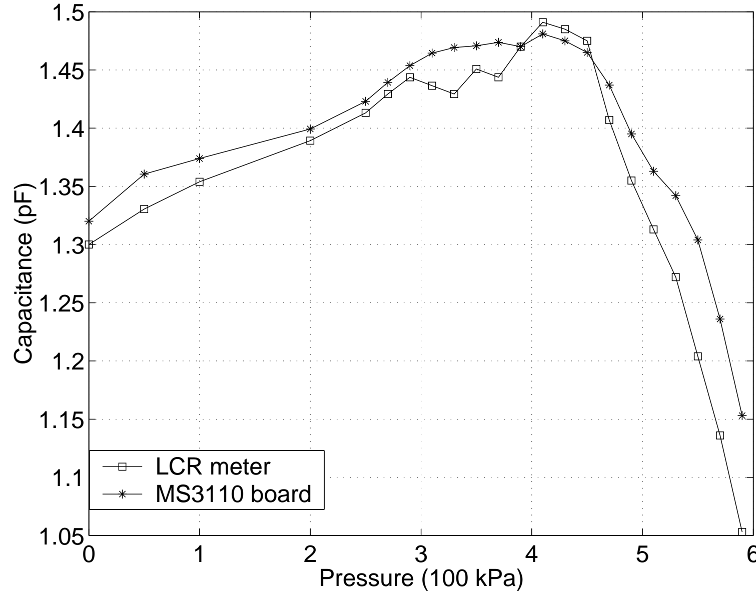

Figure 6.26. Capacitance vs applied pressure, from different methods

reference capacitors.

6.5 Conclusions

This chapter has proposed the fabrication procedure for the proposed pressure sensor, which includes the bulk micromachining on the glass wafer, the surface micromachining to form the cantilever diaphragm in the SOI wafer, and the anodic bonding of two wafers followed by backside deep etching. The process flow is described by using schematic cross section of main processing steps.

The important features of the fabrication process are illustrated in succession. Two types of positive photo resist are employed in lithography patterning, AZ9260 stands for large feature sizes while AZ7220 stands for small feature sizes. Buffered HF is adopted in glass wet etching due to its high etch rate of $0.168\mu m/min$. The metal layer is formed by e-beam evaporation using the material of Au/Cr, which has a large deposition rate of 50 nm/s. Besides, Au/Cr metal layer tends to tolerate process temperature as high as 700^oC. Before metallization, high temperature LPCVD process can be used to form the 400nm thick nitride layer. Meanwhile, only PECVD processes are used to deposit silicon oxide and polysilicon, in order

to avoid the possible thermal attack on the metal layer. To facilitate the sacrificial etching under the large polysilicon film, etch holes are properly put onto the film. Moreover, by adding HCl to HF based solution, it is possible to achieve high release etch rate and less damage to nitride layer. Anodic bonding is used to bind two wafers together and deep RIE etching is performed on the backside of the SOI wafer. By using some metrology measurement tools, the film thickness and pattern sizes can be examined and analyzed.

Upon obtaining the completed sensor devices, their electrical performance are tested in a hydrostatic pressure system. The system is designed and used to test the sensor performance. Four categories of sensors with different diaphragm sizes have been tested and the changing capacitance is detected by LCR meter. The capacitance pressure curves shows different relationship before and after the turning point. The sensor with $670\mu m$ has the largest sensitivity improvement of 709% after diaphragms contact. However, the testing results in this chapter can only used for concept proof. It still need more work to apply the idea to the commercial pressure sensor. For the practical purpose, it is always necessary to convert the capacitance value to voltage output. MS3110 board is utilized to provide such a conversion. The voltage output of the pressure sensor is between 0 to 4.0 V, which can be easily handled by the normal electronic circuits.

Chapter 7

Conclusions and Suggestions

7.1 Conclusions

This thesis proposed and analyzed a novel micro capacitive pressure sensor with two movable diaphragms, including performance simulation in FEM software, analytical modelling, graphical design and geometry optimization using genetic algorithm, the fabrication process and sensor performance test.

The newly developed capacitive pressure sensor is proposed to address the need to detect small variations in a large pressure ambient. The new sensor is a parallel plate sensor with a fixed electrode on the rigid substrate, and an electrode on one of the movable diaphragms, the cantilever middle diaphragm. When high pressure is applied, the deflections of thick sensing diaphragm are very small, and these small deflections are magnified in the middle diaphragm when the two movable diaphragms come into contact. FEM software ABAQUS is employed to simulate the diaphragm deflections and interactions between diaphragms. The geometric data of the deformed middle diaphragm can be used to estimate the sensor capacitance, based on an integration method. Simulation results show that the proposed sensor with this magnification mechanism has a promising capacitance-pressure characteristics while operating in the contact mode. Besides the ability to sustain large pressure, it has a sensitivity comparable to normal parallel plate capacitive pressure sensors working at low pressure environment.

From the ABAQUS simulation results, effects of geometric parameters on sensor performance have been discussed. Large diaphragm size will enhance the sensitivity, and large post size results in the reduced sensitivity. Increasing boss ring size may help to enlarge sensitivity, but further increase will make the sensitivity smaller. A graphical design tool is developed to design the proposed pressure sensor. To meet specification requirement, diaphragm sizes and gap height between diaphragms are selected first, then the boss ring size and post size are fine-tuned to find a better sensitivity. The graphical design is a good choice for selecting suitable parameters in a quick way. However, the graphical design only vary two parameters simultaneously at a time. Thus, the selected set may not be the optimal choice in view of the whole design space. Another approach like genetic algorithm is employed to design and optimize the sensor geometry.

In the use of genetic algorithm to select geometrical parameters of sensors, an analytical model is proposed to estimate the characteristics of micro sensor. For the proposed capacitive pressure sensor, the analytical model can predict the deformed geometry of clamped-edge sensing diaphragms by means of energy method, and the deflections of cantilever middle diaphragms are also discussed and characterized. Compared to ABAQUS results, the analytical model can predict diaphragm deformation behavior with less than 3.2% error. Unlike ABAQUS, the analytical model can be incorporated into the genetic algorithm in MATLAB. The optimal design method using genetic algorithm is desirable because the evaluation of sensor performance is based on the whole design space, where all the device parameters can be varied simultaneously.

The last concern in this thesis is to fabricate the sensor and test its performance. The sensor is fabricated by using the standard micromachining technology, which includes the bulk micromachining on the glass wafer, surface micromachining to form the cantilever diaphragm on the SOI wafer, and the anodic bonding of two wafers succeeded by backside deep etching. The important features, conditions and fabrication results of the process are illustrated in detail. Buffered HF is adopted in glass wet etching due to its high etch rate. High temperature LPCVD

process can be used to form the insulating nitride layer. The metal lines are formed by e-beam evaporation using the material of Au/Cr, which can sustain high temperatures in following processes. PECVD processes are used to deposit silicon dioxide and polysilicon films. Release etching is performed by HCl to HF based solution. Anodic bonding is used to bind two wafers together and the SOI wafers are deep etched from backside so as to define the sensing diaphragm. The electrical performance of sensors are tested in a hydrostatic pressure system. Due to the safety concern, the applied pressure can only be pressurized to 1000 kPa, so the thickness of sensing diaphragm of $5.0\mu m$ is used, so as to observe sensor's contact mode. Thus the testing results can only used for concept proof. The test results show that sensors with $670\mu m$ diaphragm size have the largest sensitivity, which verifies the optimal design by genetic algorithm. A sensitivity improvement of 709% can be achieved in the sensor with $670\mu m$ side length. Besides, a MS3110 measurement board is utilized to provide a conversion from capacitance to voltage. The voltage output of the pressure sensor is between 0 to $4.0V$, which can be easily handled by the electronic circuits.

7.2 Suggestions for future work

Based on the simulation, design, fabrication and testing work that have been completed, and the performance requirements put by fast development of pressure sensor industry, suggestions for future work include:

- In the design of micro pressure sensors, the analytical model is proposed and plays important roles in the estimation of sensor performances. Currently, the model as well as the genetic algorithm can only address the sensitivity optimization and touch point design. Further research may be conducted on the model to analyze more performance indexes such as hysteresis, nonlinear effect and creeping etc. After successfully characterizing these non-linear phenomena, it is possible to find some solutions to compensate for them, either by adding compensation algorithms in signal processing circuits or by

modifying sensor mechanical structures and materials.

- In the fabrication and testing of the micro capacitive pressure sensors, it can be observed that 441% to 709% percentage improvement in sensitivity when the sensors work in the contact mode. Although concept proof has been achieved and there is still more space to improve the sensor performance. It should be very useful to test these sensors in a very high pressure system, or even in the hydrostatic tanks.

- In sensor industry, capacitance change in the pressure sensors are normally converted to voltage or current output, followed by signal processing and amplification. In the research, MS3110 board has been used to fulfill this requirement. However, the connections between the sensor chips and the MS3110 board need to go through probes and wires, which may bring large stray capacitances to the measurement. To reduce the effect of stray capacitances, processing circuit should be put much closer to the sensor chips and connect them with wire bonding. It is better to put sensor mechanical parts and signal processing units in a single chip, but this requires that the sensor fabrication is compatible to electronic circuit process.

Bibliography

[1] J. Bryzek. Impact of mems technology on society. *Sensors and Actuators*, A56(1-2):179–192, 1996.

[2] J. Bryzek. Mems: A closer look, part 2: the mems industry in silicon valley and its impact on sensor technology. *Sensors*, page 4, 1996.

[3] Andrew D Ketsdever, Riki H Lee, and Taylor C Lilly. Performance testing of a microfabricated propulsion system for nanosatellite applications. *Journal of Micromechanics and Microengineering*, 15(12):2254–2263, 2005.

[4] C. Pramanik, H. Saha, and U. Gangopadhyay. Design optimization of a high performance silicon mems piezoresistive pressure sensor for biomedical applications. *Journal of Micromechanics and Microengineering*, 16(10):2060–2066, 2006.

[5] Subrahmanyam Gorthi, Atanu Mohanty, and Anindya Chatterjee. Cantilever beam electrostatic mems actuators beyond pull-in. *Journal of Micromechanics and Microengineering*, 16(9):1800–1810, 2006.

[6] Hyukjae Lee, Ronald A Coutu, Shankar Mall, and Kevin D Leedy. Characterization of metal and metal alloy films as contact materials in mems switches. *Journal of Micromechanics and Microengineering*, 16(3):557–563, 2006.

[7] Gregory T.A. Kovacs. *Micromachinsed Transducers Sourcebook*. McGraw-Hill, New York, 2000.

[8] M Pedersen, M G H Meijerink, W Olthuis, and P Bergveld. A capacitive differential pressure sensor with polyimide diaphragm. *Journal of Micromechanics and Microengineering*, 7:250–252, 1997.

[9] K. Woonbae, W. Qian, et al. Application of au-sn eutectic bonding in hermetic rf mems wafer level packaging. In *Advanced Packaging Materials: Processes, Properties and Interfaces, 2004. Proceedings. 9th International Symposium on*, pages 215–219, 2004.

[10] Y.T. Cheng, L. Lin, and K. Najafi. Localized silicon fusion and eutectic bonding for mems fabrication and packaging. *Microelectromechanical Systems, Journal of*, 9(1):3–8, 2000.

[11] L. Ristic. *Sensor Technology and Devices.* Boston, 1994.

[12] C.S. Smith. Piezoresistance effect in germanium and silicon. *Physical Review*, 94(1):42–49, 1954.

[13] H.C. Nathanson and R.A. Wickstrom. A resonant-gate silicon surface transistor with high-q bandpass properties. *Applied Physics Letters*, 7:84, 1965.

[14] E.M. Blaser, W.H. Ko, and E.T. Yon. A miniature digital pressure transducer. In *24th Annual Conf. on Eng. in Med. and Biol.*, page 211, 1971.

[15] W. H. Ko, M. H. Bao, and Y. D. Hong. A high sensitivity integrated circuit capacitive pressure transducer. In *IEEE Trans. Elect. Dev.*, pages 48–56, 1982.

[16] C.S. Sander and J.W. Knutt. A monolithic capacitive pressure sensor with pulse-period output. In *IEEE Transactions on Electron Devices*, pages 927–930, 1980.

[17] K.E. Petersen. Silicon as a mechanical material. In *Proceedings of the IEEE*, pages 420–457, 1982.

[18] B.Kloeck and N.F. de Rooij. *Mechanical Sensors.* John Wiley & Sons, 1994.

[19] V. Mosser, J. Suski, J. Goss, and E. Obermeier. Piezo-resistive pressure sensors based on poly-crystalline silicon. *Sensors and Actuators, A*, 28:113–132, 1991.

[20] P.D. Dimitropoulos, C. Kachris, D.P. Karampatzakis, and G.I. Stamoulis. A new soi monolithic capacitive sensor for absolute and differential pressure measurements. *Sensors and Actuators A: Physical*, 123-124:36–43, 2005.

[21] Min-Xin Zhou, Qing-An Huang, and Ming Qin. Modeling, design and fabrication of a triple-layered capacitive pressure sensor. *Sensors and Actuators A: Physical*, 117(1):71–81, 2005.

[22] Klaus Kasten, Norbert Kordas, Holger Kappert, and Wilfried Mokwa. Capacitive pressure sensor with monolithically integrated cmos readout circuit for high temperature applications. *Sensors and Actuators A: Physical*, 97-98(1):83–87, 2002.

[23] K.D. Wise. Integrated sensors: key to future vlsi systems. In *Proceedings of the 6th Sensor Symposium*, pages 24–32, 1986.

[24] Y.S. Lee and K.D. Wise. A batched-fabricated capacitive pressure transducer with low temperature sensitivity. In *IEEE Transactions on Electron Devices*, pages 42–48, 1982.

[25] Carlos H. Mastrangelo, Xia Zhang, and William C. Tang. Surface-micromachined dapacitive differential pressure sensor with lithographically defined silicon diaphragm. *Journal of Mircoelectromechanical systems*, 5(2):98–105, 1996.

[26] Y.E. Park and K.D. Wise. An mos switched-capacitor readout amplifier for capacitive pressure sensors. In *Proceedings of the IEEE Custom IC Conferenece*, pages 380–384, 1991.

[27] K.E. Petersen, F. Pourahmadi, J. Brown, et al. Resonant beam pressure sensor with silicon fusion bonding. In *Digest of Technical Papers, 1991 In-*

ternational Conference on Solid-State Sensors and Actuators, pages 664–667, 1991.

[28] D.W. Burns, J.D. Zook, et al. A digital pressure sensor based on resonant microbeams. In *Technical Digest: Solid State Sensor and Actuator Workshop, Hilton Head '94*, pages 221–224, 1994.

[29] D.W. Burns, J.D. Zook, et al. Sealed-cavity resonant microbeam pressure sensor. *Sensors and Actuators A*, 48:179–186, 1995.

[30] C.J. Welham, J.W. Gardner, et al. A laternally driven micromachined resonant pressure sensor. In *The 8th International Confernece on solid-State Sensors and Actuators, Transducer '95*, pages 586–589, 1995.

[31] T.Bourouina, C.Vauge, and H.Mekki. Variational method for tensile stress evaluation and application to heavily boron-doped square-shaped silicon diaphragms. *Sensors and Actuators A*, 49:21–27, 1995.

[32] G. Vass. The principles of level measurement. *Sensors*, 17:55–64, 2000.

[33] P. Del Vecchio and J. Rowe. Htg detects storage tank leaks. *InTech*, 38:24–27, 1991.

[34] K. van Schuylenbergh and R. Puers. Self tuning inductive powering for implantable telemetric monitoring systems. *Sensors and Actuators*, 52(1-3):1–7, 1996.

[35] K. Shah, H. Thumu, et al. A mems vertical fringe comb capacitive pressure sensor for biomedical application. In *Technical Proceedings of the 2005 NSTI Nanotechnology Conference and Trade Show*, pages 379–382, 2005.

[36] J. Champier Z. Hamici, R. Itti. A high efficiency power and data transmission system for biomedical implanted electronic devices. *Measurement Science & Technology*, 7(2):192–201, 1996.

[37] U.Paschen, M.Leineweber, et al. A novel tactile sensor system for heavy-load applications based on an integrated capacitive pressure sensor. *Sensors and Actuators A*, 68:294–298, 1998.

[38] G.Bistue, J.G.Elizalde, et al. A design tool for pressure microsensors based on fem simulations. *Sensors and Actuators A*, 62:591–594, 1997.

[39] Woei Wan Tan, Pei Ge, et al. Developement of a 3-plates capacitive pressure sensor. *International Journal of Computational Engineering Science*, 4(3):613–616, 2003.

[40] R.Schellin, G.Hess, C.Thielemann, et al. Measurements of the mechanical behavior of micromachined silicon and the silicon-nitride membranes for microphones, pressure sensors, and gas flow meters. *Sensors and Actuators A*, 41-42:287–292, 1994.

[41] R.Steinmann, H.Friemann, C.Prescher, and R.Schellin. Mechanical behavior of micromachined sensor membranes under uniform external pressure affected by in-plane stresses using a ritz method and hermite polynomials. *Sensors and Actuators A*, 48:37–46, 1995.

[42] B.Folkmer, H.L.Offereins, H.Sandmaier, W.Lang, et al. A simulation tool for mechanical sensor design. *Sensors and Actuators A*, 32:521–524, 1992.

[43] R.W.G Wyckoff. *Crystal Structures*. Interscience, 2nd edition, 1963.

[44] H.J.McSkimin, W.L.Bond, E.Buehler, and G.K.Teal. Measurement of the elastic constants of silicon single crystals and their thermal coefficients. *Physicis Review*, 83:1080, Sept. 1951.

[45] D.Meakin, J.Stonemenos, et al. Structural studies of low-temperature low-pressure chemical deposited polycrystalline silicon. *Journal of Applied Physics*, 61(11):5031–5037, June 1987.

[46] X.Ding, W.H.Ko, and J.M.Mansour. Residual stress and mechanical properties of boron-doped p-silicon films. *Sensors and Actuators A*, 21-23:866–871, 1990.

[47] Alberto Carpinteri. *Structural Mechanics - A unified approach.* E & FN Spon, 1997.

[48] Staffan Greek, Fredric Ericson, et al. Mechanical characterization of thick polysilicon films: Young's modulus and fracture strength evaluated with microstructures. *Journal of Micromechanics and Microengineering*, 9:245–251, 1999.

[49] J. Bagdahn, W.N. Jr. Sharpe, and O Jadaan. Fracture strength of polysilicon at stress concentrations. *Microelectromechanical Systems, Journal of*, 12(3):302–312, 2003.

[50] Q. Wang and Wen H. Ko. Modeling of touch mode capacitive sensors and diaphragms. *Sensors and Actuators A*, 75:230–241, 1999.

[51] C.Wilson and P.Beck. Fracture testing of bulk silicon microcantilever beams subjected to a side load. *Journal of Microelectromechical System*, 5:142–150, 1996.

[52] Ville Kaajakari and Tomi Mattila. Nonlinear limits for single-crystal silicon microresonators. *Journal of Microelectromechical System*, 13(5):715–723, 2004.

[53] R. Plonsey and R. E. Collin. *Principles and Applications of Electromagnetic Fields.* McGraw-Hill, New York, 1961.

[54] M.J. Kumar, S.K. Gupta, and V. Venkataraman. Compact modeling of the effects of parasitic internal fringe capacitance on the threshold voltage of high-k gate-dielectric nanoscale soi mosfets. In *Electron Devices, IEEE Transactions on*, pages 706–711, 2006.

[55] A. Bansal, B.C. Paul, and K.; Roy. Modeling and optimization of fringe capacitance of nanoscale dgmos devices. In *Electron Devices, IEEE Transactions on*, pages 256–262, 2005.

[56] *MEDICI 4.0.* Technology Modeling Associates, Inc.,, Palo Alto, CA, 1997.

[57] H.J.; Hovel. Silicon-on-insulator substrates: status and prognosis. In *SOI Conference, Proceedings., 1996 IEEE International*, pages 1–3, October 1996.

[58] Huai-Yuan Chu, Shih-Wei Lee, and Weileun Fang. Design and fabrication of multi-degrees-of-freedom single crystal silicon moveable platforms on soi wafer. In *Solid-State Sensors, Actuators and Microsystems, 2005. The 13th International Conference on*, pages 737–740, 2005.

[59] Y.; Kanda. What kinds of soi wafers are suitable for what micromachining purposes. In *Solid-State Sensors and Actuators, 1991. Digest of Technical Papers, TRANSDUCERS '91., 1991 International Conference on*, pages 452–455, 1991.

[60] Silicon Quest International. [Online]. *Available: http://www.siliconquest.com/eng/products/soi.htm*.

[61] David Koester, Allen Cowen, Amaswamy Mahadevan, et al. *PolyMUMPs design handbooks, Revision 9.0.* MEMSCAP, 2003.

[62] K. Schjlberg-Henriksen, G.U. Jensen, A. Hanneborg, and H.; Jakobsen. Anodic bonding for monolithically integrated mems. In *TRANSDUCERS, Solid-State Sensors, Actuators and Microsystems, 12th International Conference on, 2003*, pages 1323–1326, 2003.

[63] Ciprian Iliescu, Jianmin Miao, and Francis E.H. Tay. Stress control in masking layers for deep wet micromachining of pyrex glass. *Sensors and Actuators A*, 117(5):286–292, 2005.

[64] O. Castillo and L. Trujillo. Multiple objective optimization genetic algorithms for path planning in autonomous mobile robots. *International Journal of Computers, Systems and Signals*, 6(1):48–63, 2005.

[65] C. M. Fonseca and C. J. Fleming. Genetic algorithms for multiobjective optimization: formulation, discussion and generalization. In *5th Int. Conf. Genetic Algorithms*, pages 416–423, 1993.

[66] I.G.Boobnov. *Theory of structures of ships.* vol 2, St. Petersburg, 1914.

[67] S.Timoschenko and S.Woinowsky-Krieger. *Theory of plates and shells.* McGraw-Hill, NewYork, 1959.

[68] E.Suhir. *Structural Analysis in Microelectronic and Fiber-Optic Systems.* Van Nostrand Reinhold, Volume I, 1991.

[69] Wen H. Ko, Q. Wang, and Y. Wang. Touch mode capactivie pressure sensors for industrial applications. In *Technical Digest: 1996 Solid-State Sensor and Actuator Workshop*, pages 244–248, Hilton Head, 1996.

[70] D.Peters, H.Bolte, et al. Modeling and designing quadratic membrane structures. *Microelectronics Journal*, 33:11–19, 2002.

[71] I.D. Vrinceanu and S Danyluk. Measurement of residual stress in single crystal silicon wafers. In *Advanced Packaging Materials, 2002. Proceedings. 2002 8th International Symposium on*, pages 297–301, 2002.

[72] Kuo-Shen Chen, Terry Yuan-Fang Chen, Chia-Cheng Chuang, and I.-Kuan Lin. Full-field wafer level thin film stress measurement by phase-stepping shadow moir. In *IEEE TRANSACTIONS ON COMPONENTS AND PACKAGING TECHNOLOGIES*, pages 594–601, 2004.

[73] Lloyd Hamilton Donnell. *Beams, Plates, and Shells.* McGraw-Hill, NewYork, 1976.

[74] Guangqing Meng and Wen H.Ko. Modeling of circular diaphragm and spreadsheet solution programming for touch mode capacitive sensors. *Sensors and Actuators*, 75:45–52, 1999.

[75] K. F. Man, K. S. Tang, and S. Kwong. *Genetic Algorithms*. Springer, London, 1999.

[76] A. Chen, K. Subprasom, and E.Z Ji. A simulation-based mult-objective genetic algorithm (smoga) for transportation network design problem. In *Uncertainty Modeling and Analysis, 2003. ISUMA 2003. Fourth International Symposium on*, pages 373–378, 2003.

[77] K. Sugihara. Genetic algorithms for adaptive planning of path and trajectory of a mobile robot in 2d terrains. In *IEICE Trans. Inf. & Syst.,*, pages 309–313, 1997.

[78] J. D. Schaffer. Multiple objective optimization with vector evaluated genetic algorithms. In *Genetic Algorithms and their Applications: Proceedings of the First International Conference on Genetic Algorithms*, pages 93–100, 1985.

[79] D. E. Goldberg. *Genetic Algorithms in Search, Optimization and Machine Learning*. Addison-Wesley, MA, 1989.

[80] M. Srinivas and K. Deb. Multiobjective optimization using nondominated sorting in genetic algorithms. *Evolutionary Computation*, 2(3):221–248, 1994.

[81] S. L. Ho, Shiyou Yang, Guangzheng Ni, and H. C. Wong. A tabu method to find the pareto solutions of multiobjective optimal design problems in electromagnetics. In *IEEE TRANSACTIONS ON MAGNETICS*, pages 1013 – 1016, 2002.

[82] K.C. Tan, T.H. Lee, D. Khor, et al. A multi-objective evolutionary algorithm toolbox for computeraided multi-objective optimization. *IEEE Transactions on Systems, Man and Cybernetics: Part B (Cybernetics)*, 31(4):537–556, 2001.

[83] K. C. Tan, Y. H. Chew, and L. H. Lee. A hybrid multiobjective evolutionary algorithm for solving truck and trailer vehicle routing problems. *European Journal of Operational Research*, 172:855–885, 2006.

[84] K. C. Tan, C. K. Goh, Y. J. Yang, and T. H. Lee. Evolving better population distribution and exploration in evolutionary multi-objective optimization. *European Journal of Operational Research*, 171:463–495, 2006.

[85] J. Melngailis, H.I. Smith, and N. Efremow. Instrumentation for conformable photomask lithography. In *Electron Devices, IEEE Transactions on*, pages 496 – 498, 1975.

[86] Mattias Vangboy and Ylva Backlund. Precise mask alignment to the crystallographic orientation of silicon wafers using wet anisotropic etching. *Microelectromechanical Systems, Journal of*, 6:279–284, 1996.

[87] Hulsenberg D et al. New glasses for microsystem technologies. *Proc. Micro System Technol.*, pages 259–268, 1994.

[88] Shoji S, Kikuchi H, and Torigoe H. Anodic bonding below 180 degrees for packaging and assembling of mems using lithium alminosilicate-
-quartz glass-ceramic. In *Proc.MEMS'97*, pages 482–487, 1997.

[89] Peter Enoksson Thierry Corman and Goran Stemme. Deep wet etching of borosilicate glass using an anodically bonded silicon substrate as mask. *Journal of Micromechanics and Microengineering*, 8:84–87, 1998.

[90] O.N. Hartley, R. Russell, et al. Investigation of thin aluminium films on the rear of monocrystalline silicon solar cells for back surface field formation. In *Photovoltaic Specialists Conference, 2002. Conference Record of the Twenty-Ninth IEEE*, pages 118–121, 2002.

[91] Lin Yinyin, Tang Ting-ao, et al. Fabrication and characteristics of au/cr/pzt/pt/ti/zro2/si structure for mfmis fet application. In *Solid-State*

and Integrated-Circuit Technology, 2001. Proceedings. 6th International Conference on, pages 702–705, 2001.

[92] D. Pantelica, G. Drafta, et al. Rbs analysis of au/cr contact on gaas. In *Semiconductor Conference, 1996., International*, pages 405–408, 1996.

[93] K. Kim, Y. Song, G.S. Lee, and J. Song. Electrical properties of pecvd oxide films deposited at room temperature. *Electronics Letters*, 32(21):2015–2016, 1996.

[94] Chang Liu and Yu-Chong Tai. Sealing of micromachined cavities using chemical vapor deposition methods: characterization and optimization. *Microelectromechanical Systems, Journal of*, 8(2):135–145, 1999.

[95] M. Yoshimaru, N. Inoue, et al. Effects of deposition temperature on the oxidation resistance and electrical characteristics of silicon nitride. In *Electron Devices, IEEE Transactions on*, pages 1747–1752, 1994.

[96] Wen-Hsien Chuang, T. Luger, et al. Mechanical property characterization of lpcvd silicon nitride thin films at cryogenic temperatures. *Microelectromechanical Systems, Journal of*, 13(5):870–879, 2004.

[97] D. Hojo, N. Tokuda, and K. Yamabe. Increasing roughness at sio_2si interface during thermal oxidation. In *Gate Insulator, Extended Abstracts of International Workshop on*, pages 128–129, 2001.

[98] W. Chu, M. Mehregany, D. Hansford, and P. Pirouz. Effect of thermal oxidation on residual stress distribution through the thickness of p+ silicon films. In *Solid-State Sensor and Actuator Workshop, 5th Technical Digest., IEEE*, pages 90–93, 1992.

[99] R. Moazzami and C. Hu. A high-quality stacked thermal lpcvd gate oxide technology for ulsi. *Electron Device Letters*, 14(2):72–73, 1993.

[100] P.G. Carey, P.M. Smith, and M.O. Thompson. Polysilicon thin film transistors fabricated at 100c on a flexible plastic substrate. In *Device Research Conference Digest, 55th*, pages 58–59, 1997.

[101] D.J. Monk, D.S. Soane, et al. Hydrofluoric acid etching of silicon dioxide sacrificial layers. *Journal of the electrochemical society*, 141(1):264–269, 1994.

[102] Chang L.H. A study of psg sacrificial etch solutions used in surface micromachining processing. In *Proceedings of the symposium on microstructures and microfabricated systems*, pages 79–85, 1994.

[103] K. Schjlberg-Henriksen, G.U. Jensen, et al. Anodic bonding for monolithically integrated mems. In *TRANSDUCERS, Solid-State Sensors, Actuators and Microsystems, 12th International Conference on*, pages 1323–1326, 2003.

Appendix A

GUI Method for Capacitance Calculation

The GUI method explores the intrinsic electrostatics of capacitors from the deformed geometry. It includes following steps:

1. Use FEM software to find the electric displacement $\vec{E}$ between the two plates.

2. Then compute charges on top and bottom plates according to Maxwell's equations (Gauss's law): the electric displacement flux $\vec{E}$ emanating from a closed surface S is equal to the charge contained with the volume V bounded surface S.:

$$\oint_S \vec{E} \cdot dS = \oint_V \rho \cdot dV = Q$$

   where ρ– volume charge density, Q - charge

3. Capacitance of the structure may then be computed

$$C = (Q_{top} + Q_{bottom})/2U$$

To simplify the calculation, first a square plate capacitor with 1.4 side length and 0.4 electrode gap is simulated, and the dielectrics between two plates is air (dielectric constant = 1.0). By using the PDE toolbox's GUI in Matlab, the capacitor's geometry is created and meshed by triangles. The electrostatics of capacitor can be simulated by solving basic elliptic equation:

$$-\nabla(c\nabla u) + au = f \qquad in\Omega$$

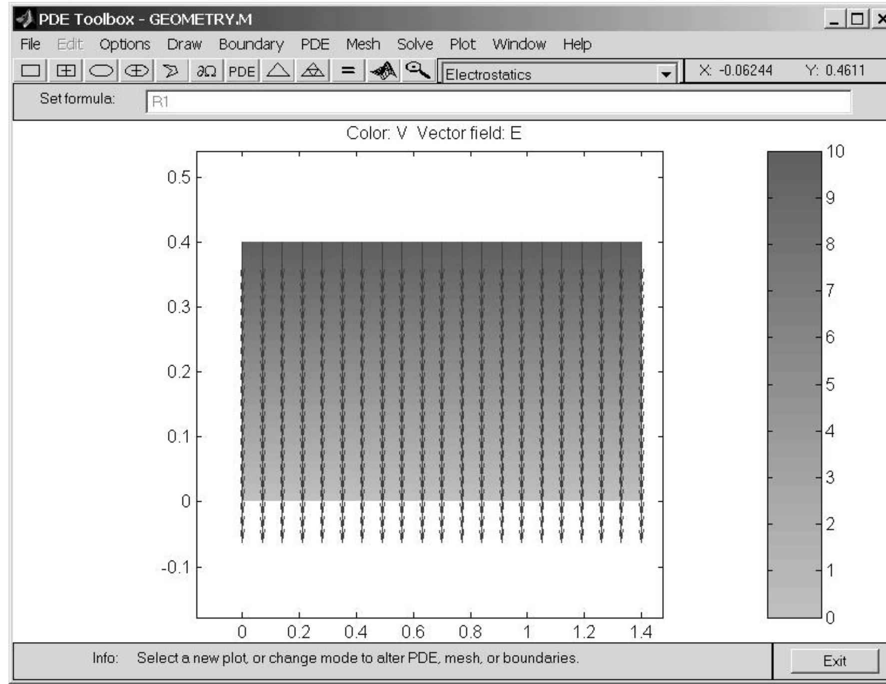

The solution of PDE equation u can be expressed in terms of elementary functions. To yield meaningful results, Dirichlet conditions are defined at top and bottom lines, by restricting test function $v = 0$ at boundary points, and setting $u = 10$ at top line, $u = 0$ at bottom line. For side boundaries, since the exact voltage is unknown, Neumann conditions are defined. The results obtained by solving the PDE equation are shown in Figure. .

The cross section view of deformed model is shown in Figure. . By integrating the electric displacement flux $\vec{e}$ along the electrode length, the electrode charge can be obtained, which is used in calculating the capacitance.

The PDE solutions and triangular mesh data in GUI simulation are exported to Matlab workspace. A m-file is written to compute the capacitance, and it has following steps:

1. Calculating the $\vec{E}$-field. Since the PDE solutions are just a matrix of voltages at each node, so function pdegrad is used to calculate electric displacement vectors ($\vec{E} = \nabla u$) at center of each triangle. Then the $\vec{E}$-field is interpolated to triangle nodes.

   $[Dxc, Dyc] = pdegrad(p, t, u);$ %p, t represents triangles data

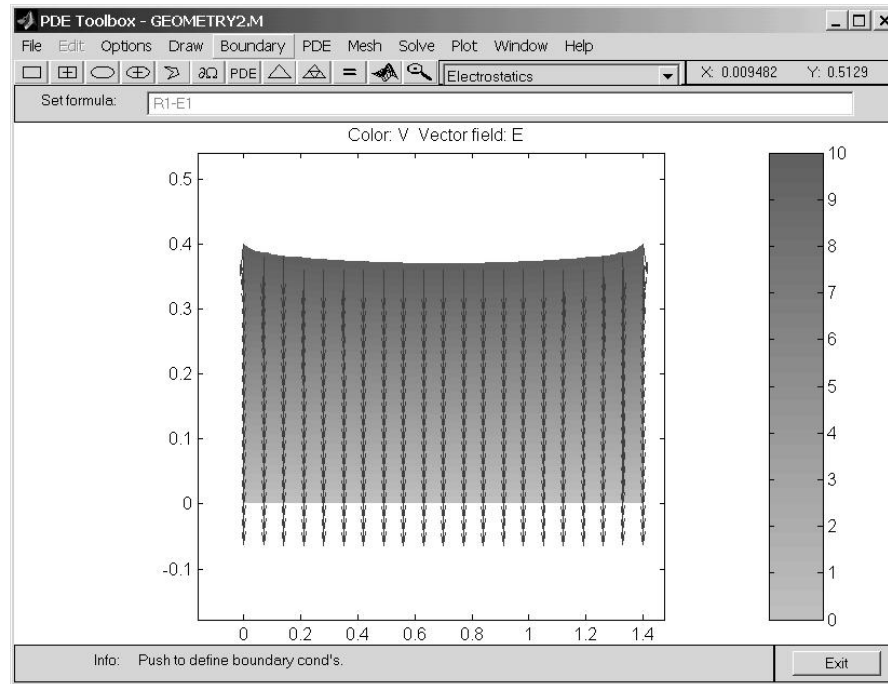

$Dx = pdeprtni(p, t, Dxc);$ %interpolate electric displacement D from

$Dy = pdeprtni(p, t, Dyc);$ %triangle centers to nodes

2. Pick out boundary points. There are two boundary sets: top boundary and bottom boundary. In this case, the bottom is always flat, so the condition $y < 0.001$ can be defined to get those points. However, the top boundary is not a straight line and may be difficult to define when the triangle mashes are very small. By choosing suitable mesh size, condition $y > 0.4 - deflection + 0.001$ is used to get top boundary points.

3. Sort the points and Line integrate to get the surface charge. The points in boundary sets are rearranged to have a sequence from left ($x = 0$) to right ($x = 0.4$). Recognizing the surface as a non-uniform length with constant width, the following equation can be obtained:

$$\Sigma \vec{E} \cdot dl = Q/w$$

4. Calculate total capacitance. After summarize the charges, the results should be checked so that top and bottom boundaries have the same value. If the

boundary sets are not selected properly, the top charge may not equal to bottom charge.

GUI Method	Step	Mesh size	Top charge	Bottom charge	Capacitance
	1	89	35.0000	35.0000	$4.9000\varepsilon_0$
	2	356	35.0000	35.0000	$4.9000\varepsilon_0$
	3	1424	35.0000	35.0000	$4.9000\varepsilon_0$
Integration Method					$4.9\varepsilon_0$

GUI Method	Step	Mesh size	Top charge	Bottom charge	Capacitance
	1	97	36.9515	37.3662	$5.2022\varepsilon_0$
	2	388	36.9416	37.4337	$5.2063\varepsilon_0$
	3	1552	37.8443	37.4606	$5.2713\varepsilon_0$
Integration Method					$5.18\varepsilon_0$

Appendix B

Basic Photo Lithography Process

1. HMDS (Hexamethyldisilazane) Printing under Vacuum. a. Baking the substrate at 110^oC for $3 \sim 5$ minutes; b. Baking and purging to remove surface moisture ($100^oC, 60sec.$); c. HMDS Printing (room temperature, $20sec.$); d. Baking and purging (60 sec.);

2. Wafer cooling Cool down the wafer in room temperature for 60 sec.

3. Spin coating. Thick PR (AZ-9260) is for large pattern lithography. Thin PR (AZ-7220) is for small pattern lithography where critical dimension is below 2-3 microns. a. Clean aligner using Acetone; b. Clean PR tube using Acetone; c. Place glass wafer on the tabletop and adjust its position using aligner; d. Press "Vacuum", fix wafer position using pressure difference on both sides; e. Choose Automatic mode, and spin Photo resist on the wafer surface.

4. Resist Pre-Baking.

	Temp	Time
AZ-9260	110 ^oC	4 min.
AZ-7220	100 ^oC	1.5 min.

5. Resist Cooling.

	Temp	Time
AZ-9260	24 ^oC	1.0 min.
AZ-7220	24 ^oC	1.0 min.

6. Photo Resist Exposure. 365 nm wave-length UV Intensity $9.3mv/cm^3$. For $10\mu m$ thick AZ-9260 PR, the exposure time is 300 seconds and the exposure time reduced to 180 seconds for $4\mu m$ thick AZ-7220 PR.

7. Resist Post-Baking.

	Temp	Time
AZ-9260		no post baking
AZ-7220	100 ^oC	1.0 min.

8. Developing. Dip the wafer into a developer of potassium hydroxide (KOH) at room temperature for 60 $\sim$ 70 seconds.

9. DI Water Rinsing. Rinse both surfaces of the glass wafer. Be careful not to damage the PR patterns on the wafer.

10. Spin Drying. Dry the glass wafer in the spun-dry machine for 120 seconds at $700rpm$ spin speed.

11. Microscope Inspection. Check the PR pattern in the Microscope.

Appendix C

MS3110 Measurement Board Calibration

MS3110 Universal Capacitive Readout Board is a general purpose, ultra-low noise CMOS IC intended to support a variety of MEMS sensors (such as accelerometers, rate sensors and capacitive pressure sensors) that require a high resolution capacitive readout interface. Typically, the MS3110 measurement board is capable of sensing capacitance changes as small as $4.0aF/rtHz$. In order to test the features of MS3110 Evaluation Board, some equipments are needed:

- a +5 VDC Power Supply and a +16 VDC supply;
- an Oscilloscope;
- two multi-meters;
- a Parallel port cable, a IBM PC;
- a MS3110 evaluation board, 16 pin SOIC.

The Evaluation Board needs a +5V DC supply for operation. The DC supply is connected to the banana jacks located on the upper edge of the board. Connect a parallel port cable from PC to J2 on the Evaluation Board. There are a software in PC which will send programming signals to MS3110.

MS3110 board measures the capacitance change between capacitors (CS1 and CS2) and provides a voltage output proportional to that change. The transfer

function from capacitance to voltage output is as:

$$V_{out} = GAINSEL * V_{ref} * 1.14 * (CS_1 - CS_2)/C_{ref} + V_{ref} \quad (.1)$$

Where V_{out} is output voltage; $GAINSEL = 2V/V$ nominal; C_{ref} is selected to optimize input sense capacitance range.

The reference voltage V_{ref} should be adjusted to $2.25V \pm 0.01V$. First, select "nominal" for the **Voltage reference trim T[3:0]** and use a multimeter in DC Volts Mode to detect the reference voltage. V_{ref} can be adjusted within requirement by change settings in trim T[3:0].

Then remove the jumper on J9, and place the second multimeter across the pins. Set the multimeter to DC current mode. This multimeter must be quite sensitive in detecting small current in μA. Adjust **Current reference trim R[2:0]** and make the current as close to $10\mu A$ as possible. After the requirement is satisfied, place the jumper back and remove the multimeter.

The last bias setting is the frequency of carrier wave. Put the probe on pin 1 of J3, and the ground. Adjust the oscilloscope to display a square wave. **Oscillator Trim D[2:0]** can be used to tune the square wave to have a $100kHz \pm 5kHz$ frequency, and a 2.25V magnitude. Remove the oscilloscope after the setting is finished.

B1. Nominal capacitance $C_{ref} = 5.130pF$

- Reference Voltage = $2.258V$; (nominal)
- Reference Current = $0.010mA$; (nominal)
- Frequency of Square Wave = $100.5kHz$; (+24%)
- $C_{ref}[9:0] = 5.130pF$;

$CS_2 - CS_1 (pF)$					
	-1.501	-1.026	-0.589	-0.228	-0.019
	0	0.019	0.228	0.589	1.026
$V_{out}(V)$	0.724	1.202	1.638	2.003	2.213
	2.233	2.252	2.461	2.822	3.250

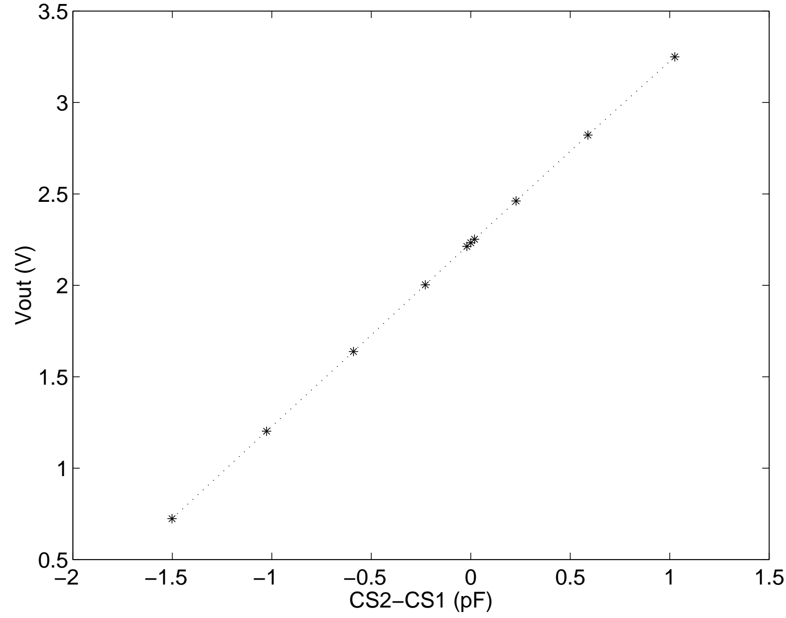

The relationship between V_{out} and $CS_2 - CS_1$ is represented by the first order polynomial:

$$V_{out} = 1.0015 * (CS_2 - CS_1) + 2.2301$$

The following function is obtained from MS3110 data sheet:

$$\begin{aligned} V_{out} &= (V_{ref})(1.14)(GAINSEL)\frac{CS_2 - CS_1}{C_{ref}} + V_{ref} \\ &= 2.258 * 1.14 * 2 * \frac{CS_2 - CS_1}{5.130} + 2.258 \\ &= 1.0036 * (CS_2 - CS_1) + 2.258 \end{aligned}$$

B2. Nominal capacitance $C_{ref} = 0.057pF$

- Reference Voltage = $2.259V$; (nominal)
- Reference Current = $0.010mA$; (-13.7%)
- Frequency of Square Wave = $99.05kHz$; $(+13\%)$
- $C_{ref}[9:0] = 0.057pF$;

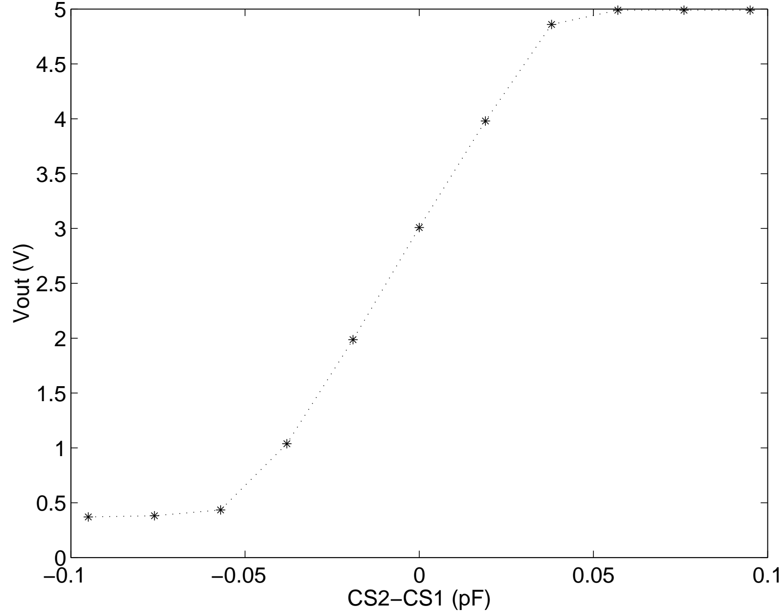

$CS_2 - CS_1(pF)$	-0.095	-0.076	-0.057	-0.038	-0.019	0
V_{out} (V)	0.371	0.381	0.435	1.038	1.987	3.009
	0.019	0.038	0.057	0.076	0.095	
	3.980	4.860	4.990	4.990	4.990	

Consider the linear range from $-0.019pF$ to $0.019pF$, the function is:

$$V_{out} = 52.4474 * (CS_2 - CS_1) + 2.9920$$

Theoretically, the function from MS3110 data sheet is shown as:

$$\begin{aligned} V_{out} &= (V_{ref})(1.14)(GAINSEL)\frac{CS_2 - CS_1}{C_{ref}} + V_{ref} \\ &= 2.259 * 1.14 * 2 * \frac{CS_2 - CS_1}{0.057} + 2.259 \\ &= 90.360 * (CS_2 - CS_1) + 2.259 \end{aligned}$$

Apart from the experiment data shown in Section 6.4.3, the result of additional experiments as listed above help to optimize the settings to measure the proposed sensor. Generally large C_{ref} value would result in a less amplification effect, while small C_{ref}, such as $0.057pF$, would constrain the measurement into a very narrow working range.

In those experiments, output voltage V_{out} has been monitored by an oscilloscope. It has been found that V_{out} is a straight line with $0.1V$ width on the oscil-

loscope, while the corresponding readout in multimeter has a better accuracy of 0.001V. Noise signals observed on the oscilloscope may come from the power supply. Therefore a high precision voltage supply would be helpful to decrease noise level, alternatively a filter is needed between voltage supply and the measurement board.

When the measurement operates in the differential mode, the external sensing capacitors that are connected to the CS_1 and CS_2 are usually mismatched, and this leads to a DC offset in the output signal path. As the capacitive sensor under detection is within the range of CS_1 array value, this gives the option to operate the chip single-ended. In other words, suitable CS_1 and C_{ref} would be able to minimize the offset balance with external sensing capacitance CS_2.